



저작자표시-비영리-변경금지 2.0 대한민국

이용자는 아래의 조건을 따르는 경우에 한하여 자유롭게

- 이 저작물을 복제, 배포, 전송, 전시, 공연 및 방송할 수 있습니다.

다음과 같은 조건을 따라야 합니다:



저작자표시. 귀하는 원저작자를 표시하여야 합니다.



비영리. 귀하는 이 저작물을 영리 목적으로 이용할 수 없습니다.



변경금지. 귀하는 이 저작물을 개작, 변형 또는 가공할 수 없습니다.

- 귀하는, 이 저작물의 재이용이나 배포의 경우, 이 저작물에 적용된 이용허락조건을 명확하게 나타내어야 합니다.
- 저작권자로부터 별도의 허가를 받으면 이러한 조건들은 적용되지 않습니다.

저작권법에 따른 이용자의 권리는 위의 내용에 의하여 영향을 받지 않습니다.

이것은 [이용허락규약\(Legal Code\)](#)을 이해하기 쉽게 요약한 것입니다.

[Disclaimer](#)

공학박사 학위논문

**Fabrications of Polymeric
Nano-structured Materials using
Ion-beam Irradiation**

이온빔 조사를 활용한
고분자 표면 나노구조체의 형성 연구

2022년 8월

서울대학교 대학원

재료공학부

정성훈

Fabrications of Polymeric Nano-structured Materials using Ion-beam Irradiation

지도 교수 장호원

이 논문을 공학박사 학위논문으로 제출함
2022년 8월

서울대학교 대학원
재료공학부
정성훈

정성훈의 공학박사 학위논문을 인준함
2022년 8월

위원장 김진영 (인)

부위원장 장호원 (인)

위원 선정윤 (인)

위원 김도근 (인)

위원 Mohammadreza Shokouhimehr (인)

Abstract

Rapid nanotechnology development has recently enabled numerous nanomaterials to be used in daily life. It is being used in a wide range of materials, machinery, electronics, and life sciences, from semiconductors that utilize nanometer-scale patterning, nanocoating films used in displays or vehicles, filters to filter harmful substances such as fine dust, and proteins/genetic materials for treatment. Among the numerous nanomaterials, the surface with nanostructure has different physical properties from the flat surface, which can give the surface new functionality. The surface on which the nanostructure is formed can maximize surface energy to make hydrophilic to superhydrophilic and hydrophobic to superhydrophobic, and use a large specific surface area for adhesion and bonding, or increase the chemical reaction speed. In addition, new optical properties such as low reflection and coloring may be provided by generating light scattering, diffraction, and plasmon resonance.

Fabrication methods of nanostructure can be divided into top-down methods such as lithography, imprinting, and self-nanostructure, and bottom-up methods for growing nanomaterials. Among the top-down methods, lithography and imprinting are methods that can form very sophisticated patterns, but masks for patterning are required, and process prices are very high. Therefore, they are suitable for applications that require very sophisticated and regular patterns, such as semiconductors and plasmonic resonance, but in fields such as low reflection, superhydrophilic/super water repellent, and catalysts, different production methods, which are fast and cheap, are required.

A linear ion-beam is a device that modifies the surface by emitting several kV ions in a vacuum of about 10^{-3} Torr. As the kind of plasma generating source, ion energy control and incident angle control are more accessible than widely used RF-type plasma, and length is easily expanded, thereby being advantageous for mass production. Depending on the process conditions of the linear ion-beam, various physical and chemical characteristics on the surface, such as etching, generation of an oxide film/nitride film, surface energy change, and surface shape change, may occur. In this study, the surface shape of the polymer films used in everyday life, such as PEN, PDMS, and PET, were controlled using a linear ion beam, and the cause was investigated.

When an ion beam is irradiated to PEN, a nano-dimple having a diameter and a height of about 100 nm is formed. The formed nano-dimple changes the optical properties of the PEN. It was confirmed that the formation of the PEN surface nanostructure was well simulated using the DKS model. Conforming to the DKS model means that the difference in sputtering rates depending on the location of microscopic roughness less than several nm on the surface of the PEN is the cause of nanodimple formation.

When an ion beam is irradiated to the PDMS surface, a nano-wrinkle structure is created. Through XPS surface analysis, it was confirmed that the SiO bond of PDMS on the surface changed to the hardskin layer close to the SiO₂ bond. Displace per atom (DPA) values according to depth were calculated using dissociation energy (E_d) of carbon-based bond and nuclear stopping ($(dE/dx)_{\text{nuclear}}$) calculated by SRIM. To compare DPA and changes in carbon bonds measured by XPS depth profiling, H-CH₂ and C-Si bonds with a DPA value of 1.5 or more changed significantly. It was

concluded that the decomposition of the bonds could be predicted through the calculation of the DPA value.

The PET surface irradiated with the ion beam has a nano-hairy structure. It was confirmed that the formed nano-hairy structure significantly increased the scattering of PET. The scattering degree increased as the size of the nanostructure increased. Scattering is greatly affected by the size and wavelength of nanostructures, and since the size of nanostructures formed is about 40 to 60 nm, light in the visible light region (about 400 to 800 nm) is greatly affected by Rayleigh scattering behavior. Since Rayleigh scattering is inversely proportional to the fourth power of wavelength, the wavelength corresponding to the blue light of the visible light shows a much larger scattering degree than the wavelength of the red light, which is well fitted with the measured haziness results. OLED was manufactured using the nano-hairy substrate. In OLED, extracting light trapped inside the device to the outside is essential in improving efficiency. OLED manufactured on nano-hairy PET substrate had increased efficiency by up to 30% compared to OLED manufactured on flat PET, which means that nano-hairy structure on PET surface is very efficient in extracting light trapped in the substrate to the outside.

The development of surface treatment technology for filters consisting of 1-dimensional fibers such as coronavirus prevention masks and HEPA filters for air purifiers is crucial. When an ion-beam with similar energy for fabrications of nano-hairy structure on PET film irradiates on PET fibers which have a thickness of several tens of micrometers, the fibers are agglomerated due to Rayleigh-Plateau instability. In order to prevent agglomeration, an increment of temperature during the treatment process should be suppressed. The amount of temperature change could have a similar correlation with the amount of phonon calculated through SRIM.

Therefore, a filter fabric irradiated by temperature-controlled conditions could obtain high adhesion while suppressing fiber agglomerations. As a result, the filter fiber and copper had high adhesion. Copper-coated filters were evaluated for antiviral and antibacterial properties for coronavirus (SARS-CoV-2) and four types of bacteria, and as a result, more than 99% of viruses and bacteria were killed when exposed for 1 hour.

Through this study, changes in surface shape were observed by performing surface treatment of the polymer, and it was found that the behavior and cause of the shape change can be predicted through SRIM calculation. SRIM calculations could not match the calculation results quantitatively because the variables for polymer bonds were not precisely reflected in the calculations, but they were confirmed to be qualitatively predictable. It will be possible to predict the surface change behavior during ion-beam irradiation by applying it to various polymers such as polyimide (PI), polytetrafluoroethylene (PTFE), polystyrene (PS), and the like, as well as PEN, PDMS, and PET which are polymer materials conducted in this study. Linear ion beams are advantageous for expansion for mass production such as roll-to-roll processes, and this study, which focuses on oxygen and argon, which are non-toxic gases, is essential for future industries where eco-friendliness is emphasized.

Keyword : ion-beam, plasma, polymer, nano-structure, nano-dimple, nano-wrinkle, surface treatment, continuum equation, SRIM calculation, light extraction, antibacterial, antiviral

Student Number : 2018-35976

Table of Contents

ABSTRACT	i
TABLE OF CONTENTS	v
LIST OF FIGURES.....	1
LIST OF TABLES	6
CHAPTER 1. INTRODUCTION.....	7
1.1. Nanostructures on Polymer Substrates	7
1.1.1. Polymer Nanostructures	7
1.2. Closed Drift-Type Anode Layer Linear Ion Beam Source	11
1.2.1. Introduction	11
1.2.2. Theoretical Background	11
1.3. Surface Nanostructures Produced by Ion beam	17
1.3.1. Nano-hairy Structures of Polymers	17
1.3.2. Nano-wrinkle PDMS Structure	18
1.3.3. Nano-dimple Structures of Semiconductor Materials	19
1.3.4. Interactions Between Ions and Matter	20
1.3.5. Computational Analysis	23
1.4. Purpose of This Research Study.....	26
1.5. Bibliography.....	27
CHAPTER 2. PRINCIPLES OF FORMATION OF NANO-DIMPLE STRUCTURES ON PEN SUBSTRATE.....	32
2.1. Introduction	33
2.2. Materials and Methods	35
2.2.1. Materials.....	35
2.2.2. Ion Beam Treatment.....	35
2.2.3. Field-Emission Scanning Electron Microscopy	35
2.2.4. Atomic Force Microscopy.....	37
2.2.5. Field-Emission Transmission Electron Microscopy and the Electron Energy Loss Spectrum.....	37

2.3. Results and Discussion	38
2.4. Conclusions	48
2.5. Bibliography.....	50
CHAPTER 3. FABRICATION OF A NANO-WRINKLED PDMS SUBSTRATE.....	53
3.1 Introduction	54
3.2 Methods	57
3.3. Results and Discussion	59
3.4 Conclusions	80
3.5 Bibliography.....	82
CHAPTER 4. NANO-HAIRY PET STRUCTURE FOR THE ENHANCEMENT OF EXTERNAL LIGHT EXTRACTION EFFICIENCY OF OLEDs	87
4.1 Introduction	88
4.2 Experimental.....	91
4.2.1. Materials.....	91
4.2.2. Ion Beam Treatment.....	91
4.2.3. ITO Sputtering	91
4.2.4. OLED Fabrication.....	92
4.2.5. FE–SEM.....	94
4.2.6. AFM.....	94
4.2.7. Optical Properties.....	94
4.3 Results and Discussion	95
4.4 Conclusions	104
4.5 Bibliography.....	106
CHAPTER 5. IMPROVEMENT OF SURFACE ADHESION OF PET FIBER AND COPPER FOR ANTIMICROBIAL PROPERTY WITHOUT NANO-STRUCTURING.....	108
5.1 Introduction	109
5.2. Materials and Methods	112

5.2.1. Materials.....	112
5.2.2. Ion Beam Treatment and Copper Sputtering Deposition	112
5.2.3. SRIM Calculations	114
5.2.4. Adhesion Test of Copper Deposited onto the Filter	114
5.2.5. Observing the Surfaces of the Filters and Tapes	115
5.2.6. Method for Evaluation of Antibacterial Performance	115
5.2.7. Method for Evaluation of SARS-CoV-2 Elimination Performance	116
5.3. Results and Discussion	118
5.3.1. Condition of the Filters After Ion Beam Treatment	118
5.3.2. Composition and Adhesion Properties of the Filters	121
5.3.3. Antibacterial Properties of the Copper-Coated Filter	130
5.3.4. Antiviral Properties of the Copper-Coated Filter	133
5.4. Conclusions	135
5.5. Bibliography.....	137
CHAPTER 6. CONCLUSIONS	142
ABSTRACT IN KOREAN	146

LIST of Figures

Figure 1.1. Various applications of nanostructures.	8
Figure 1.2. Classification of the existing nanostructure fabrication processes.	10
Figure 1.3. Structure and cross-section of the LIS.	12
Figure 1.4. Cycloid motion of a charge inside LIS.	14
Figure 1.5. Interface for entering calculation parameters into SRIM, including the ion type, ion energy, substrate density, and atomic species.	24
Figure 1.6. SRIM window showing the calculation results. Various physical parameters characterizing the ion collision with a medium, such as the longitudinal and lateral ion distributions, numbers of recoil ions and phonons, and sputtering yield, can be determined.	25
Figure 2.1. Linear ion-beam irradiation on a moving substrate (speed: 10 mm/s). Ion current density and ion energy distribution function were measured by Faraday cup and retarding potential ion energy analyzer, respectively.	36
Figure 2.2. AFM images (area: $2\ \mu\text{m} \times 2\ \mu\text{m}$) of dimple patterns on a PEN surface by 600 eV argon ion-beam bombardment with ion doses of (a) $2.4 \times 10^{15} / \text{cm}^2$ and (b) $4.8 \times 10^{15} / \text{cm}^2$. X-axis and Y-axis line profiles: (c) $2.4 \times 10^{15} / \text{cm}^2$, (d) $4.8 \times 10^{15} / \text{cm}^2$. (e) Distribution of dimple diameter in the $2\ \mu\text{m} \times 2\ \mu\text{m}$ area.	39
Figure 2.3. Diameter measurement of dimple structure using SPIP TM software, (a) ion dose: $2.4 \times 10^{15} / \text{cm}^2$, (b) ion dose: $4.8 \times 10^{15} / \text{cm}^2$	40
Figure 2.4. (a) Cross-sectional SEM image of dimple pattern, (b) the points of EELS measurement at a peak and trough. (c) EELS at the selected peak and trough.	42
Figure 2.5. Spectrum of wide angle X-ray scattering, (a) as-received PEN, (b) 600 eV argon ion-beam irradiated PEN.	43

Figure 2.6. Simulation results by iterating the DKS Equation: (a) ion flux = 4.83×10^{13} /cm²·s, time = 50 s for 20 scans (b) ion flux = 4.83×10^{13} /cm²·s, time = 100 s for 40 scans. Experimentally obtained dimple patterns on the PEN surface: (c) 20 scans, (d) 40 scans. 46

Figure 2.7. Graphical summarization of Chapter 2. The nano-dimple structure of the PEN surface was fabricated using an argon ion-beam, and the structure was similar to the result calculated through the DKS model. 49

Figure 3.1. Wrinkled PDMS surfaces obtained after Ar ion-beam irradiations at ion energies of (a) 360 eV, (b) 600 eV, and (c) 840 eV. 60

Figure 3.2. XPS depth profiling of the Si 2p signal. The etching process was conducted for 100 s at intervals of 10 s and Ar ion energies of (a) 360 eV, (b) 600 eV, and (c) 840 eV. 63

Figure 3.3. Deconvolution of the Si 2p XPS peaks obtained for the topmost surface layers of (a) pristine PDMS and the PDMS substrates irradiated at Ar ion energies of (b) 360 eV, (c) 600 eV, and (d) 840 eV. 64

Figure 3.4. XPS depth profiling of the C 1 s signal. The etching process was conducted for 100 s at intervals of 10 s and Ar ion energies of (a) 360 eV, (b) 600 eV, and (c) 840 eV. 66

Figure 3.5. Bond ratios determined by conducting XPS C 1s depth profiling at Ar ion energies of (a) 360 eV, (b) 600 eV, and (c) 840 eV. DPA values obtained at Ar ion energies of (d) 360 eV, (e) 600 eV, and (f) 840 eV. The Ed magnitudes of H-CH₂, C-Si, C-C (sp³), C=O, and C-O were equal to 4.9, 4.5, 6.3, 7.8, and 11.2 eV, respectively. 68

Figure 3.6. Deconvolution of the C 1s XPS peaks obtained for the topmost surface layers of (a) pristine PDMS and the PDMS substrates irradiated by Ar ions with energies of (b) 360 eV, (c) 600 eV, and (d) 840 eV.	69
Figure 3.7. Bonding states of the Si 2p and C 1s signals obtained at etching times of 150–750 s and Ar ion energies of 300, 600, and 840 eV. (a) Si 2p at 360 eV, (b) Si 2p at 600 eV, (c) Si 2p at 840 eV, (d) C 1s at 360 eV, (e) C 1s at 600 eV, and (f) C 1s at 840 eV. The Si 2p and C 1s peaks of the as-received PDMS sample are also plotted as the bulk spectra.	71
Figure 3.8. DPA values plotted at various ion penetration depths and Si–O dissociation energy of 8.3 eV.	75
Figure 3.9. Calculation graph of Young's modulus values according to the thickness of hardskin layer.	78
Figure 3.10. Schematic diagram illustrating the generation of the heterogeneous hardskin layer consisting of the topmost and intermediate layers.	81
Figure 4.1. Ratio of the loss mode of the light generated in the OLED to the thickness of the electron transport layer. The light is emitted to the outside in the Air mode (red color).	90
Figure 4.2. Structure of the fabricated OLED device.	93
Figure 4.3. (a–e) SEM and (f–i) AFM images of the (a, f) bare PET surface and PET surfaces treated by the ion beam surface (b, g) 10 times, (c, h) 20 times, (d) 40 times, and (e, i) 60 times.	96
Figure 4.4. (a) Perpendicular transmittance and diffused transmittance plotted as functions of wavelength. At wavelengths below 400 nm, the absorption of the silver-colored PET material is very large. (b) Average total transmittance, perpendicular transmittance, diffused transmittance, and haziness values obtained in the	

wavelength region of 400–800 nm at different numbers of ion-beam treatments. (c) Diffuse transmittance values (symbols) obtained at different wavelengths and dashed fitting lines proportional to $(1/\lambda)^4$ that match the experimental data points in the region between 700 and 800 nm. 99

Figure 4.5. (a) Current–voltage characteristics (left axis) and luminescence–voltage characteristic (right axis), (b) current efficiencies, and (c) normalized emission spectra of the manufactured OLEDs. 103

Figure 4.6. Graphical summary of Chapter 4. 105

Figure 5.1. Diagrams of the a) ion beam treatment and copper sputtering processes, b) T-peeling test, and c) closed system used to evaluate aerosol filters. 117

Figure 5.2. a) Rate of change of area of the filter (black axis on the left), maximum process temperature reached during ion beam treatment (blue axis on the right), and the relative number of phonons generated as calculated by SRIM (red axis on the right) under ion beam irradiations of 1.45, 3.13, and 8.84 J/cm². b–e) Optical microscope images (scale bar: 100 μm) of the bare filter and the filters treated by Ion Beams 1, 2, and 3, respectively, under a dark field. The red-dashed circles show the areas where the fibers became agglomerated. 120

Figure 5.3. SEM (grayscale) and EDS mapping (color) images (scale bar: 100 μm) of the surfaces of the a) bare filter and b) copper-coated filter after ion beam treatment by Ion Beam 2. Atomic weight percentages of the surfaces of the c) bare filter and d) copper-coated filter after treatment by Ion Beam 2. 122

Figure 5.4. Optical microscope images (obtained under ultraviolet light with a peak wavelength of 360 nm; scale bar: 100 μm) of copper-coated filters treated with a) no ion beam (bare filter), b) Ion Beam 1, c) Ion Beam 2, and d) Ion Beam 3. 123

Figure 5.5. Peeling force per 10 mm of tape in the T-peeling test. 125

Figure 5.6. SEM images (scale bar, 50 micrometer) of the surface after peeling test a) tape surface and b) filter surface of bare, c) tape surface and d) filter surface treated under Ion Beam 1, and e) schematic diagram of the peeling test result of the untreated (bare) and ion beam–treated specimens. 126

Figure 5.7. a-d) Optical microscope images (scale bar, 100 micrometer) of copper coated on filter surface after peeling test bare, Ion Beam 1, Ion Beam 2, and Ion Beam 3 under ultraviolet with 360 nm of peak wavelength, respectively. e-f) Optical microscope images (scale bar, 100 micrometer) of tape surface after peeling test bare, Ion Beam 1, Ion Beam 2, and Ion Beam 3 under white light. 128

Figure 5.8. SEM and EDS mapping images (scale bar, 50 micrometer) of surface of copper-coated filter after tape peeling test of a) bare and b) Ion Beam 1. SEM and EDS mapping images (scale bar, 100 micrometer) of tape surface after tape peeling test of a) bare and b) Ion Beam 1. 129

Figure 5.9. Antibacterial properties of bare filter (control) and copper coated filter against *Staphylococcus aureus* ATCC 6538, *Klebsiella pneumonia* ATCC 4352, *Escherichia coli* ATCC 25922 and *Pseudomonas aeruginosa* ATCC 27853. 131

Figure 5.10. Antibacterial test results for a) *Staphylococcus aureus* ATCC 6538, b) *Klebsiella pneumoniae* ATCC 4352, c) *Escherichia coli* ATCC 25922, and d) *Pseudomonas aeruginosa* ATCC 27853. The left is the control group exposed to the normal filter, and the right is the experimental group exposed to the copper coated filter in each image. 132

Figure 5.11. a) images of copper coated filter and non-copper coated filter after spraying SARS-CoV-2 aerosol, b) images of crystal violet stained plaque assay plates, and c) inactivation of SARS-CoV-2. 134

Figure 5.12. Graphical summary of Chapter 5. 136

LIST of Tables

Table 3.1. Physical and optical properties of the PDMS samples after different Ar ions irradiations.	61
Table 3.2. Thicknesses of the hardskin layer (t_{hardskin}), Young's moduli of the hardskin layer (E_{hardskin}), and induced strain values obtained during substrate irradiation with an ion beam at various energies.	79
Table 4.1. Optical properties of the untreated and treated PET substrates.	97
Table 4.2. Averaged total transmittance, perpendicular transmittance, diffused transmittance, and haziness values determined in the wavelength region of 400–800 nm at different numbers of ion beam treatments.	100
Table 5.1. Vacuum ion-beam surface treatment and sputtering process conditions.	113

Chapter 1. Introduction

1.1. Nanostructures on Polymer Substrates

1.1.1. Polymer Nanostructures

Nanostructured surfaces possess physical and optical properties that are different from those of flat substrates, and their utilization in various fields has gradually increased in recent years [1–5]. Compared to a flat surface, the large specific surface area of a nanostructured surface facilitates chemical reactions and thus may be used as a catalyst or electrochemical electrode with enhanced adhesion properties. Optically, surface nanostructures can exhibit a plasmonic effect and good scattering and diffraction properties. In addition, it is possible to control the wettability of a substrate by maximizing its change in surface energy, thereby forming a surface that inhibits bacterial growth and mechanically changing its friction characteristics used for lubrication.

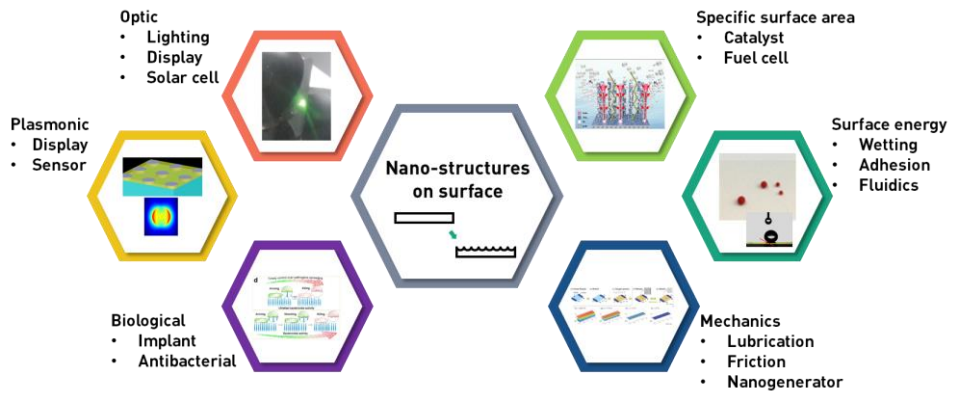


Figure 1.1. Various applications of nanostructures. [18, 36-38]

The existing nanostructure fabrication methods can be classified into top-down and bottom-up approaches. For example, lithography, nanoimprinting, and plasma etching are typical top-down methods, whereas hydrothermal growth and sol-gel coating are bottom-up techniques [6–11]. Lithography can produce very sophisticated patterns; however, because its processing step is complex and expensive, this technique is suitable for material that require very sophisticated processes (such as semiconductors), but not for films with large areas [6]. Nanoimprinting allows large-area processes and complex patterning and is less expensive than lithography [7]. However, its master mold fabrication step is expensive; moreover, if the mold and resin are not perfectly detached, resin residue is produced, which results in a defective product requiring a new master mold fabrication step. Lithography combined with the use of block copolymers can produce uniform nanopatterns without a mask [8]. The shape of the resulting nanostructure depends on the type and molecular weight of the block copolymer. However, it is difficult to form a nanostructure with a size of more than 100 nm, and the described approach requires a separate etching step. A plasma-based self-patterning method is inexpensive and easily scalable, although it is difficult to form a sophisticated and regular pattern using this technique [12–16].

Top - down

- Lithography (e-beam, photo, etc)
- Nanoimprinting
- Block copolymer self-assembly
- Plasma self-patterning

Bottom - up

- Hydrothermal growth
- Nanomaterial solution coating
- Sol-gel coating
- Vacuum deposition

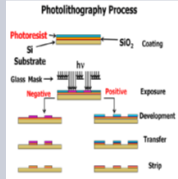
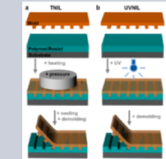
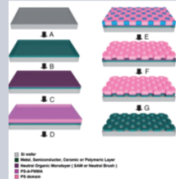
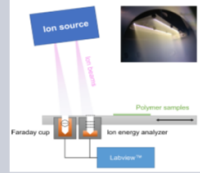
	Lithography	Nanoimprinting	Block copolymer self-assembly	Plasma self-patterning
Cost	Expensive	Moderate	Low cost	Low cost
Feature size	< 10 nm (EUV)	~ 5 nm	3 ~ 100 nm	10 ~ 1000 nm
Advantages	Regular patterning, high resolution	Regular patterning, fast process	No mask, uniformity, high pattern density	No mask, simple process, R2R process
Limitations	3d patterning, low throughput	Alignment, residue, expensive master mold	Simple structure, adjusting block for desire pattern	3d patterning, simple structure, low-uniformity
Process	 <p><i>J. Vac. Sci. Technol. B, (2013) 31, 3, May/June</i></p>	 <p><i>Polymers (2021), 13, https://doi.org/10.3390/polym13030445</i></p>	 <p><i>Soft Matter (2009), 5, 1568</i></p>	 <p><i>Applied Surface Science (2022) 572, 151452</i></p>

Figure 1.2. Classification of the existing nanostructure fabrication processes.

1.2. Closed Drift-Type Anode Layer Linear Ion Beam Source

1.2.1. Introduction

Plasma-based conventional patterning is typically performed using highly reactive toxic gases such as CF_4 and SF_6 at a radio frequency (RF) power. During this process, the surface is quickly etched via physical and chemical reactions; however, SF_6 is a representative greenhouse gas, and its usage is strictly regulated worldwide. Moreover, these two gases can easily corrode a metal-based vacuum chamber. Therefore, a plasma-based process using an environmentally friendly gas must be developed. Argon and oxygen are eco-friendly gases, but their chemical reactivities are lower than those the aforementioned fluorine-based gases. To compensate for this effect, it is necessary to increase the plasma ionization rate or physical etching rate. The energy of the ion beam generated by a closed drift-type anode layer linear ion-beam source (LIS) is easier to control than the energy of general RF plasma. In previous studies, a LIS was employed to release ions by efficiently controlling its internal structure, and the theoretical movement of internal charges will be described in the next chapter [17].

1.2.2. Theoretical Background

Figure 1.3 shows a schematic diagram of the shape and cross-section of LIS, which is mainly composed of the external ground electrode and internal cathode.

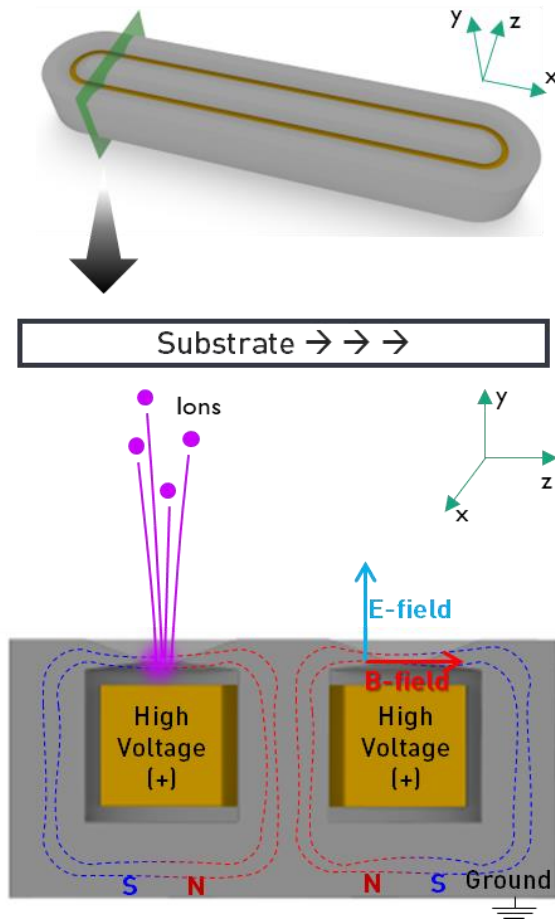


Figure 1.3. Structure and cross-section of LIS.

When a high voltage is applied to the anode and ground electrode of LIS, the injected gas molecules are separated to ions and electrons. A permanent magnet is present inside the ion-beam source to generate a magnetic field in the z-axis direction. The separated electrons and ions are driven by the electromagnetic force. The force of the charge is described by the following equation:

$$\vec{F} = m \frac{d\vec{v}}{dt} = q[\vec{E} + (\vec{v} \times \vec{B})] \dots \dots \dots (1.1)$$

where m is the charge mass, q is the charge amount, E is the applied electric field, v is the velocity of the charge, and B is the magnetic field generated by the permanent magnet. To simplify the equation, it is assumed that the magnetic field is formed only in the z-axis direction, while the electric field is formed along the y-axis.

$$\vec{B} = (0, 0, B), \vec{E} = (0, E, 0)$$

The following equations express the forces applied along the x-, y-, and z-axes.

$$\vec{F}_x = m \frac{dv_x}{dt} = q[\vec{E}_x + (v_x \times \vec{B}_x)] = qv_y B \dots \dots \dots (1.2)$$

$$\vec{F}_y = m \frac{dv_y}{dt} = q[\vec{E}_y + (v_x \times \vec{B}_x)] = q(E - v_x B) \dots \dots \dots (1.3)$$

$$\vec{F}_z = m \frac{dv_z}{dt} = 0 \dots \dots \dots (1.4)$$

They indicate that no force is applied in the z-axis direction (unlike the x-axis and y-axis directions). By combining these differential formulas with the calculated x, y, and z positions, the following equations can be derived:

$$x = \frac{qE}{m\omega^2}(\omega t - \sin \omega t) \dots \dots \dots (1.5)$$

$$y = \frac{qE}{m\omega^2}(1 - \cos \omega t) \dots \dots \dots (1.6)$$

where ω is the angular momentum, $\omega = qB/m$.

Equations (1.5) and (1.6) indicate that a charge inside LIS performs a cycloid motion. This movement in the x-axis direction, which reciprocates within a range of $2r$, is described by Equation 1.7 (Figure 1.4).

$$r = \frac{qE}{m\omega^2} \dots \dots \dots (1.7)$$

The radius of constrained electrons and cations can be calculated from the following parameters under the conditions used in this study. The mass of electron is 9.11×10^{-31} kg; the mass of the argon ion is 6.63×10^{-23} kg; the electron charge is 1.6×10^{-19} C; the magnetic field is 0.05 T; and the applied electric field is 500 V/mm (corresponding to an applied voltage of approximately 1000 V and gap between the anode and the ground equal to 2 mm). The electron transport radius is 1.14 mm, and the argon ion is 8.3×10^7 m. Electrons move cyclically at a diameter of 2.28 mm, and proceed in the x-axis direction due to the action of the ion beam. They continuously

collide with internal gas molecules in a chain-like manner, which accelerates the ionization process and increases the plasma density. The generated ions are emitted outside LIS due to the action of a repulsive electrical force and exhibit more complex behavior in the real environment, which requires theoretical simulations [17].

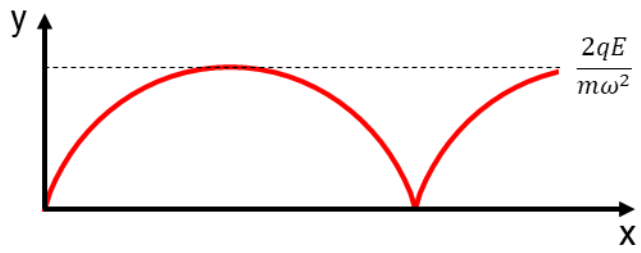


Figure 1.4. Cycloid motion of a charge inside LIS.

1.3. Surface Nanostructures Produced by Ion beam

1.3.1. Nano-hairy Structures of Polymers

Various nanostructures are formed when a polymer is irradiated with an ion beam. Their morphology depends on different process variables such as the polymer type, collision ion energy, collision ion dosage, and ion composition. For example, polyethylene naphthalate (PEN) has a nano-dimple structure; polydimethylsiloxane (PDMS) exhibits a nano-wrinkle structure; and polyethylene terephthalate (PET) possesses a nano-hairy structure.

Wang et al. has reported that nanostructures can be formed from protrusions or concaves present on the surface [14]. These structures were produced previously on various polymers such as poly(3,4-ethylenedioxythiophene) : poly(styrene-sulfonate) (PEDOT:PSS), polypyrrole (PPY), SU8, polyvinylidene fluoride (PVDF), poly(methyl methacrylate), polystyrene, and poly[2-methoxy-5-(2'-ethylhexyloxy)-1,4-phenylene vinylene] to prepare nanowire-sized organic light-emitting diodes (OLEDs). The ion collision angle on the surface containing protrusions and concaves depends on the collision position. The vertically collided ions transfer most energy to the polymer, leading to a higher degree of etching in the given region. Nanostructures are formed due to the differences between the etching rates of various ion collision positions. Their locations can be determined in advance by forming protrusions via imprinting.

Campo et al. etched polymer films by oxygen plasma and found that nanostructures could be aligned in specific directions depending on the crystallinity of the substrate [15]. In the case of a crystalline polymer such as PET or isotactic

polypropylene, the regions with high crystallinity are etched more weakly than the regions with low crystallinity.

Moon and co-workers fabricated nanorod-shaped structures on the surface of a polymer substrate through plasma etching and found that their formation occurred due to the presence of impurities [16]. When a voltage of -400 V is applied to the cathode, plasma ions collide with the cathode and polymer. The metal cathode is sputtered by the plasma, and the produced metal particles are deposited onto the polymer film. The coated metal species act as a mask influencing the etching rate of the polymer film.

1.3.2. Nano-wrinkle PDMS Structure

Many research groups reported nano-wrinkle PDMS structures fabricated by plasma irradiation [18–20]. For example, Yang and co-workers manufactured one-dimensional (1D) ripple patterns on the PDMS surface [18]. They increased PDMS wrinkles in the axial direction followed by surface curing with oxygen plasma. When the tension applied to PDMS returned to its original value, a ripple structure was formed on the PDMS surface with a ripple wavelength depending on the degree of tension.

Seo et al. demonstrated that the period and direction of a nano-wrinkle structure could be controlled by varying the irradiation angle of the ion beam [19]. When ion irradiation occurs at an angle perpendicular to the surface, the ion penetration depth increases, forming a thick silica (“hardskin”) layer on the surface. When the ion angle of incidence approaches the horizontal direction, the ion penetration depth becomes small, and a thinner silica layer is formed as compared with that produced by vertical irradiation. The authors concluded that the thin silica layer formed on the

surface contains a nanostructure with a short wrinkle wavelength and that the ion collision force applied in a specific direction influenced the directionality of the wrinkle pattern.

The period and amplitude of the produced PDMS wrinkle structure depend on the Young's modulus and Poisson's ratio of the cured surface layer. The wavelength (λ_0) and amplitude (A_0) of the wrinkle pattern are expressed by the following formulas:

$$\lambda_0 = 2\pi t \left(\frac{\bar{E}_{hardskin}}{3\bar{E}_{pdms}} \right)^{\frac{1}{3}} \dots \dots \dots (1.8)$$

$$A_0 = t \left(\frac{\varepsilon_0}{\varepsilon_c} - 1 \right)^{\frac{1}{2}} \dots \dots \dots (1.9)$$

$$\varepsilon_c = -\frac{1}{4} \left(\frac{3\bar{E}_{PDMS}}{\bar{E}_{hardskin}} \right)^{\frac{2}{3}} \dots \dots \dots (1.10)$$

$$\bar{E} = E / (1 - \nu^2) \dots \dots \dots (1.11)$$

where E is Young's modulus, ν is Poisson's ratio, t is the thickness of the hardskin layer, and ε_c is the critical strain.

1.3.3. Nano-dimple Structures of Semiconductor Materials

The polymer nano-dimple structure examined in this thesis has not been studied in detail. However, the structures fabricated on semiconductor materials by ion-beam irradiation have been reported a few decades ago [21–25]. Thus, Facsko's research

group irradiated the GaSb (100) surface by an argon ion beam with an ion density of 10^{17} – 10^{18} /cm² and energy of 0.42 keV to fabricate a GaSb nano-dot structure [21]. Wang et al. irradiated a Ge (100) substrate with a Ga⁺ ion beam to form periodic nanodots on the surface [22]. They elucidated the nanodot formation mechanism using the damped Kuramoto–Sivashinsky (DKS) model, which is described in the next chapter.

1.3.4. Interactions Between Ions and Matter

Ion-beam surface treatment may form a physically modified structure on the surface of a solid material or chemically modify its properties. This phenomenon is caused by physical collisions and the energy transferred through chemical reactions that occur during ions penetration. Its mechanism can be elucidated by examining the energy transfer of the ions penetrating the material [26, 27]. The permeated ions allow atoms and electrons in the material to escape from their original positions, and the minimum energy required for this process is called the displacement energy (E_d) [28]. The atoms with a separation energy exceeding the E_d energy are called primary knock-on atoms (PKAs). This energy is directly supplied from the outside through the energy transferred from the ions and can cause a collision. Meanwhile, when the energy transferred by ions is less than E_d , it generates a lattice vibration [29].

In the case of a polymer material, a polymer chain scission (during which a monomeric bond is broken by the energy of penetrated ions), cross-linking (recombination of broken chains), or generation of free radicals by atom detachment typically occurs. The parameter used to quantitatively express the ion energy required for these phenomena is dE/dx , which is the energy loss amount dE of penetrated ions per distance dx travelled in the depth direction (it is also called a

linear energy transfer or stopping power). Its value is affected by the initial energy of ions, angle of ion incidence, ion atomic weight, and material density. There are two different ways by which ions transfer energy: elastic collision (a collision between ions and atomic nuclei in the material structure) and inelastic collision due to the reaction between ions and electrons in the material structure [30]. The elastic collision between an ion and an atomic nucleus is called nuclear stopping; the inelastic collision between an ion and an electron is called electronic stopping; and the total dE/dx value of an ion penetrating the material can be expressed as the sum of the nuclear stopping (S_n), electron stopping (S_e), and charge exchange terms.

$$\left(\frac{dE}{dx}\right)_{loss} = \left(\frac{dE}{dx}\right)_{nuclear} + \left(\frac{dE}{dx}\right)_{electron} + \left(\frac{dE}{dx}\right)_{charge\ exchange} \dots (1.12)$$

The energy loss term due to charge exchange is relatively small and can be ignored.

$$\left(\frac{dE}{dx}\right)_{loss} = \left(\frac{dE}{dx}\right)_{nuclear} + \left(\frac{dE}{dx}\right)_{electron} = S_n + S_e \dots \dots (1.13)$$

Here, S_n and S_e refer to the energy losses due to nuclear and electron stops, respectively, which are affected by the ion energy and material density. Various models have been proposed to derive their values over decades. Nanostructure formation is caused by the separation of atoms in the material; therefore, nuclear stopping represents the primary energy transfer path [31]. The formula for calculating the energy loss due to nuclear stopping can be derived by applying the

Coulomb repulsive force and electron screening potential at nuclear shutdown resulting from the elastic collision between ionic and atomic nuclei.

$$\left(\frac{dE}{dx}\right)_{nuclear} = S_n = N \frac{\pi^2}{2} Z_1 Z_2 e^2 a \frac{M_1}{M_1+M_2} \dots \dots \dots (1.14)$$

where N is the atomic density of the target, Z_1 is the charge of the ion, Z_2 is the charge of the target, M_1 is the atomic mass of the ion, M_2 is the atomic mass of the target, and a is the Thomas–Fermi screening radius for collision.

The electronic energy loss of an ion in the solid is expressed by the following equation:

$$\left(\frac{dE}{dx}\right)_{electron} = S_e = \frac{4\pi e^4 Z_p^2 Z_t N_t}{m_e v^2} \times \left[\ln\left(\frac{2m_e v^2}{I}\right) - \ln\left(1 - \frac{v^2}{c^2}\right) - \frac{v^2}{c^2} \right] \dots (1.15)$$

where v is the velocity, Z_p is the charge of the projectile ions, Z_t is the atomic number, N_t is the number density of target atoms, m_e is the electron rest mass, e the electronic charge, and I is the average excitation and ionization potential of the target.

As described above, polymeric bonds are broken and recombined by the energy transferred by ions. This process involves bond cleavage and polymer cross-linking through nuclear stopping, and its activity increases with increasing ion irradiation intensity. As a result, the physical and chemical interactions of ions that occur during the ion-beam treatment change the polymer surface morphology and chemical structure.

1.3.5. Computational Analysis

The Stopping and Range of Ions in Matter (SRIM) software is a Monte Carlo calculation-based simulation program that quantum-mechanically examines the physical collisions between ions and particles in the target material during ion penetration and can be used to calculate the stopping power and penetration distance [32–25]. The ion energy transfer occurring inside a material may be evaluated from the penetration depth. The incoming ions interact with atoms and electrons in the target material, which results in atomic dissociation, electron excitation, and plasmon generation. Note that ion–target interactions are strongly affected by the electronic structure, interatomic bonding structure, ion type, and ion energy. Figure 1.5 shows the input window of the SRIM calculation process that is used to specify the ion species and energy, target atom species, atomic ratios, and density of the target material. By performing SRIM simulations, it is possible to calculate the distribution of ions along the depth direction, ionization rates of target elements, number of phonons generated in the target, longitudinal and lateral ion projection ranges, and sputtering field. Figure 1.6 displays the SRIM calculation output including numerical data, which can be used for DKS modeling and displacement-per-atom (DPA) calculations.

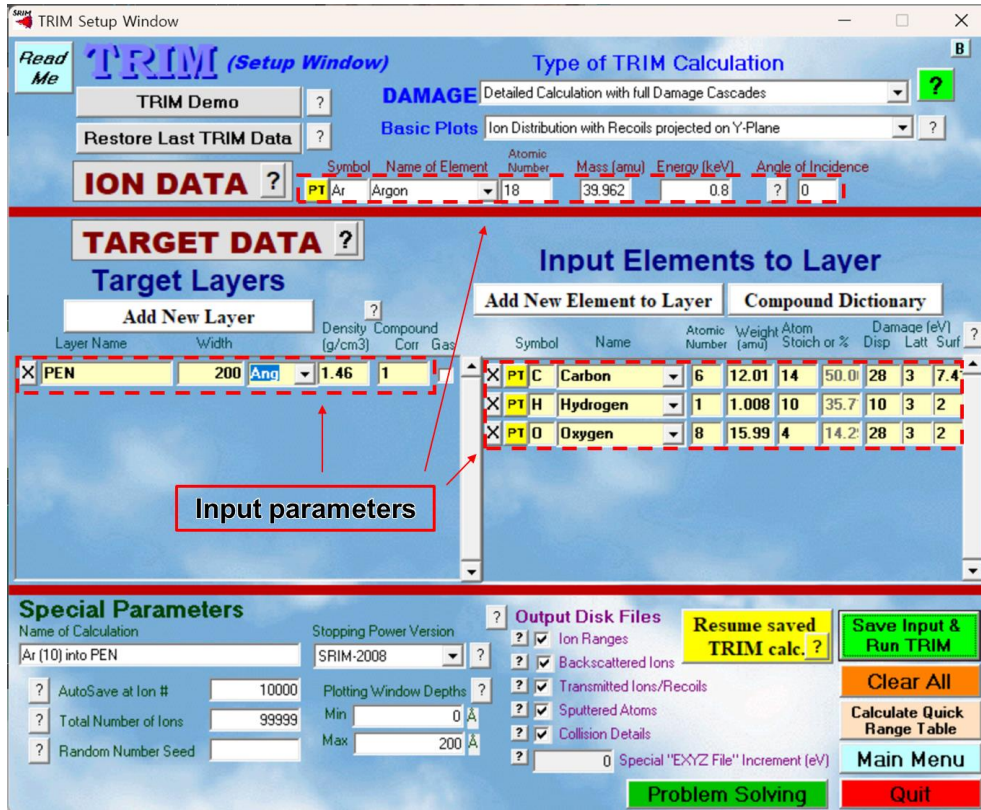


Figure 1.5. Interface for entering calculation parameters into SRIM, including the ion type, ion energy, substrate density, and atomic species.

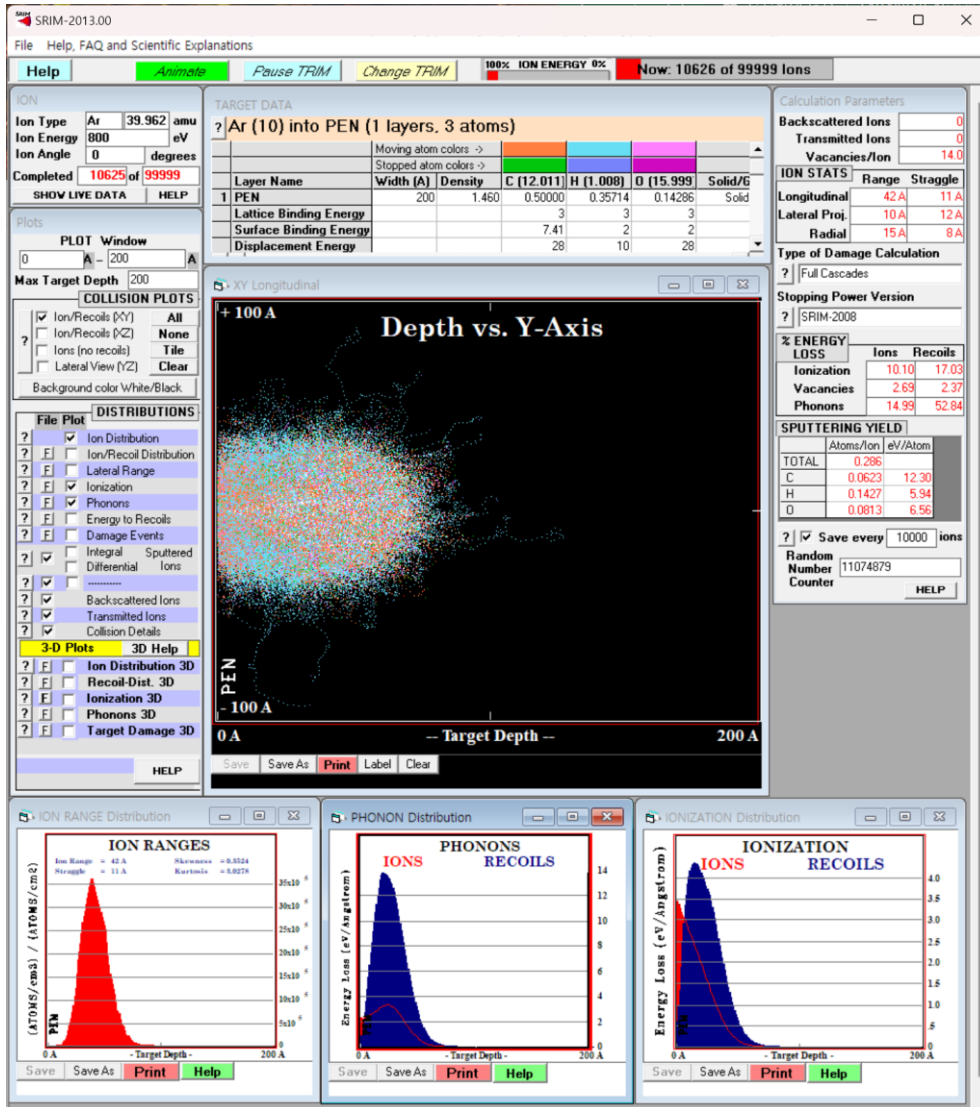


Figure 1.6. SRIM window showing the calculation results. Various physical parameters characterizing the ion collision with a medium, such as the longitudinal and lateral ion distributions, numbers of recoil ions and phonons, and sputtering yield, can be determined.

1.4. Purpose of This Research Study

As mentioned above, numerous studies have been conducted to examine various nanostructures formed on the polymer surface through plasma or ion irradiation and elucidate its underlying mechanism. Most of these studies qualitatively investigated the principle of nanostructure formation; however, very few of them attempted to quantify this process because unlike metals and ceramics, polymers contain different bond types despite the same molecular structure. In this work, an analysis method mainly utilized for describing the formation of nanostructures in metals and ceramics is applied to polymers. The SRIM calculation software can determine various parameters characterizing the collision of particles with a medium, including the amount of transferred energy that depends on the medium and ion species, energy transfer type, and sputtering field. Because this program does not consider polymer bonding, it is not particularly suitable for studying polymers and mainly employed for semiconductors, ceramics, and metallic materials. This work shows that SRIM calculations can be performed to describe changes occurring on the polymer surface.

The formation a nano-dimple structure on a PEN surface is discussed in Chapter 2, while a PDMS wrinkled structure is discussed in Chapter 3. Chapters 4 and 5 describing different applications of nanostructures show that the nano-hairy structure formed on the PET surface can be used in OLEDs to increase their efficiency and explore process conditions that enable surface treatment while suppressing the formation of nanostructures.

1.5. Bibliography

1. J. Cai and L. Qi, Recent advances in antireflective surfaces based on nanostructure arrays. *Royal Society of Chemistry* (2015) 2, 37-53
2. Z. Wang, P. Liu, J. Han, et al., Engineering the internal surfaces of three-dimensional nanoporous catalysts by surfactant-modified dealloying. *Nature Communications* (2017) 8, 1066, <https://doi.org/10.1038/s41467-017-01085-3>
3. Y. Li, M. Kovačič, J. Westphalen, et al., Tailor-made nanostructures bridging chaos and order for highly efficient white organic light-emitting diodes. *Nature Communications* (2019) 10, 2972, <https://doi.org/10.1038/s41467-019-11032-z>
4. J. Huang, Y. Lai, L. Wang, et al., Controllable wettability and adhesion on bioinspired multifunctional TiO₂ nanostructure surfaces for liquid manipulation. *J. Mater. Chem. A*, (2014) 2, 18531-18538
5. D. P. Linklater, V. A. Baulin, S. Juodkazis, et al., Mechano-bactericidal actions of nanostructured surfaces. *Nat Rev Microbiol* (2021) 19, 8–22, <https://doi.org/10.1038/s41579-020-0414-z>
6. N. Riegel, C. Middlebrook, K. Kruse, M. Roggemann, Using the 3D beam propagation method to model the effects of lithographic roughness on the attenuation of highly multimodal polymer waveguides. *Journal of Vacuum Science & Technology B* (2013) 31, 031206, <https://doi.org/10.1116/1.4802979>
7. M. Handrea-Dragan, Multifunctional Structured Platforms: From Patterning of Polymer-Based Films to Their Subsequent Filling with

- Various Nanomaterials. *Polymers* (2021), 13, <https://doi.org/10.3390/polym13030445>
8. W. van Zoelen, G. ten Brinke, Thin films of complexed block copolymers. *Soft Matter* (2009) 5, 1568
 9. J. -Y. Yang, S. -G. Park, S. Jung, et al., SERS substrates based on self-organized dimple nanostructures on polyethylene naphthalate films produced via oxygen ion beam sputtering. *Applied Surface Science* (2022) 572, 151453
 10. J. Park, T. H. Lee, C. Kim et al., Hydrothermally obtained type-II heterojunction nanostructures of In₂S₃ / TiO₂ for remarkably enhanced photoelectrochemical water splitting. *Applied Catalysis B: Environmental* (2021) 295, 120276
 11. G. N. Kozhemyakin, S. A. Kiiko, O. E. Bryl, Formation of Indium Nanoparticles by Thermal Evaporation. *Crystallogr. Rep.* (2019). 64, 457–460,
 12. J. -Y. Yang, S. Jung, E. -Y. Byeon et al., Preliminary Validation of a Continuum Model for Dimple Patterns on Polyethylene Naphthalate via Ar Ion Beam Sputtering. *Polymers* (2021), 13, 1932
 13. S. Lee, E. Byeon, S. Jung, D. -G. Kim, Heterogeneity of hard skin layer in wrinkled PDMS surface fabricated by Ar ion-beam irradiation. *Scientific Reports* (2018) 8:14063, doi:10.1038/s41598-018-32378-2
 14. L. Wang, A. Rastelli, S. Kiravittaya, et al., Self-Assembled Quantum Dot Molecules. *Adv. Mater.*, (2009) 21, 2601-2618. <https://doi.org/10.1002/adma.200803109>

15. J. P. Fernández-Blázquez, C. Serrano, C. Fuentes, A. Campo, Distinct Nanopatterns on Dry Etched Semicrystalline Polymer Films Controlled by Mechanical Orientation. *ACS Macro Letters* (2012) 1, 5, 627-631
16. T. -J. Ko, K. H. Oh, M. -W. Moon, Plasma-Induced Hetero-Nanostructures on a Polymer with Selective Metal Co-Deposition, *Advanced Materials Interfaces* (2015) 2, 1400431
17. S. Lee, J. Kim, D. -G. Kim, Effects of electrode geometry on the ion beam extraction of closed drift type anode layer linear ion source, *The Review of scientific instruments* (2012) 83, 2, 02B703
18. P. -C. Lin, S. Vajpayee, A. Jagota, et al., Mechanically tunable dry adhesive from wrinkled elastomers. *Soft Matter* (2008) 4, 1830-1835
19. H. -C. Jeong, H. -G. Park, Y. H. Jung et al., Tailoring the Orientation and Periodicity of Wrinkles Using Ion-Beam Bombardment. *Langmuir* (2016) 32, 28, 7138–7143
20. S. Yang, K. Khare, P. -C. Lin, et al., Harnessing Surface Wrinkle Patterns in Soft Matter. *Advanced Functional Materials* (2010) 20, 16, 2550-2564
21. S. Facsko, T. Dekory, C. Koerdt, et al, Formation of Ordered Nanoscale Semiconductor Dots by Ion Sputtering, *Science* (1999) 285, 1551-1553
22. Q. Wei, X. Zhou, B. Joshi, et al., Self-Assembly of Ordered Semiconductor Nanoholes by Ion Beam Sputtering, *Advanced Materials* (2009) 21, 28, 2865-2869

23. Q. Wei, Self-organized Nanoscale Patterning under Ion Beam Irradiation', (2009) Univ. Michigan, Ph.D. thesis
24. M. Castro, R. Cuerno, L. Vazquez and R. Gago, Self-organized ordering of nanostructures produced by ion-beam sputtering. *Physical Review Letters* (2005) 94, 1, 016102
25. F. Frost, A. Schindler, F. Bigl, Roughness Evolution of Ion Sputtered Rotating InP Surfaces: Pattern Formation and Scaling Laws. *Physical Review Letters* (2000) 85, 19, 4116
26. P. Jain, G. Agarwal, Ion beam induced surface and interface engineering. *Surf. Sci. Rep.*, (2011) 66, 3–4, 77–172
27. E. Rutherford, The scattering of α and β particles by matter and the structure of the atom. *Philos. Mag.* (1912), 92, 4, 379–398
28. M. Terasawa, Coulomb explosion following electronic excitation in ion-solid interaction. *Vacuum* (2006) 81, 2, 142–149
29. R. Behrisch, Sputtering by particle bombardment: Physical sputtering of single-element solid. (1981)
30. R. M. Papaleo, A. Hallén, B. U. Sundqvist, et al., Chemical damage in poly (phenylene sulphide) from fast ions: dependence on the primary-ion stopping power. *Phys. Rev. B* (1996) 53, 5, 2303
31. Y. P. Karade, Ion beam induced micro-structuring of polymeric surfaces. (2010) Technische Universiteit Eindhoven
32. M. Guenther, G. Gerlach, G. Suchaneck, et al., Ion-beam induced chemical and structural modification in polymers. *Surf. Coat. Technol.* (2002) 158–159, 108–113.

33. E. H. Lee, Ion-beam modification of polymeric materials fundamental principles and applications. *Nucl. Instrum. Methods Phys. Res. B* (1999) 151, 29–41.
34. M. F. Zaki, Effect of Ar ion on the surface properties of low density polyethylene. *Spectrochim. Acta. A Mol. Biomol. Spectrosc.* (2016) 159, 177–183
35. F. Ziegler, SRIM-2003. *Nucl. Instrum. Methods Phys. Res. B* (2004) 219–220, 1027–1036
36. Lee, J. Y. Park, S. Gim, et al., Spontaneously Formed Nanopatterns on Polymer Films for Flexible Organic Light-Emitting Diodes. *Small* (2015) 11, 35, 4480-4484
37. L. Luo, Y. Zhou, X. Xu, et al., Progress in construction of bio-inspired physico-antimicrobial surfaces. *Nanotechnology Reviews* (2020) 9, 1, 1562-1575
38. S. Choi, J. Hwang, T. H. Lee, et al., Photoelectrochemical Hydrogen Production at Neutral pH Phosphate Buffer Solution Using TiO₂ Passivated InAs Nanowire/p-Si Heterostructure Photocathode. *Chemical Engineering Journal* (2020) 392, 123688

Chapter 2. Principles of Formation of Nano-dimple Structures on PEN Substrate

2.1. Introduction

Since the self-organization of nano-dots by ion-beam sputtering was introduced by Facsko, diverse nano-structures have been fabricated by ion-beam sputtering on semiconductor surfaces [1,2,3]. Regular ripples and dots have been created on the surfaces of Si, InP, and GaSb by noble gas ion-beam irradiation [1,4,5,6,7]. Ion-induced surface instability results in self-organization, which has been successfully described by a continuum model including terms of roughening and smoothing [8]. The continuum model accounts for different sputtering yields at peaks and troughs, dependency on the ion's incident angle, ion-induced effective surface diffusion, thermal diffusion, and surface viscous flow [9]. The similarity between experimentally observed surface morphology and theoretical calculation showed the possibility of exact prediction for self-organization by ion-beam sputtering. Nano-dots, ripples, and dimples on polymer substrates also have been observed in surface treatments using ion-beam irradiations. M. Goyal reported that a 40 keV oblique argon ion-beam resulted in ripple or dot nano-structures on polypropylene (PP) surfaces [10]. We reported that dimple nano-structures were obtained by 1 keV oxygen ion-beam treatments on polyethylene terephthalate (PET) surfaces [11]. Polyethylene naphthalate (PEN) surfaces irradiated by an argon ion-beam showed dimple patterns, which resembled the patterns calculated by the continuum equation, especially the Kuramoto–Sivashinsky (KS) model [9]. This similarity implied the possibility of applying the continuum equation to describe the self-organization of polymer surfaces by noble gas ion-beam sputtering. In this work, we fabricated dimple patterns on PEN surfaces via 600 eV argon ion-beam irradiation. Surface analysis was performed to find a clue regarding whether ion-beam sputtering was

the main reaction making the dimple patterns. A nonlinear continuum equation was solved by MATLABTM software and compared to the dimple patterns obtained by argon ion-beam irradiation.

2.2. Materials and Methods

2.2.1. Materials

A dimple pattern was fabricated on a commercially available PEN film surface by argon ion-beam bombardment. 125 μm PEN film (Dupont Teijin Films, Chester, VA, USA) was prepared by cutting it to a size of 100 mm \times 100 mm. After removing the protective film on the surface, the PEN film was attached to the linear moving stage located in the vacuum chamber.

2.2.2. Ion Beam Treatment

The vacuum chamber was evacuated with a base pressure of 5.0×10^{-5} Torr, and then argon gas was injected into the linear ion source. A gridless ion source was used to generate linear argon ion-beams with a width of 300 mm [11,12]. The PEN samples were treated at a linear moving speed of 10 mm/s. The ion dose per scan was 1.2×10^{14} / cm^2 , according to measurement by a Faraday cup. The ion energy distribution function was measured by an ion energy analyzer (Figure 2.1.) [13]. argon ion-beams were irradiated under normal incidence conditions.

2.2.3. Field-Emission Scanning Electron Microscopy

The PEN surface was observed using field-emission scanning electron microscopy (FE-SEM; JSM 6700F, JEOL, Tokyo, Japan) in secondary electron (SE) mode. The accelerating voltage was maintained at 5 kV.

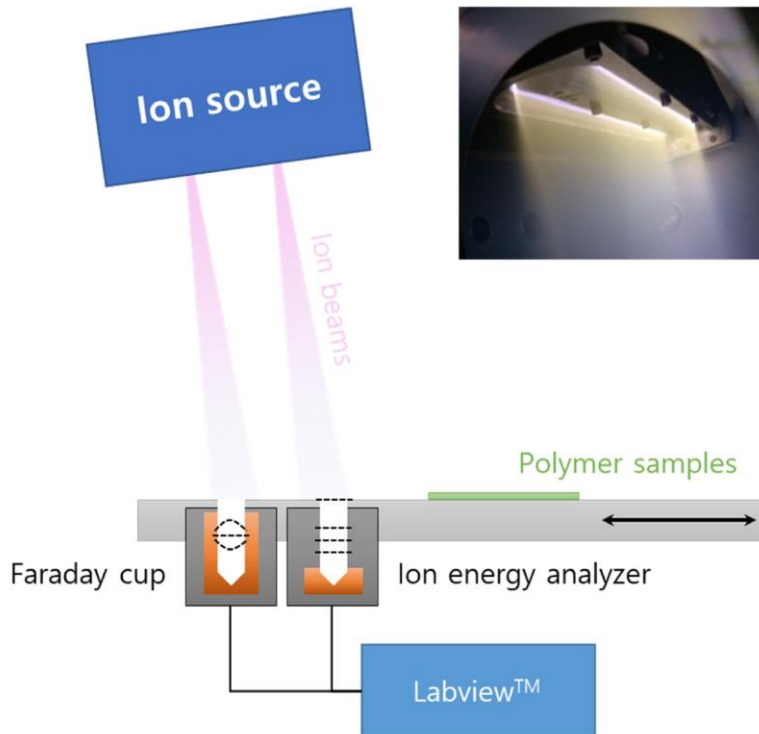


Figure 2.1. Linear ion-beam irradiation on a moving substrate (speed: 10 mm/s). Ion current density and ion energy distribution function were measured by Faraday cup and retarding potential ion energy analyzer, respectively.

2.2.4. Atomic Force Microscopy

The morphology of the dimple nano-structures was measured by atomic force microscopy (AFM, NX10, Park Systems, Korea) in non-contact mode.

2.2.5. Field-Emission Transmission Electron Microscopy and the Electron Energy Loss Spectrum

A localized cross-linking on the dimple nano-structures was verified via cross-sectional field-emission transmission electron microscopy (FE-TEM, JEM-ARM, JEOL, Tokyo, Japan) with electron energy loss spectroscopy (EELS, JEOL, Tokyo, Japan). The FE-TEM measurements were performed at an accelerating voltage of 200 kV. The cross-sectional specimens of FE-TEM were prepared using a liquid metal ion source (Ga^+) equipped with a focused ion-beam with a coarse milling current (4 nA) and a fine milling current (20 pA) at 30 kV. The 90 nm-thick PEN sample was prepared with a focused ion-beam.

2.3. Results and Discussion

Figure 2.2 shows surface morphologies and profiles. Figure 2.2 a,b show AFM images of PEN surfaces treated by 600 eV argon ion-beam bombardment with ion doses of $2.4 \times 10^{15} / \text{cm}^2$ and $4.8 \times 10^{15} / \text{cm}^2$, respectively. As the ion dose was increased, the irregular dimple patterns were formed clearly. In Figure 2.2 c,d, the peak-to-peak roughness (Rz) was increased from 29.1 ± 4.7 nm and 53.4 ± 8.4 nm as the ion dose was increased. In Figure 2.2 e, a scanning probe image processor (SPIPTM, Image Metrology, Diplomvej, Denmark) showed that dimple diameter was increased from 63.4 ± 18.6 nm to 77.6 ± 23.1 nm as the ion dose was increased (Figure 2.3). In addition, the aspect ratio (Rz/diameter) of dimples were increased from 0.45 to 0.68.

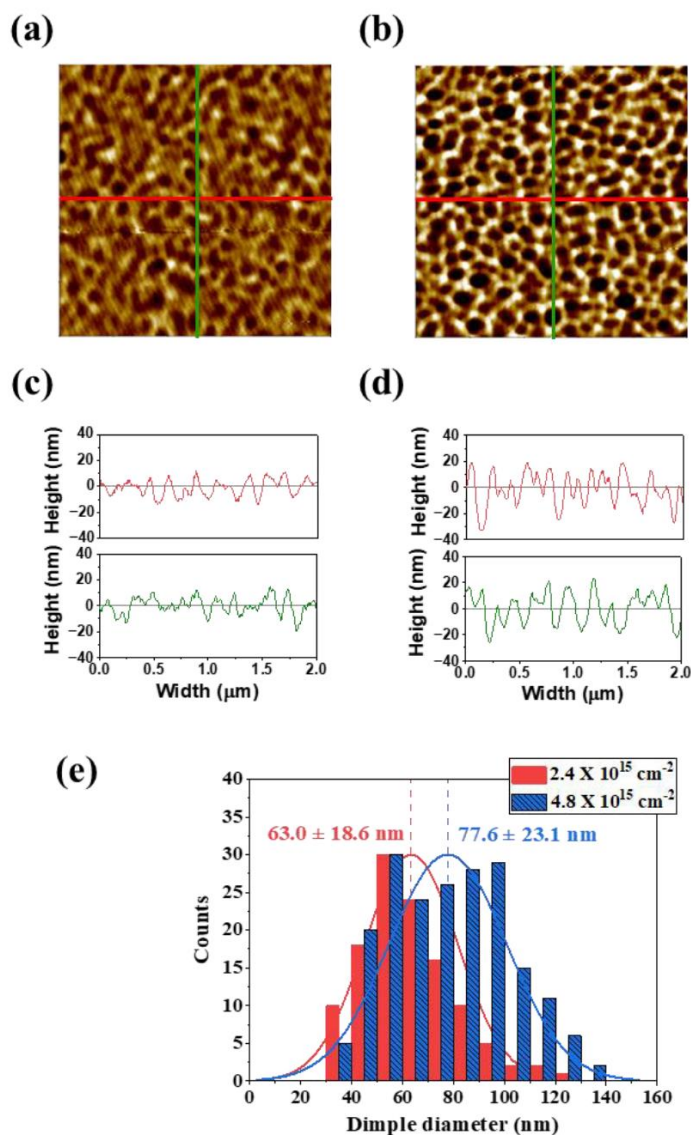
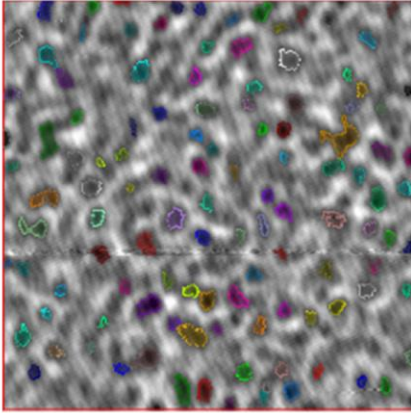


Figure 2.2 AFM images (area: $2 \mu\text{m} \times 2 \mu\text{m}$) of dimple patterns on a PEN surface by 600 eV argon ion-beam bombardment with ion doses of (a) $2.4 \times 10^{15} / \text{cm}^2$ and (b) $4.8 \times 10^{15} / \text{cm}^2$. X-axis and Y-axis line profiles: (c) $2.4 \times 10^{15} / \text{cm}^2$, (d) $4.8 \times 10^{15} / \text{cm}^2$. (e) Distribution of dimple diameter in the $2 \mu\text{m} \times 2 \mu\text{m}$ area.

(a)



(b)

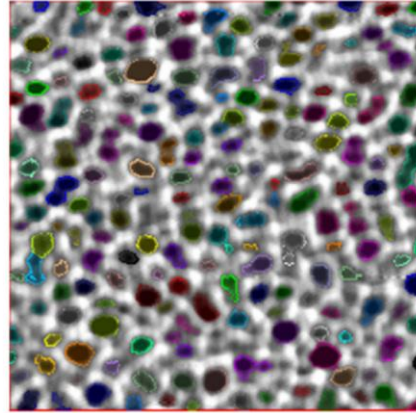


Figure 2.3. Diameter measurement of dimple structure using SPIP™ software, (a) ion dose: $2.4 \times 10^{15} /\text{cm}^2$, (b) ion dose: $4.8 \times 10^{15} /\text{cm}^2$.

Self-organization by ion-beam irradiation has been explained by two mechanisms. One is the semi-crystallinity of cross-linked polymers. The sputtering yield of a semi crystalline polymer is lower than that of the amorphous phase [14]. For instance, He ion bombardment on polytetrafluoroethylene surfaces left the backbones of the crystallized polymer chains, which formed worm-like structures [15]. Another possibility is surface instability induced by ion bombardments. Ion-induced surface instability results in roughening and smoothing of the amorphous layer [2]. The self-organization of ordered morphologies by ion-beam sputtering is independent from the orientation of surface materials because self-organization by surface instability occurs in the amorphous layer formed by ion-beam irradiation [2]. If the polymer surface is in the amorphous phase during ion-beam sputtering, ion-induced surface instability could explain the pattern formation. In Figure 2.4, FE-TEM and EELS show the cross-sectional images and the chemical bond statuses at the valleys and hills of the dimple structures. The EELS was measured at the peak (point A in Figure 2.4a) and trough (point B in Figure 2.4b). The EELS signal showed aromatic C=C (285 eV), ketone C=O (286.3 – 286.8 eV), and aldehyde O=CH (286.3 – 286.8 eV) functional groups, which existed similarly at the peak and trough [16]. If the partially distributed crystalline chains induced the dimple patterns, the binding status at the peak position would differ from that at the trough region. This revealed that the patterning mechanism was not partial semi-crystallization. Wide angle X-ray scattering (WAXS) showed that semi-crystallization was not induced by argon ion-beam irradiation (Figure 2.5). The EELS and WAXS results mean that the self-organization on the PEN samples could be due to the ion-induced surface instability of the amorphous layer.

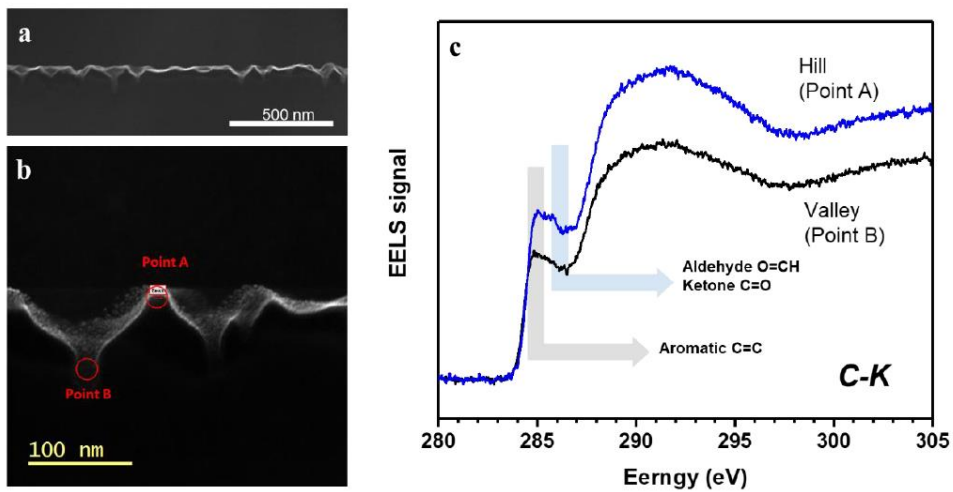
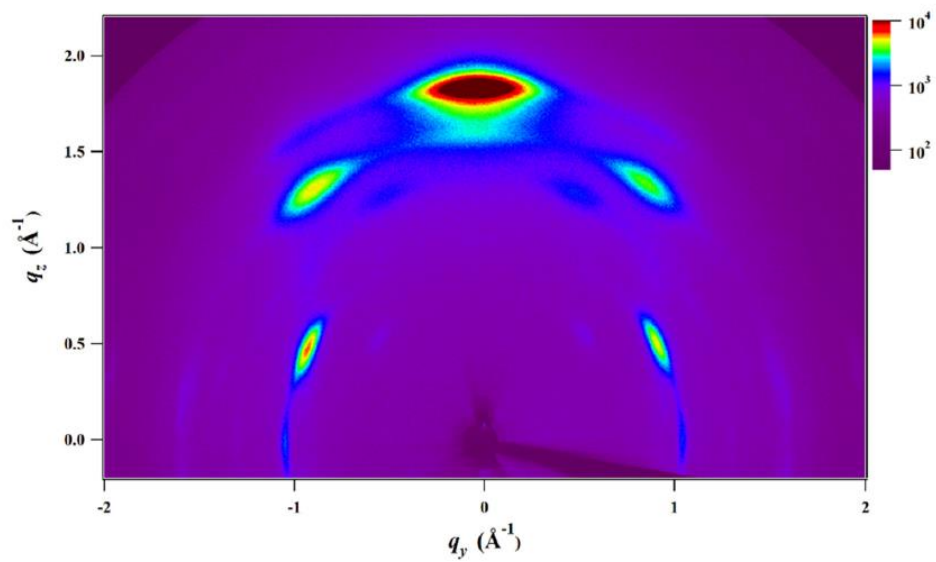


Figure 2.4. (a) Cross-sectional SEM image of dimple pattern, (b) the points of EELS measurement at a peak and trough. (c) EELS at the selected peak and trough

(a)



(b)

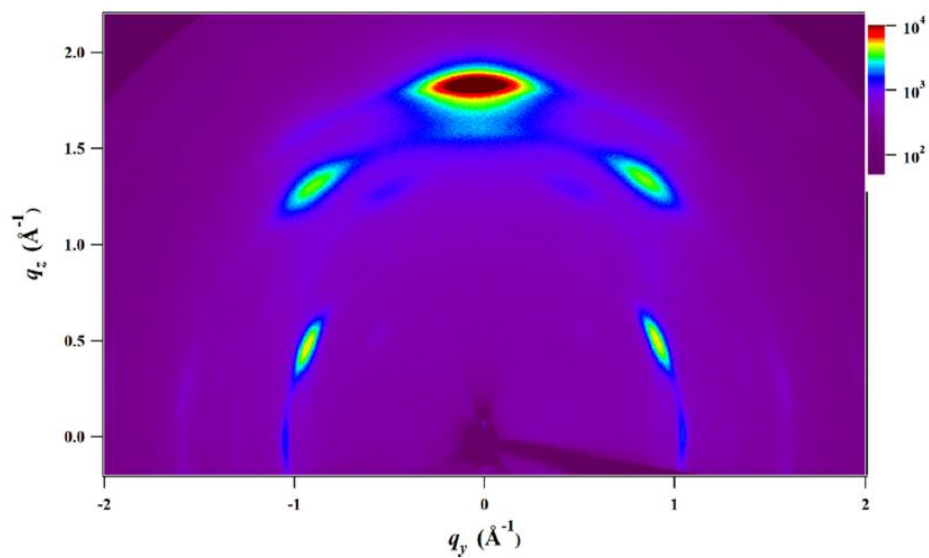


Figure 2.5. Spectrum of wide angle X-ray scattering, (a) as-received PEN, (b) 600 eV argon ion-beam irradiated PEN.

The KS model could explain the self-organization of dimple structures on the PEN surface by ion-induced surface instability. The mechanism of pattern formation by ion bombardment has been extensively investigated using a continuum equation [8,9]. The KS Equation describes the morphology evolution during an ion bombardment. The KS Equation is given by

$$\frac{\partial h}{\partial t} = (v\nabla^2 - D\nabla^4 - K\nabla^4)h - \lambda(\nabla h)^2 + \eta \dots \dots \dots (2.1)$$

where h is the height of the ion-bombarded surface as a function of time t , n is the effective surface tension generated by the erosion process or viscous flow due to surface stress, D is the diffusion coefficient from ion-induced diffusion, K is a thermal diffusion coefficient, λ describes the tilt-dependent sputtering yield, and η is Gaussian white noise resulting from the stochastic nature of the erosion process. We tried to reproduce the dimple structures on PEN surfaces by argon ion-beam irradiations using the KS model. Numerical simulation was executed on an equally spaced, 2-dimensional 200×200 mesh by integration of Equation 2.1 using a standard discretization method with periodic boundary conditions. The integration began from a random surface with a height randomly distributed from 0 to 0.1 with spatial step $dx = 0.5$ nm, time step $dt = 0.002$ s, $n = -0.0553$ nm²/s, $\lambda = -0.177$ nm/s, $D = 0.0138$ nm⁴/s, and $K = 0$. The coefficients were calculated by ion species (argon), polymer density (1.36 g/cm³), ion energy (600 eV), and a definition of coefficients from previous work [8,17]. The sputtering yield was calculated by SRIM [17]. The sign of the nonlinear term λ determined dot or dimple structures. A positive λ induced dot formation and a negative λ described dimple formation [2,8]. In this normal

incident condition, Equation 2.1 yielded an isotropic, partial differential equation with a negative nonlinear λ term, which implied dimple formation. Figure 2.6 compares simulation results using Equation 2.1 with FE-SEM images of experimentally fabricated samples. The images reveal a similarity of surface morphology between the simulation and the experiment. In the simulation, the disconnected patterns developed after 50 s, which corresponded to 20 scans (Figure 2.6a). After 100 s (40 scans), dimple patterns formed (Figure 2.6b). As experimental bombardment proceeded (Figure 2.6c), a partially disconnected network structure was observed after 20 scans. For longer irradiation times, the pattern formed after 40 scans (Figure 2.6d). The spatiotemporal pattern predicted by Equation 2.1 showed good correlation with experimental observations.

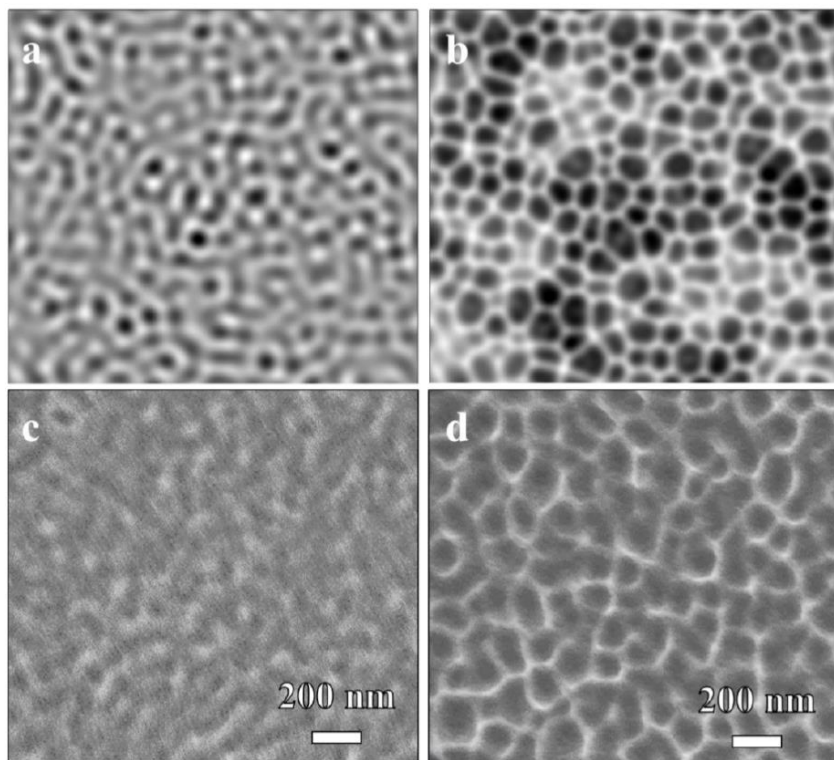


Figure 2.6. Simulation results by iterating the DKS Equation: (a) ion flux = 4.83×10^{13} / $\text{cm}^2\cdot\text{s}$, time = 50 s for 20 scans (b) ion flux = 4.83×10^{13} / $\text{cm}^2\cdot\text{s}$, time = 100 s for 40 scans. Experimentally obtained dimple patterns on the PEN surface: (c) 20 scans, (d) 40 scans.

The successful prediction of self-organization means that ion-beam irradiation on the PEN surface mainly results in surface sputtering. The continuum equation is based on the sputtering reaction on the ion-beam irradiated surface. Ion irradiation on the polymer surface simultaneously induces cross-linking and sputtering. Ion energy transfer by nuclear collision affects the ratio of cross-linking to sputtering. If surface atoms receive sufficient energy to break surface binding with energetic recoils and ions, surface displacement induces sputtering. Energy transfer by recoils and ions depends on the atomic number density of the target polymer. The concept of displacement per atom (DPA), which is proportional to the energy transfer by the nuclear stopping reaction, could be a quantitative value for evaluating the degree of displacement [18]. PEN density (1.36 g/cm^3) was sufficient to induce multiple atomic displacements of polymer atoms at the surface. The 600 eV argon collision on the PEN surface showed a DPA of 4 to 8, a value sufficient for inducing frequent sputtering by ion bombardments. Thus, the continuum model based on sputtering reactions showed similar surface morphology to an argon ion-beam irradiated PEN surface.

2.4. Conclusions

The comparison of the KS model and the dimple pattern showed the validity of applying the continuum model to the self-organization of a polymer surface using ion-beam irradiation. The continuum model based on sputtering reactions could be applied to the limited polymer material, which has a density that induces sufficient surface displacement and sputtering by ion-beam irradiation.

The discrepancy between the simulation and the experiment is due to a limitation in explaining the exact ion-induced sputtering yield of the polymer substrate that consists of several atoms such as carbon, hydrogen, and oxygen. The SRIM code supplied a statistically averaged sputtering yield for the polymer substrate.

This approach could be useful to fabricate nano-structures applied to sensors such as surface-enhanced Raman spectroscopy, which uses the enhancement of local electric fields wherein the surface morphology has a several nm gap [19,20]. The dimple patterns could be applied to form hot spots on polymer surfaces using a simple, top-down process.

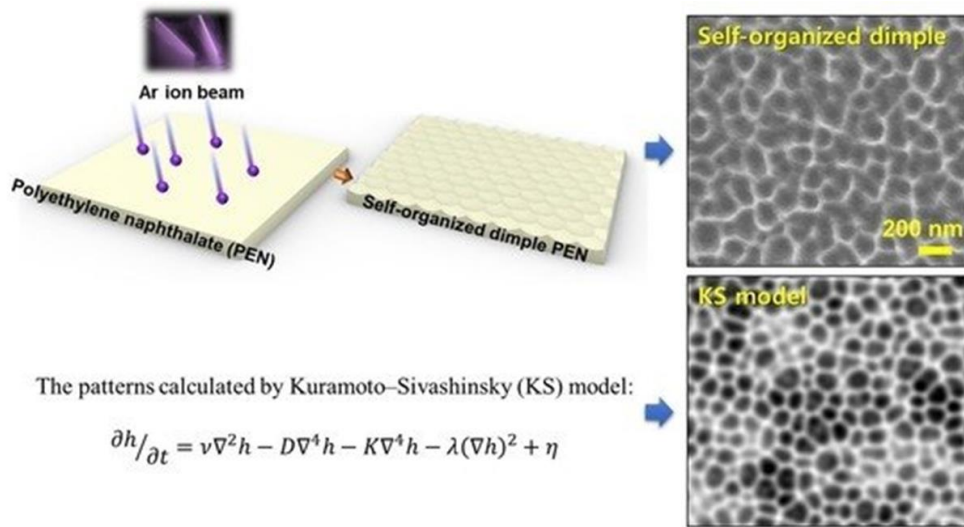


Figure 2.7. Graphical summarization of Chapter 2. The nano-dimple structure of the PEN surface was fabricated using an argon ion-beam, and the structure was similar to the result calculated through the DKS model.

2.5. Bibliography

1. Facsko, S.; Dekorsy, T.; Koerdt, C.; Trappe, C.; Kurz, H.; Vogt, A.; Hartnagel, H.L. Formation of ordered nanoscale semiconductor dots by ion sputtering. *Science* **1999**, *285*, 1551–1553.
2. Wei, Q.; Zhou, X.; Joshi, B.; Chen, Y.; Li, K.; Wei, Q.; Sun, K.; Wang, L. Self-Assembly of Ordered Semiconductor Nanoholes by Ion Beam Sputtering. *Adv. Mater.* **2009**, *21*, 2865–2869.
3. Castro, M.; Cuerno, R.; Vázquez, L.; Gago, R. Self-organized ordering of nanostructures produced by ion-beam sputtering. *Phys. Rev. Lett.* **2005**, *94*, 16102.
4. Bobek, T.; Facsko, S.; Kurz, H.; Dekorsy, T.; Xu, M.; Teichert, C. Temporal evolution of dot patterns during ion sputtering. *Phys. Rev. B* **2003**, *68*, 85324.
5. Facsko, S.; Kurz, H.; Dekorsy, T. Energy dependence of quantum dot formation by ion sputtering. *Phys. Rev. B* **2001**, *63*, 165329.
6. Cuerno, R.; Makse, H.A.; Tomassone, S.; Harrington, S.T.; Stanley, H.E. Stochastic model for surface erosion via ion sputtering: Dynamical evolution from ripple morphology to rough morphology. *Phys. Rev. Lett.* **1995**, *75*, 4464.
7. Frost, F.; Schindler, A.; Bigl, F. Roughness evolution of ion sputtered rotating InP surfaces: Pattern formation and scaling laws. *Phys. Rev. Lett.* **2000**, *85*, 4116.
8. Keller, A.; Facsko, S. Ion-induced nanoscale ripple patterns on Si surfaces: Theory and experiment. *Materials* **2010**, *3*, 4811–4841.

9. Facsko, S.; Bobek, T.; Stahl, A.; Kurz, H.; Dekorsy, T. Dissipative continuum model for self-organized pattern formation during ion-beam erosion. *Phys. Rev. B* **2004**, *69*, 153412.
10. Goyal, M.; Aggarwal, S.; Sharma, A.; Ojha, S. Surface structuring in polypropylene using Ar + beam sputtering: Pattern transition from ripples to dot nano-structures. *Appl. Surf. Sci.* **2018**, *439*, 380–385.
11. Lee, S.; Byun, E.Y.; Kim, J.K.; Kim, D.G. Ar and O₂ linear ion beam PET treatments using an anode layer ion source. *Curr. Appl. Phys.* **2014**, *14*, S180–S182.
12. Jung, S.; Byeon, E.-Y.; Kim, D.-G.; Lee, D.-G.; Ryoo, S.; Lee, S.; Shin, C.-W.; Jang, H.W.; Yang, J.-Y.; Kim, H.J. Copper-Coated Polypropylene Filter Face Mask with SARS-CoV-2 Antiviral Ability. *Polymers* **2021**, *13*, 1367.
13. Böhm, C.; Perrin, J. Retarding-field analyzer for measurements of ion energy distributions and secondary electron emission coefficients in low-pressure radio frequency discharges. *Rev. Sci. Instrum.* **1993**, *64*, 31–44.
14. Junkar, I.; Cvelbar, U.; Vesel, A.; Hauptman, N.; Mozetič, M. The role of crystallinity on polymer interaction with oxygen plasma. *Plasma Process. Polym.* **2009**, *6*, 667–675.
15. Coen, M.C.; Lehmann, R.; Groening, P.; Schlapbach, L. Modification of the micro-and nanotopography of several polymers by plasma treatments. *Appl. Surf. Sci.* **2003**, *207*, 276–286.
16. Vollmer, C.; Kepaptsoglou, D.; Leitner, J.; Busemann, H.; Spring, N.H.; Ramasse, Q.M.; Hoppe, P.; Nittler, L.R. Fluid-induced organic

synthesis in the solar nebula recorded in extraterrestrial dust from meteorites. *Proc. Natl. Acad. Sci. USA* **2014**, *111*, 15338–15343.

17. Ziegler, J.F.; Ziegler, M.D.; Biersack, J.P. SRIM–The stopping and range of ions in matter (2010). *Nucl. Instrum. Methods Phys. Res. Sect. B* **2010**, *268*, 1818–1823
18. Lee, S.; Byeon, E.; Jung, S.; Kim, D.-G. Heterogeneity of hard skin layer in wrinkled PDMS surface fabricated by Ar ion-beam irradiation. *Sci. Rep.* **2018**, *8*.
19. Jeon, T.Y.; Park, S.; Kim, D.; Kim, S. Standing-Wave-Assisted Creation of Nanopillar Arrays with Vertically Integrated Nanogaps for SERS-Active Substrates. *Adv. Funct. Mater.* **2015**, *25*, 4681–4688.
20. Wang, X.; Park, S.; Ko, J.; Xiao, X.; Giannini, V.; Maier, S.A.; Kim, D.; Choo, J. Sensitive and Reproducible Immunoassay of Multiple Mycotoxins Using Surface-Enhanced Raman Scattering Mapping on 3D Plasmonic Nanopillar Arrays. *Small* **2018**, *14*, 1801623.

Chapter 3. Fabrication of a Nano-wrinkled PDMS

Substrate

3.1 Introduction

Nanostructures on polymer films with sizes varying between tens and hundreds of nanometers are widely used in anti-fouling, superhydrophobic, anti-reflection, and surface-enhanced Raman spectroscopy applications [1–6]. They are also utilized in the security and biotechnology fields [7–9]. Nanopatterning processes using physical masks or molds can create nanostructured polymer films with regular patterns; however, their fast low-cost production remains a challenging task. The demand for the mass production of nanostructured polymer films without physical masks or molding processes has recently increased [10–16]. To facilitate industrial applications requiring irregularly nanopatterned surfaces, processes using plasma and ion-beam treatments, electrospinning, and electrochemical methods with high commercialization potential are employed to form nanostructured polymer films [17].

The treatment of polymer surfaces by energetic ions can generate nanostructures directly on polymer films. The ion irradiation of polymer films at several kilo-electron volts induces the surface-localized polymer deformation by transferring the ion energy in a region with a size between tens and hundreds of nanometers [18, 19]. This energy causes localized bond dissociation and ionization beneath the surface and initiates the scission and cross-linking processes, which induce self-organized nanostructuring (SONS). To implement SONS with controlled scission and cross-linking processes, it is necessary to change the amount of ion energy transferred to the polymer surface, depth of energy absorption, and added elements that affect surface chemical bonds. Ion-beam irradiation is suitable for SONS because it allows easily varying the incident energy, penetration depth, and

composition of reactive ion species, such as oxygen, nitrogen, and hydrogen, for chemical bond modification.

Wrinkles are among the most well-known self-organized nanostructures fabricated by ion-beam irradiation. In particular, wrinkles on PDMS substrates are used in wearable devices due to their excellent flexibility and bio-adaptability [20–23]. Liquid metal ions or gas ion-beams can successfully fabricate wrinkles on PDMS substrates [24–26]. An X-ray photoelectron spectroscopy (XPS) analysis of wrinkled PDMS surfaces has shown that the original surfaces were converted to silica-like hardskin layers. The difference in elastic modulus between the hardskin layer and PDMS medium induces wrinkling [25, 26]. Previous studies have qualitatively attributed the observed changes in the wrinkle structures on the PDMS surface to ion-beam irradiation conditions, such as the ion energy and beam incident angle. Although analyses of hardskin layers have shown the existence of a strong correlation between the wrinkle width and irradiation conditions, a detailed mechanism of their formation including the physical parameters of ion–polymer interactions has not been determined. Various aspects such as the formation of a hardskin layer by the collisional energy transfer after ion impingement, spatial distribution of surface bond states caused by the variation in the ion energy transfer rate with depth, and distribution of SiO_x ($x = 0.5\text{--}2$) bonds in the silica-like hardskin layer have not been discussed.

In this study, wrinkles were fabricated on a PDMS surface by the argon ion-beam irradiation at an energy of 360–840 eV. XPS depth profiling was performed to measure the spatial bond distribution in the depth direction of the wrinkled PDMS. The ion energy transferred to the PDMS substrate was calculated theoretically to establish the correlation between the incident ion energy and modification depths, at

which scission and cross-linking occurred. This approach was utilized to describe quantitatively the formation of a heterogeneous hardskin on the PDMS surface after argon ion-beam irradiation.

3.2 Methods

PDMS precursor mixtures were prepared by mixing Sylgard 184 base and a hardener (Sylgard 184, Dow Corning Corporation, USA) at a mass ratio of 10:1 in a Petri dish for 10 min. The prepared mixtures were held in a vacuum chamber until no bubbles remained in their bulk. Polyimide substrates with thicknesses of 120 μm were sequentially washed with acetone and isopropanol and dried at 80 $^{\circ}\text{C}$ in an oven for 10 mins. The precursor mixtures were spin-coated onto the polyimide substrates with sizes of 100 \times 100 mm and thicknesses of 125 μm for 40 s at 500 rpm. The produced PDMS coatings were cured at 65 $^{\circ}\text{C}$ on a hot plate for 120 min. The obtained PDMS samples on the polyimide substrates were exposed to an argon ion-beam generated by a closed-drift ion source [27]. This ion source emitted a linear argon ion-beam with a width of 300 mm and ion fluence of $5.0\pm 0.5\times 10^{15}/\text{cm}^2$. The anode voltage was varied to achieve an average ion energy of 360, 600, or 840 eV. A retarding potential analyzer measured the average ion energy of the argon ions incident on the PDMS samples [33]. The argon ion-beam irradiation procedure was conducted in a vacuum environment with a background pressure of 0.1 Pa. The wrinkle surface patterns were observed by FE-SEM (JSM-6700F, JEOL) and AFM (NX10, Park Systems). The haze and transmittance of the PDMS samples were measured by a haze and transmittance measurement system (COH-400, Nippon Denshoku). PDMS surface binding states were analyzed by XPS (K-ALPHA+ XPS system, Thermo Fisher Scientific). The X-ray source, energy, and spot size were monochromated Al $K\alpha$, 72 W, and 400 μm , respectively. The obtained peaks were corrected with respect to a C 1s reference peak position (284.6 eV). To minimize changes in the ion beam-treated surface during XPS depth profiling, an argon cluster

gun (energy: 4 kV, cluster number: 1000) was used to etch the PDMS substrate. XPS depth profiling was conducted over a period of 100 s at 5-s intervals for the topmost layer and over a period of 750 s at 30-s intervals for the intermediate layer. In SRIM simulations, the "Detailed Calculation with Full Damage Cascades" conditions were used. This option follows every recoil particle until its energy becomes less than the lowest energy level of any target atom. To minimize the statistical error of SRIM computations, the number of collision events exceeded 10000 for each simulation case. Details of the SRIM calculation procedure are described in the software manual [32].

3.3. Results and Discussion

In this section, PDMS samples were prepared by argon ion irradiation at ion energies of 360, 600, and 840 eV. Figure 3.1 displays the SEM and AFM images of the argon ion-beam irradiated PDMS surfaces. The show that as the argon ion energy increases, the wrinkle width increases from 410.2 ± 25.1 to 941.1 ± 49.3 nm, and the wrinkle height varies from 47.3 ± 7.1 to 100.1 ± 13.8 nm. This observation is in good agreement with the results of other studies on ion-beam irradiated PDMS [25, 26]. The transmittance and haze of the as-received PDMS sample were 94.52% and 0.28%, respectively. After the argon ion-beam treatment, the transmittance decreased by 0.22%, and the haze increased by 2.18%. The physical and optical properties of the studied PDMS samples are listed in Table 3.1. Note that the PDMS wrinkles produced in this work were fabricated by an in-line ion-beam irradiation process using a linear ion beam, which resulted in irradiated areas with widths as high as 300 mm [27].

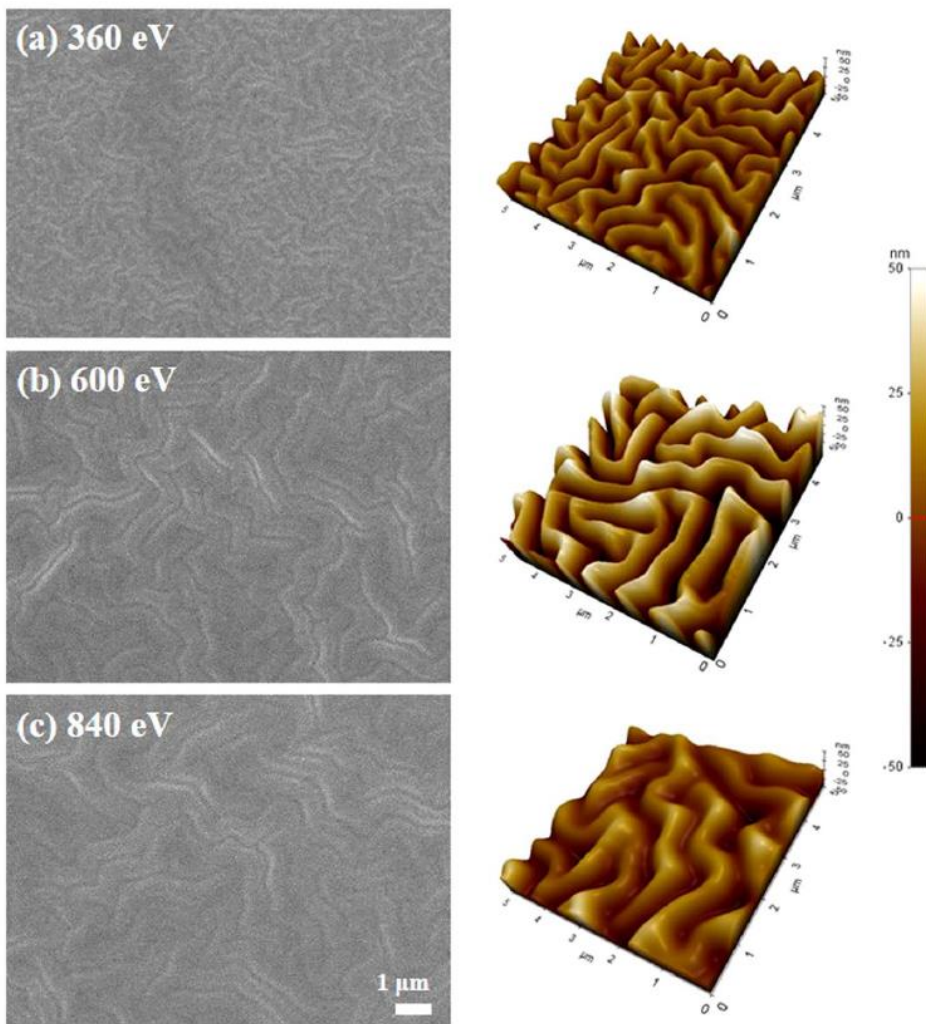


Figure 3.1. Wrinkled PDMS surfaces obtained after Ar ion-beam irradiations at ion energies of (a) 360 eV, (b) 600 eV, and (c) 840 eV.

Table 3.1. Physical and optical properties of the PDMS samples after different Ar ions irradiations.

	bare	360 eV	600 eV	840 eV
Wavelength (nm)	-	410.2 ± 25.1	512.7 ± 27.2	941.1 ± 49.3
Amplitude (nm)	-	47.3 ± 7.1	60.1 ± 10.2	100.1 ± 13.8
Haziness (%)	0.28	0.36	1.00	2.46
Perpendicular transmittance (%)	93.52	93.63	92.58	92.30
Diffused transmittance (%)	0.26	0.34	0.93	2.27
Total transmittance (%)	93.26	93.29	91.65	90.03

XPS depth profiling was performed to analyze the topmost PDMS surface layer irradiated by argon ions. XPS Si $2p$ and C $1s$ spectra were recorded at etching times of 0–100 s and intervals of 10 s. Figures 3.2(a–c) show the Si $2p$ peaks obtained at argon ion energies of 360, 600, and 840 eV, respectively. The peak positions of SiO₁ (102.1 eV), SiO_{1.5} (102.8 eV), and SiO₂ (103.4 eV) bonds are designated in the graph [28]. The observed peak shifts to higher binding energies indicate that the amount of oxygen in SiO_x bonds increases with increasing etching time from 0 to 100 s. At 100 s, bonds similar to SiO_x ($x = 1.75–2$) are detected at all energies. The corresponding silica-like layer is a hardskin layer that induces wrinkling [25]. However, for the topmost surface layer and etching times of 0–20 s, the Si $2p$ peak is shifted to low binding energies, indicating smaller oxygen amounts in the SiO_x structure. As the argon ion energy increases to 840 eV, further oxygen reduction occurs in SiO_x ($x = 1.5 \rightarrow 1.25$) species, as shown in Figure 3.2c. Figure 3.3 illustrates the deconvolution of the Si $2p$ peaks recorded at an etching time of 0 s.

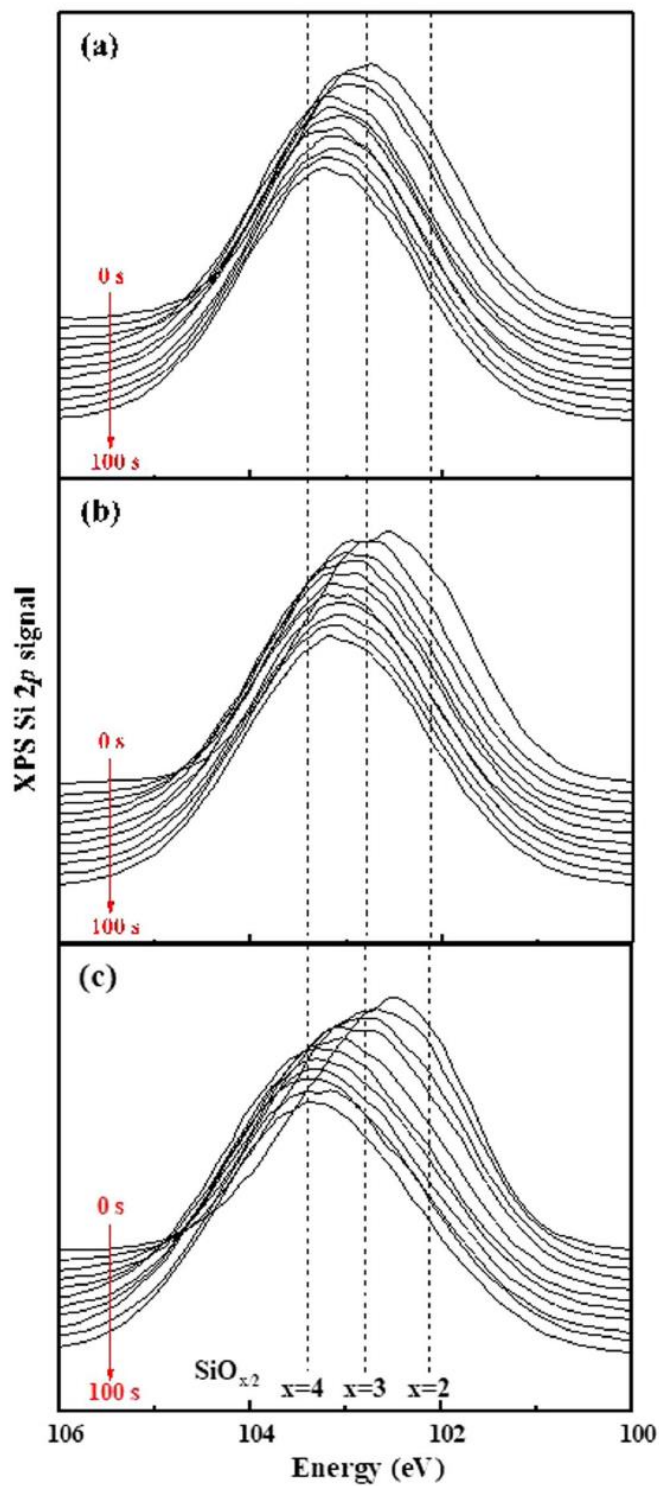


Figure 3.2. XPS depth profiling of the Si $2p$ signal. The etching process was conducted for 100 s at intervals of 10 s and Ar ion energies of (a) 360 eV, (b) 600 eV, and (c) 840 eV.

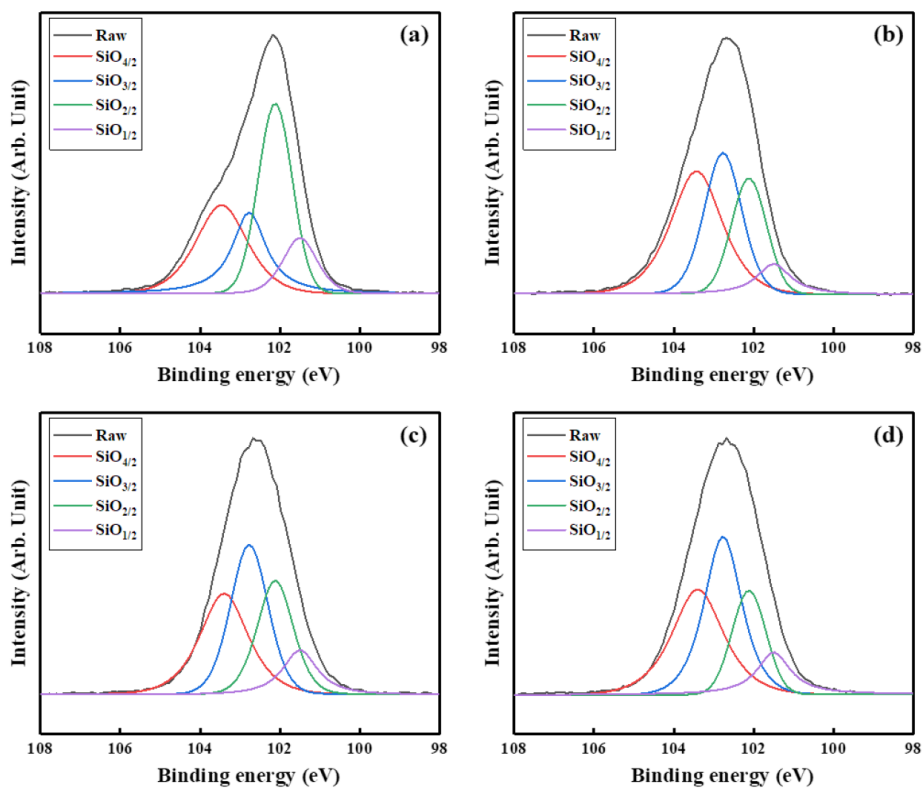


Figure 3.3. Deconvolution of the Si 2p XPS peaks obtained for the topmost surface layers of (a) pristine PDMS and the PDMS substrates irradiated at Ar ion energies of (b) 360 eV, (c) 600 eV, and (d) 840 eV.

An XPS analysis of the obtained C 1s spectra produced more complex but comprehensible results. Figure 3.4 shows the C 1s XPS profiles obtained at etching times of 0–100 s, intervals of 10 s, and argon ion energies of 360, 600, and 840 eV. The XPS C 1s peak includes several bonds, such as C–C (sp_2) and C–H overlapped at 284.6 eV, C–C (sp_3) at 285.3 eV, C–Si at 283.8 eV, C–O at 286.3 eV, and C=O at 287.6 eV [29]. The as-received PDMS sample exhibits a C 1s spectrum including mainly C–H bonds (Supplement 3). Ion-beam irradiation causes polymer cross-linking, inducing the appearance of the C–C (sp_2), C–C (sp_3), C–O, and C=O peaks [29]. The observed increase in the C 1s signal intensity at 284.6 eV after irradiation may result from the formation of C–C (sp_2) bonds via cross-linking. This occurs because ion bombardment dissociates C–H ($E_d = 4.5$ eV), H–CH ($E_d = 4.69$ eV), and H–CH₂ ($E_d = 4.9$ eV) bonds at higher rates compared with those of the C=O ($E_d = 7.8$ eV) and C–O ($E_d = 11.2$ eV) bond dissociation, which require dissociation energies (E_d) exceeding those of hydrogen-related bonds [29].

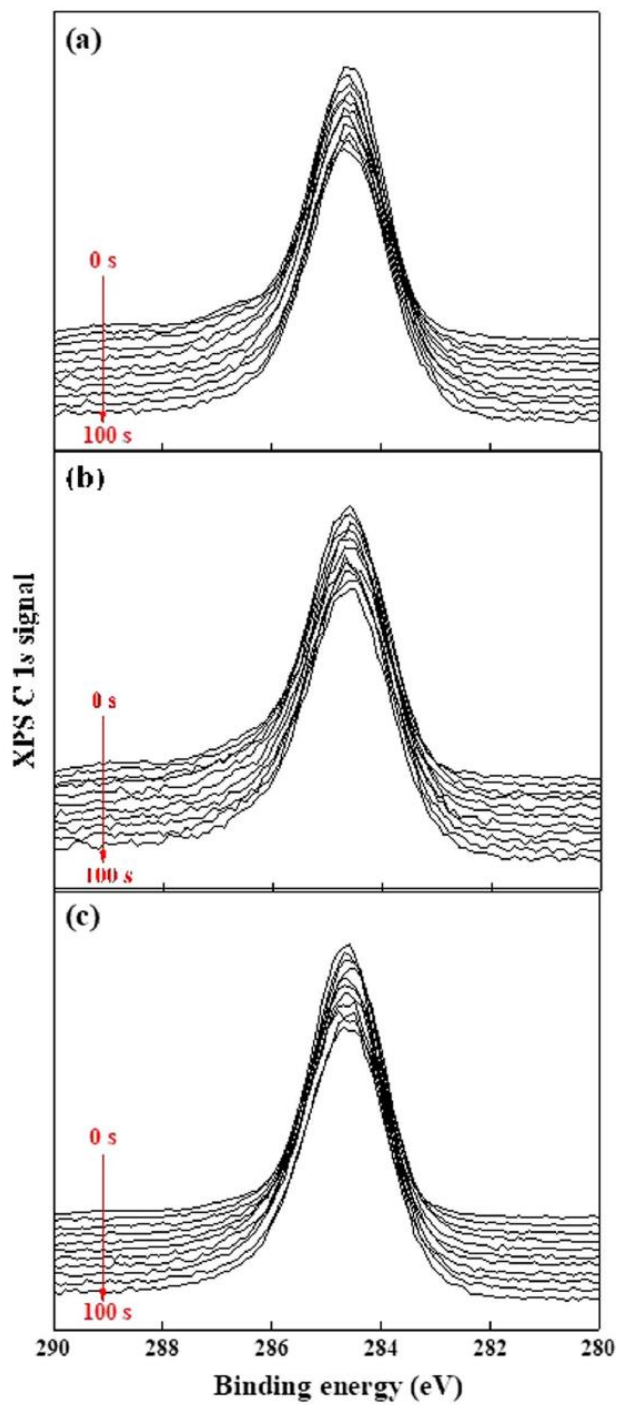


Figure 3.4. XPS depth profiling of the C 1s signal. The etching process was conducted for 100 s at intervals of 10 s and Ar ion energies of (a) 360 eV, (b) 600 eV, and (c) 840 eV.

As the etching time increased from 0 to 100 s, the observed changes in the C 1s peak were analyzed by performing its deconvolution. Figures 3.5(a–c) show the C–C (sp_2), C–H, C–C (sp_3), C–Si, C–O, and C=O bond ratios plotted as functions of the ion penetration depth. Each ratio was calculated with respect to the C 1s peak area (Figure 3.6). At an etching time of 100 s, the three samples exhibit similar bond ratios. However, different scission processes were observed after etching their surfaces for 0–50 s. The C–C (sp_3) bond, which has a higher E_d of 6.3 eV than that of C–Si ($E_d = 4.5$ eV) undergoes scission at ion energies of 600 and 840 eV, but not at 360 eV. The ratios of C=O ($E_d = 7.8$ eV) and C–O ($E_d = 11.2$ eV) bonds, which have higher E_d values than that of C–C (sp_3) are almost constant. The increased peak ratio at 284.6 eV is close to the decreased ratios of the C–Si and C–C (sp_3) bonds, which indicates that the damaged C–Si and C–C (sp_3) bonds are likely cross-linked to C–C (sp_2).

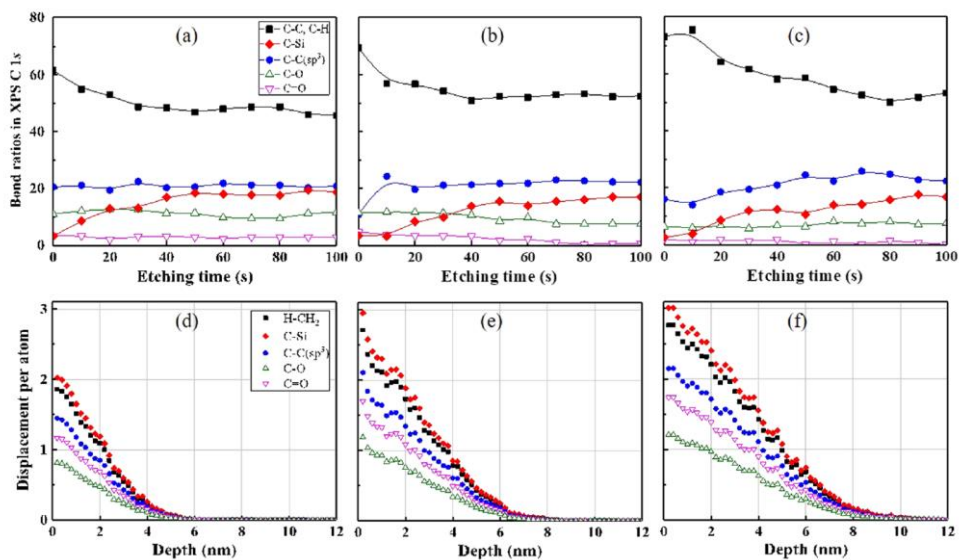


Figure 3.5. Bond ratios determined by conducting XPS C 1s depth profiling at Ar ion energies of (a) 360 eV, (b) 600 eV, and (c) 840 eV. DPA values obtained at Ar ion energies of (d) 360 eV, (e) 600 eV, and (f) 840 eV. The E_d magnitudes of H-CH₂, C-Si, C-C (sp³), C=O, and C-O were equal to 4.9, 4.5, 6.3, 7.8, and 11.2 eV, respectively.

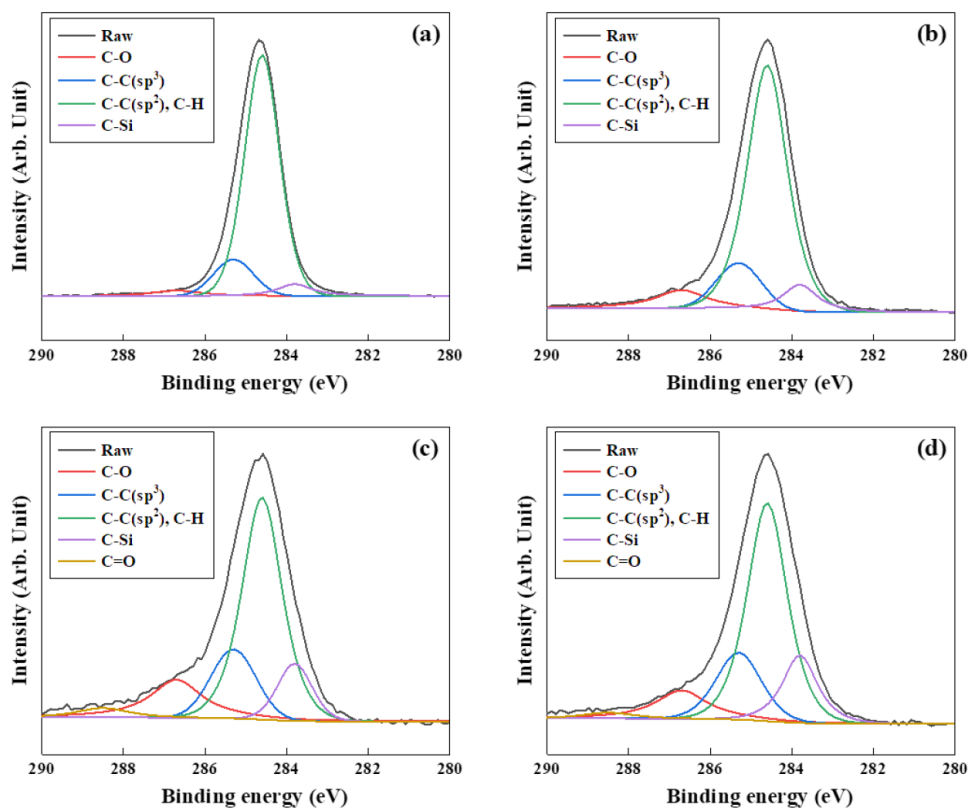


Figure 3.6. Deconvolution of the C 1s XPS peaks obtained for the topmost surface layers of (a) pristine PDMS and the PDMS substrates irradiated by Ar ions with energies of (b) 360 eV, (c) 600 eV, and (d) 840 eV.

At etching times of 150–750 s, no significant changes in the Si 2*p* and C 1*s* XPS signal intensities were observed, although the XPS depth profile indicates that the argon ion beam significantly changed the PDMS surfaces as compared with that of bulk PDMS (Figure 3.7). The Si 2*p* spectrum suggests that the cross-linking reaction formed SiO_x ($x = 1.75\text{--}2$) species at argon ion energies of 360, 600, and 840 eV. The C 1*s* depth profile also shows the broadening of the similar peak at 284.7 eV, indicating the formation of C=O, C–O, and C–C (*sp*₃) bonds due to cross-linking.

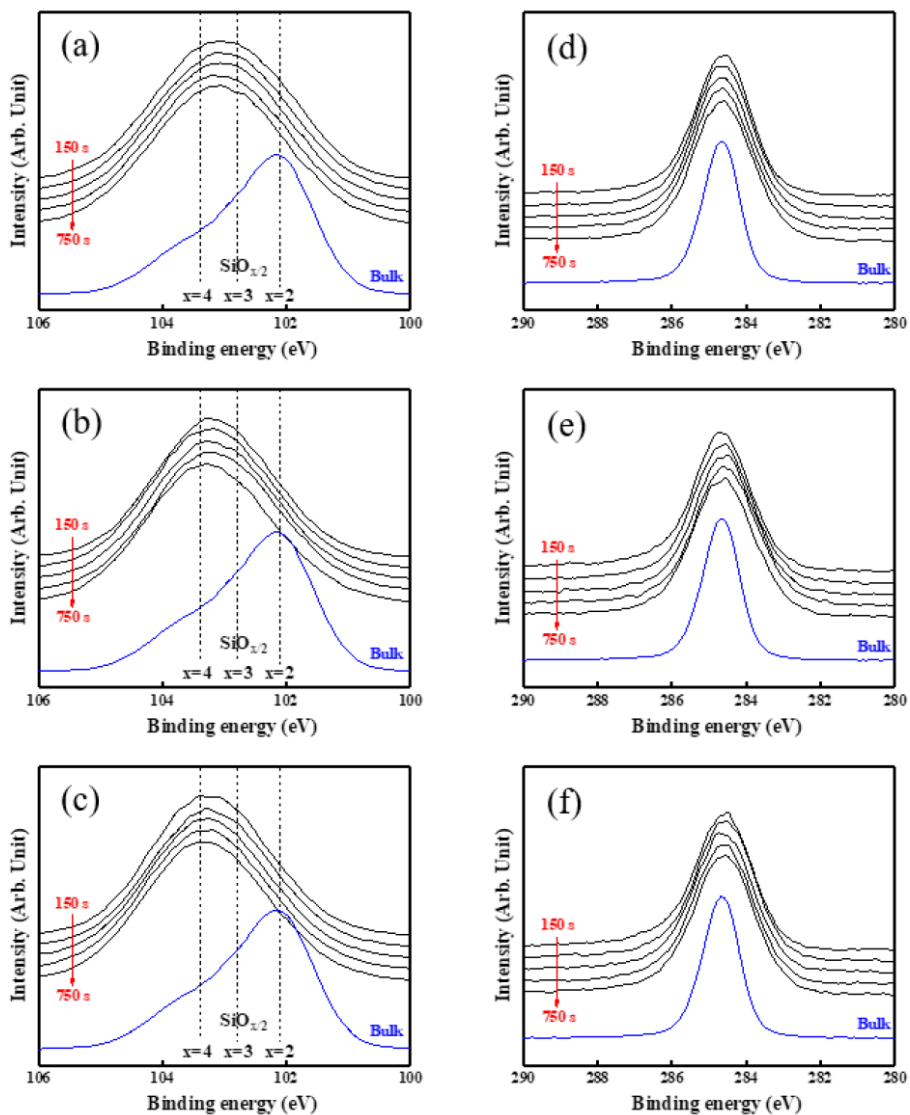


Figure 3.7. Bonding states of the Si 2*p* and C 1*s* signals obtained at etching times of 150–750 s and Ar ion energies of 300, 600, and 840 eV. (a) Si 2*p* at 360 eV, (b) Si 2*p* at 600 eV, (c) Si 2*p* at 840 eV, (d) C 1*s* at 360 eV, (e) C 1*s* at 600 eV, and (f) C 1*s* at 840 eV. The Si 2*p* and C 1*s* peaks of the as-received PDMS sample are also plotted as the bulk spectra.

The heterogeneity of the ion-beam irradiated PDMS surface observed by XPS depth profiling at etching times of 0–100 s and 150–750 s can be explained using an ion–polymer interaction model that takes into account the collision process. Ions transfer their impinging energy to the polymer medium and generate recoils, energetic particles that gain energy from ionic collisions. In the target medium, the penetrating particles (both ions and recoils) lose energy via nuclear or electronic stopping. When a particle penetrates the polymer, it loses energy by colliding with target nuclei via an interaction called nuclear stopping, which causes an atomic displacement that initiates bond breakage and phonon generation [30]. Nuclear stopping induces an atomic displacement when the energy transferred to the recoil is higher than the dissociation energy or displacement threshold. Sputtering occurs if the recoil moves toward the surface and its energy exceeds the surface binding energy. Recoils generate phonons for the ions with transferred energy below the displacement energy, which releases energy over short lengths below 10 nm. Commonly used polymers are amorphous; therefore, phonons cannot efficiently transfer heat by lattice vibrations. Polymer vibrations transfer heat to the bulk medium at a low thermal conductivity of 0.1–0.2 W/m·K [31]. This localized heating process can induce cross-linking without increasing the bulk temperature [25]. The interaction of the impinging particle with electrons in the target material can induce electronic stopping, which is inelastic and transfers energy by both electronic excitation and ionization. All the excited electrons (plasmons) eventually lose energy due to thermalization [30]. Electronic stopping effectively induces cross-linking by collectively excited electrons, which produce a sizeable excitation volume and compulsive interactions between ions and radical pairs [30]. Thus, the stopping power and depth, at which the target material absorbs energy, are critical parameters

that influence the scission and cross-linking reactions occurring on polymer surfaces after ion-beam irradiation.

The energy loss per unit depth dE/dx provides a quantitative description of the scission and cross-linking processes in the polymer medium. dE/dx is a sum of $(dE/dx)_{nuclear}$ for nuclear stopping and $(dE/dx)_{electron}$ for electronic stopping. It reaches a maximum in the topmost layer and gradually decreases with increasing penetration depth. While few ions directly lose energy by ionization and atomic displacement in the topmost layer, ions transfer most of their energy to recoils. Recoils with energies greater than the ionization and dissociation energies are concentrated near the topmost layer. Under the topmost layer, electronic stopping causes ionization, while nuclear stopping mostly induces phonon vibrations, which promote cross-linking in the intermediate layer. Beneath the intermediate layer lies an inherent bulk layer. Therefore, a pairwise comparison of dE/dx and the displacement energies of polymer chains can be used to quantitatively predict the depth-dependent spatial distribution of bond scission. To investigate the heterogeneous hardskin layer, dE/dx values must be determined at various ion irradiation conditions, such as ion energy, ion composition, and incident angle. SRIM is a computational program used to calculate the energy transmitted by ions to a medium through collision [32]. In this study, dE/dx was calculated according to the ion-beam irradiation conditions using SRIM. Scission mostly occurs in the topmost layer, where the ion energy transferred to recoil particles is sufficient to induce atomic displacements. When evaluating scission due to atomic displacements, the DPA unit defined in Equation (3.1) is often used [30].

$$DPA = \frac{0.8}{2E_d} \left(\frac{dE}{dx} \right)_{nuclear} \times \frac{ion\ fluence}{target\ atomic\ density} \dots (3.1)$$

DPA is a parameter quantitatively describing the spatial scission distribution in the depth direction as a function of $(dE/dx)_{nuclear}$, dissociation energy (E_d), and the polymer material type. Figures 3.6(d–f) show the DPA values calculated for carbon bonds at an ion fluence of $5 \times 10^{15}/\text{cm}^2$, PDMS total atomic density of 0.97 g/cm^3 , and different E_d magnitudes. The low E_d bonds, such as H–CH₂ and C–Si, exhibit large DPA values of 1.9–3.0 in the topmost layer at a depth almost equal to zero. The DPA of C–C (sp³) is 1.5–2.1, and those of C=O and C–O are lower than 1.8 in the topmost layer. The DPA and XPS depth profiling data indicate that the scissions of C–Si and C–C (sp³) bonds occur simultaneously with a cross-linking of C–C (sp²) and C–H at DPA values higher than 1.9. As the depth, at which DPA is higher than 1.5, increases, the etching times, at which the bond ratios of C–Si and C–C (sp³) are reduced, also increase. The DPA values determined for Si–O bonds were consistent with the DPAs of carbon bonds. The DPAs of the atoms in Si–O bonds were calculated at an E_d of 8.3 eV. Figure 3.8 shows that the DPA of the oxygen atom in the Si–O bond on the surface increases from 0.8 to 1.2 as the argon ion energy increases from 360 to 840 eV. This means that increasing the argon ion energy promotes O displacement and, therefore, Si–O bond scission in the topmost surface layer. The Si 2*p* peak shift to lower binding energies observed for the topmost surface in Figure 3.8 is consistent with the DPA increase for the Si–O bond at higher argon ion energies.

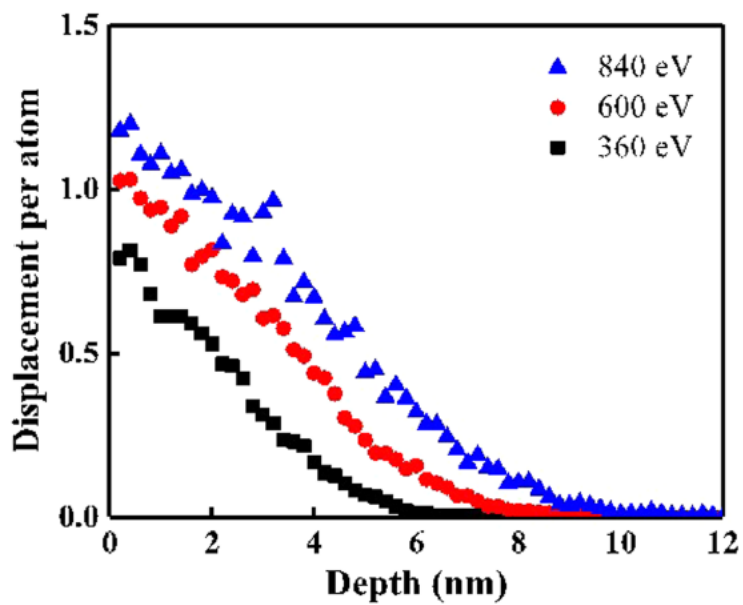


Figure 3.8. DPA values plotted at various ion penetration depths and Si–O dissociation energy of 8.3 eV.

To determine the thickness and Young's modulus of the hardskin layer formed on the PDMS surface, the wavelength and amplitude of PDMS listed in Table 3.1 and Equations (1.8)–(1.11) were used. The Young's modulus of PDMS was 860 kPa; the Poisson ratio was 0.5; and the Poisson ratio of the hardskin layer was assumed to be 0.2 [26]. Because the number of variables exceeds the number of formulas, it is possible to estimate only ranges of these two parameters, not their specific values. The Young's modulus of SiO₂ is 72 GPa, and the thicknesses of the hardskin layer calculated at argon ion energies of 360, 600, and 840 eV were equal to 2.3, 2.7, and 5.4 nm, respectively. However, the hardskin layer consists of not only SiO₂ species, but also polymeric carbon bonds (Figures 3.5 and 3.6). Therefore, it may be predicted that Young's modulus value of the actual hardskin layer is less than 72 GPa. SRIM calculations were also performed to estimate the thickness of a more substantial surface change layer. Fig. 3.2 shows that the hardskin layer contains molecular bonds similar to those in the SiO₂ structure, suggesting that PDMS molecular bonds were cleaved and then cross-linked. The scission and cross-linking of molecular bonds occur via nuclear stopping when ions penetrate a medium. SRIM allows calculating the depth at which ions penetrate PDMS, from the ion energy, and its magnitude can be potentially changed.

For SRIM calculations, the energy of the Ar ion beam varied between 360, 600, and 840 eV. The density of PDMS was 0.96 g/cm³, and its longitudinal thickness was 20 nm. The penetration depths calculated at the specified ion energies were 7.6, 9.2, and 13.3 nm, respectively. The corresponding Young's moduli of the hardskin layer were 2.09, 2.30, and 4.68 GPa, respectively. Although the SRIM-calculated values were not very accurate due to the insufficient consideration of the organic binding energy, they were physically reasonable. In future studies, more accurate values can

be computed. Figure 3.9 displays the fitting curves obtained for the thickness and Young's modulus of the hardskin layer using Equations (1.8)–(1.11), and their calculated values are listed in Table 3.2.

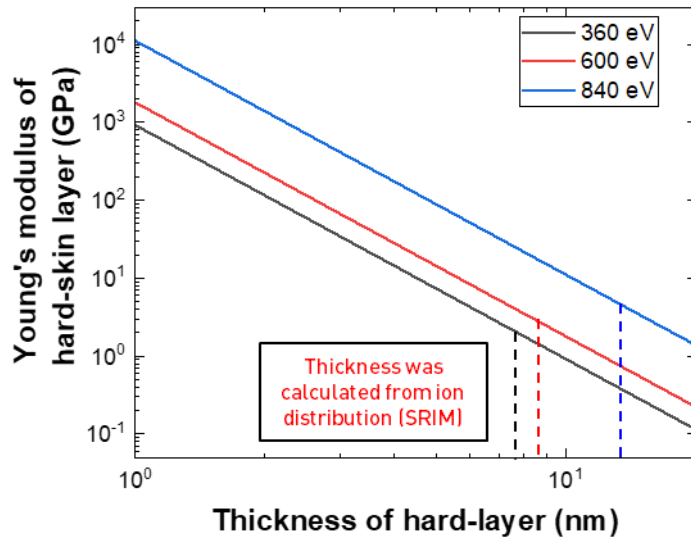


Figure 3.9. Young's modulus values calculated at various thicknesses of the hardskin layer.

Table 3.2. Thicknesses of the hardskin layer (t_{hardskin}), Young's moduli of the hardskin layer (E_{hardskin}), and induced strain values obtained during substrate irradiation with an ion beam at various energies.

	360 eV		600 eV		840 eV	
	SRIM	SiO ₂	SRIM	SiO ₂	SRIM	SiO ₂
t_{hardskin} (nm)	7.6	2.3	9.2	2.9	13.3	5.4
E_{hardskin} (GPa)	2.09	72	2.30	72	4.68	72
Strain, ϵ_0 (%)	13.5	13.1	13.9	13.6	14.5	11.2

3.4 Conclusions

The hardskin layer formed on the PDMS surface treated by argon ion-beam irradiation has a heterogeneous structure. The energetic stoppings of irradiated ions simultaneously induce the scission and cross-linking processes in the topmost layer. Under the topmost layer, the gradual decrease in the stopping power results in the predominance of cross-linking reactions in the intermediate layer. The collisional energy transfer rate calculated by SRIM and DPA concept allow a quantitative description of the scission processes occurring in the topmost layer at different argon ion beam energies. The DPA and XPS depth profiling data produced consistent spatial distributions of the silicon and carbon bonds in the depth direction. Thus, DPA can be used as a physical parameter to explain the scission and cross-linking phenomena initiating SONS on polymer surfaces after ion-beam irradiation.

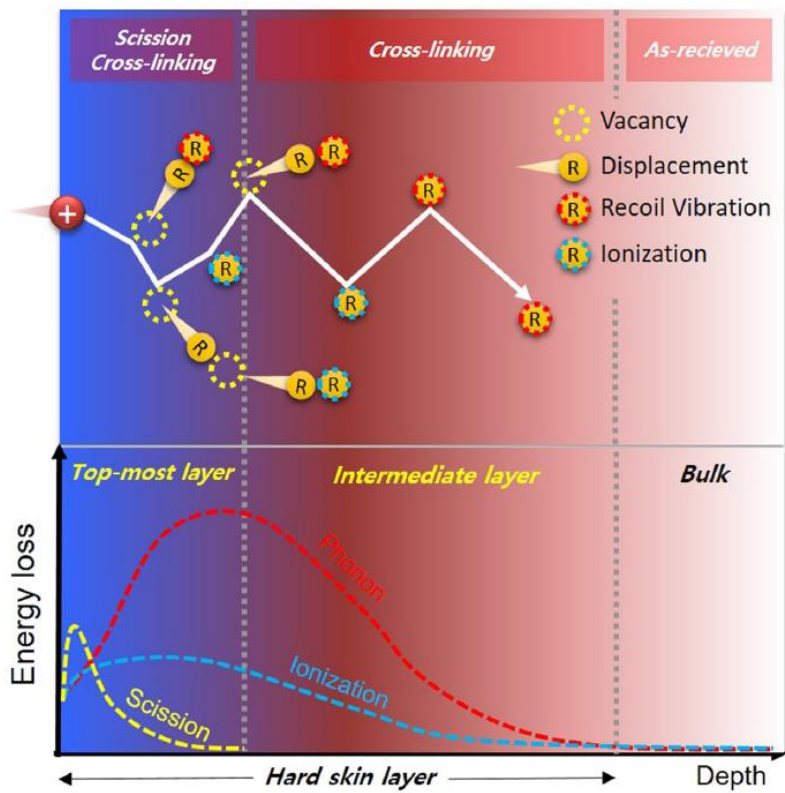


Figure 3.10. Schematic diagram illustrating the generation of the heterogeneous hardskin layer consisting of the topmost and intermediate layers.

3.5 Bibliography

1. Banerjee, I., Pangule, R. C. & Kane, R. S. Antifouling coatings: recent developments in the design of surfaces that prevent fouling by proteins, bacteria, and marine organisms. *Adv. Mater.* 23, 690–718 (2011).
2. Rahimpour, A., Jahanshahi, M., Rajaeian, B. & Rahimnejad, M. TiO₂ entrapped nano-composite PVDF/SPES membranes: preparation, characterization, antifouling and antibacterial properties. *Desalination* 278, 343–353 (2011).
3. Zhang, X., Shi, F., Niu, J., Jiang, Y. & Wang, Z. Superhydrophobic surfaces: from structural control to functional application. *J. Mater. Chem.* 18, 621–633 (2008).
4. Jung, Y. C. & Bhushan, B. Contact angle, adhesion and friction properties of micro-and nanopatterned polymers for superhydrophobicity. *Nanotechnology* 17, 4970–4980 (2006).
5. Han, K.-S., Shin, J.-H., Yoon, W.-Y. & Lee, H. Enhanced performance of solar cells with anti-reflection layer fabricated by nano-imprint lithography. *Sol. Energy Mater. Sol. Cells* 95, 288–291 (2011).
6. Jeon, T. Y., Park, S., Kim, D. & Kim, S. Standing-wave-assisted creation of nanopillar arrays with vertically integrated nanogaps for SERS-active substrates. *Adv. Funct. Mater.* 25, 4681–4688 (2015).
7. Bae, H. J. et al. Biomimetic microfingertprints for anti-counterfeiting strategies. *Adv. Mater.* 27, 2083–2089 (2015).

8. Xia, L., Wei, Z. & Wan, M. Conducting polymer nano-structures and their application in biosensors. *J. Colloid Interface Sci.* 341, 1–11 (2010).
9. Michel, R. et al. Selective molecular assembly patterning: a new approach to micro-and nanochemical patterning of surfaces for biological applications. *Langmuir*, 18, 3281–3287 (2002).
10. Humplik, T. et al. Nanostructured materials for water desalination. *Nanotechnology* 22, 292001, <https://doi.org/10.1088/0957-4484/22/29/292001> (2011).
11. Lin, J., Ding, B., Yang, J., Yu, J. & Sun, G. Subtle regulation of the micro- and nano-structures of electrospun polystyrene fibers and their application in oil absorption. *Nanoscale* 4, 176–182 (2012).
12. Yave, W., Car, A. & Peinemann, K.-V. Nanostructured membrane material designed for carbon dioxide separation. *J. Memb. Sci.* 350, 124–129 (2010).
13. Van Duyne, R. P., Hulteen, J. C. & Treichel, D. A. Atomic force microscopy and surface-enhanced Raman spectroscopy. I. Ag island films and Ag film over polymer nanosphere surfaces supported on glass. *J. Chem. Phys.* 99, 2101–2115 (1993).
14. Yilmaz, M. et al. Nanostructured organic semiconductor films for molecular detection with surface-enhanced Raman spectroscopy. *Nat. Mater.* 16, 918–924 (2017).
15. Zhang, C. et al. Continuous fabrication of nano-structure arrays for flexible surface enhanced Raman scattering substrate. *Sci. Rep.* 7, 39814, <https://doi.org/10.1038/srep39814> (2017).

16. Fan, M., Andrade, G. F. S. & Brolo, A. G. A review on the fabrication of substrates for surface enhanced Raman spectroscopy and their applications in analytical chemistry. *Anal. Chim. Acta* 693, 7–25 (2011).
17. Wen, G., Guo, Z. & Liu, W. Biomimetic polymeric superhydrophobic surfaces and nano-structures: from fabrication to applications. *Nanoscale* 9, 3338–3366 (2017).
18. Guenther, M. et al. Ion-beam induced chemical and structural modification in polymers. *Surf. Coatings Technol.* 158, 108–113 (2002).
19. Kondyurin, A. and Bilek, M. Ion beam treatment of polymers: application aspects from medicine to space. (Newnes, 2014).
20. Pang, C., Lee, C. & Suh, K. Recent advances in flexible sensors for wearable and implantable devices. *J. Appl. Polym. Sci.* 130, 1429–1441 (2013).
21. Gong, S. et al. A wearable and highly sensitive pressure sensor with ultrathin gold nanowires. *Nat. Commun.* 5, 3132, <https://doi.org/10.1038/ncomms4132> (2014).
22. Chen, Z. et al. Three-dimensional flexible and conductive interconnected graphene networks grown by chemical vapour deposition. *Nat. Mater.* 10, 424–428 (2011).
23. Shi, J. et al. Graphene reinforced carbon nanotube networks for wearable strain sensors. *Adv. Funct. Mater.* 26, 2078–2084 (2016).
24. Moon, M.-W. et al. Wrinkled hard skins on polymers created by focused ion beam. *Proc. Natl. Acad. Sci.* 104, 1130–1133 (2007).

25. Park, H.-G., Jeong, H.-C., Jung, Y. H. & Seo, D.-S. Control of the wrinkle structure on surface-reformed poly (dimethylsiloxane) via ion-beam bombardment. *Sci. Rep.* 5, 12356, <https://doi.org/10.1038/srep12356> (2015).
26. Jeong, H.-C. et al. Tailoring the orientation and periodicity of wrinkles using ion-beam bombardment. *Langmuir* 32, 7138–7143 (2016).
27. Lee, S., Byun, E.-Y., Kim, J.-K. & Kim, D.-G. Ar and O₂ linear ion beam PET treatments using an anode layer ion source. *Curr. Appl. Phys.* 14, S180–S182 (2014).
28. Alexander, M. R., Short, R. D., Jones, F. R., Michaeli, W. & Blomfield, C. J. A study of HMDSO/O₂ plasma deposits using a high-sensitivity and -energy resolution XPS instrument: curve fitting of the Si 2p core level. *Appl. Surf. Sci.* 137, 179–183 (1999).
29. Tajima, S. & Komvopoulos, K. Surface modification of low-density polyethylene by inductively coupled argon plasma. *J. Phys. Chem. B* 109, 17623–17629 (2005).
30. Lee, E. H. Ion-beam modification of polymeric materials—fundamental principles and applications. *Nucl. Instrum. Methods Phys. Res. Sect. B Beam Interact. Mater. Atoms* 151, 29–41 (1999).
31. Van Krevelen, D. W. & Te Nijenhuis, K. Properties of polymers: their correlation with chemical structure; their numerical estimation and prediction from additive group contributions. (Elsevier, 2009).
32. Ziegler, J. F., Ziegler, M. D. & Biersack, J. P. SRIM – the stopping and range of ions in matter (2010). *Nucl. Instrum. Methods Phys. Res. Sect. B Beam Interact. Mater. Atoms* 268, 1818–1823 (2010).

33. Böhm, C. & Perrin, J. Retarding-field analyzer for measurements of ion energy distributions and secondary electron emission coefficients in low-pressure radio frequency discharges. *Rev. Sci. Instrum.* 64, 31–44 (1993).

Chapter 4. Nano-hairy PET Structure for the Enhancement of External Light Extraction Efficiency of OLEDs

4.1 Introduction

OLEDs are widely used in displays and lighting applications due to their high efficiency and long service life as well as in manufacturing processes [1–4]. They can also be potentially applied in flexible devices, which is advantageous for the mass production of roll-to-rolls [4, 5].

The internal structure of OLEDs and their components are continuously improved to increase the OLED efficiency; however, most of these diodes are glass-based devices [1, 2, 6, 7]. To achieve a higher OLED efficiency, new materials or structures must be developed to increase the internal energy (electrical energy to optical energy) conversion efficiency or allow the light trapped inside the device to escape to the outside (it is well known that less than 30% of the light generated inside OLEDs device escapes to the outside [7–9]). The OLED efficiency can be increased by controlling the device thickness, adjusting the polarization mode by aligning the molecular orientation, reducing the plasmonic loss by utilizing a nano-wrinkled substrate, and forming a light extraction layer between the substrate and a transparent electrode [3, 6, 7].

To form a light extraction layer on the outermost side of the device, substrate roughening must be conducted through lithography or nanostructure (microlens) formation [10–12]. In this study, a nanostructure was formed on the polymer surface by ion-beam surface etching. This approach allows roll-to-roll continuous processing and self-nanostructuring without patterning or using a mask.

The PET surface was irradiated with an ion beam to form a hairy nanostructure, which changed the optical characteristics of the substrate and promoted the scattering process. The size of the produced nanostructure was 40–60 nm, and the scattering

mode was close to Mie scattering at the blue visible light wavelength (~400 nm) and Rayleigh scattering at higher wavelengths. In addition, scattering was more intense in the Mie scattering mode. The efficiency of the OLED fabricated from the nanostructured substrate was 30% higher than that of the device produced from the untreated PET substrate, while its scattering of the emitted blue light was more intense, as indicated by the peak of the obtained emission spectrum.

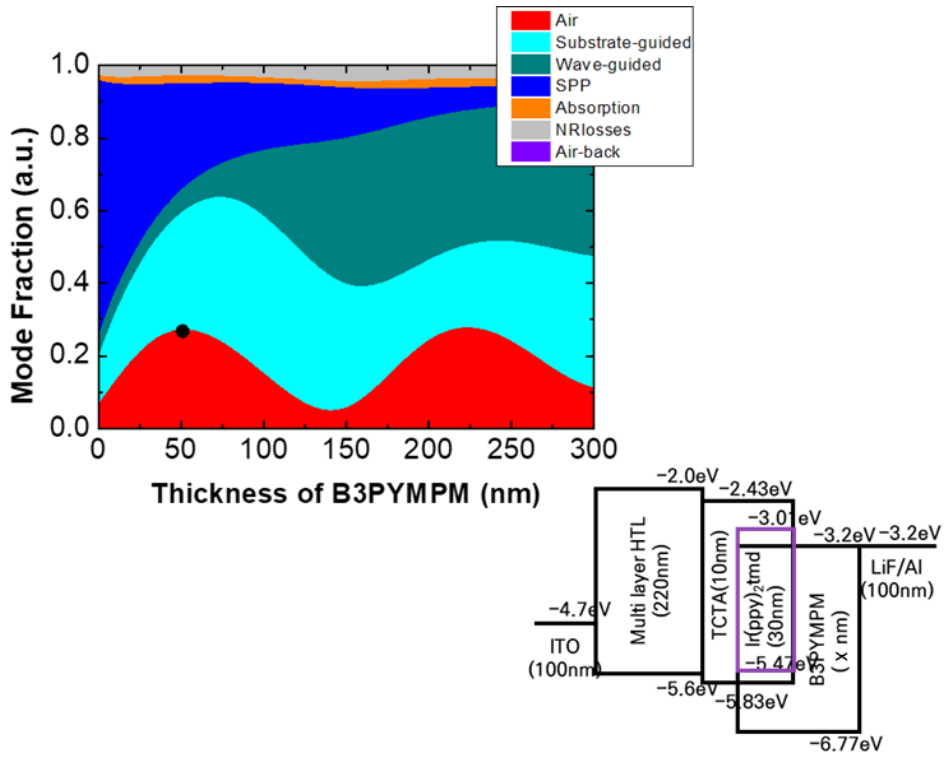


Figure 4.1. Ratio of the loss mode of the light generated in the OLED to the thickness of the electron transport layer. The light is emitted to the outside in the Air mode (red color).

4.2 Experimental

4.2.1. Materials

A nano-hairy structure was fabricated on a commercially available PET substrate by oxygen ion beam bombardment. First, a PET film with a thickness of 125 μm (PANAC, Japan) was cut into pieces with dimensions of 25 \times 25 mm^2 . After removing the protective film from the surface, the PEN film was attached to the linear moving stage of the vacuum chamber.

4.2.2. Ion Beam Treatment

The vacuum chamber was evacuated at a base pressure of 5.0×10^{-5} Torr, after which then oxygen gas was injected into the linear ion source. A gridless ion source was used to generate the linear oxygen ion beam with a width of 300 mm. The PET samples were treated at a linear moving speed of 10 mm/s. According to the results of Faraday cup measurements, the ion dose per scan was 1.2×10^{14} per square centimeter. The ion-beam treatment was performed 10, 20, 40, and 60 times. Oxygen ion beams were irradiated under the normal incidence conditions.

4.2.3. ITO Sputtering

The vacuum chamber was evacuated at a base pressure of 5.0×10^{-5} Torr, after which argon gas was injected into the chamber at a rate of 30 sccm. The working pressure was 1.0×10^{-3} Torr. A piece of tin-doped indium oxide (5 wt.% of tin) with a diameter of 100 mm was used as a sputtering target to deposit an ITO film with a

thickness of 150 nm serving as the OLED anode. The RF (13.56 MHz) power was 200 W, and the deposition time was 5 min.

4.2.4. OLED Fabrication

The OLED was manufactured by the following process. First, a PEDOT:PSS (Clevios AI4083, Heraeus, Germany) film with a thickness of 40 nm was spin-coated onto the ITO substrate. The obtained sample was transferred to a vacuum chamber with a base pressure of 1.0×10^{-6} Torr, and the organic material layer and metal electrode were deposited by thermal evaporation. A 30-nm N,N'-Di(1-naphthyl)-N,N'-diphenyl-(1,1'-biphenyl)-4,4'-diamine (NPB) and 10-nm tris(4-carbazoyl-9-ylphenyl)amine (TcTa) layers (serving as a hole transport layer), 7 wt.% tris(2-phenylpyridine)iridium(III) ($\text{Ir}(\text{ppy})_3$)-doped 4,4'-bis(n-carbazoyl)-1,1'-biphenyl (CBP) emission layer, 30-nm bathophenanthroline (BPhen) electron transport layer, 0.5-nm lithium fluoride layer, and 100-nm aluminum layer (used as the cathode) were deposited sequentially. The OLED efficiency was measured by a spectrophotometer (PR-650 SpectraScan Colorimeter, Photo Research, USA) and current-voltage source meter (Kiethley 2400, Tektronix, USA).

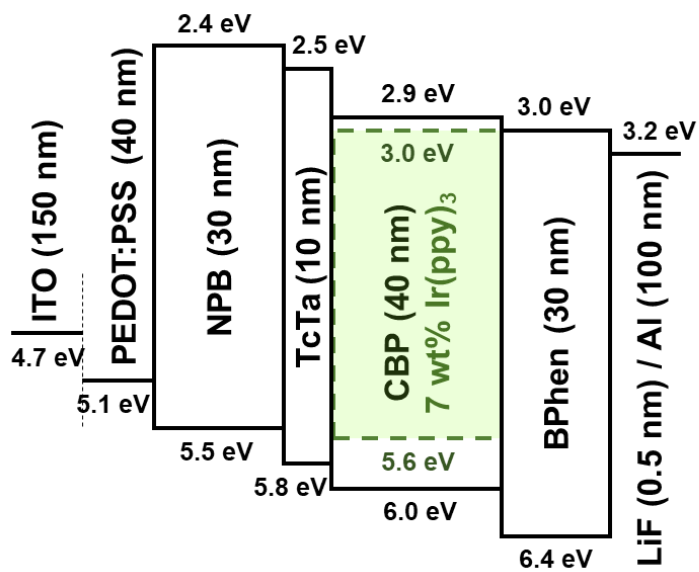


Figure 4.2. Structure of the fabricated OLED device.

4.2.5. FE–SEM

The PET surface was observed by FE–SEM (JSM 6700F, JEOL, Tokyo, Japan).

4.2.6. AFM

The morphology of the hairy nanostructures was determined by AFM (NX10, Park Systems, Suwon, Korea) in the non-contact mode.

4.2.7. Optical Properties

The optical properties of the ion-beam treated PET samples were determined by a UV–vis spectrophotometer (Cary 5000 UV–Vis–NIR Spectrophotometer, Agilent, USA).

4.3 Results and Discussion

Figure 4.3(a) shows the SEM images the bare PET surface, while Figures 4.3(b–e) display the PET surfaces treated by LIS 10, 20, 40, and 60 times, respectively. These results indicate that as the number of treatments increases, the PET nanostructure is more clearly observed. Figures 4.3(f–i) depict the AFM images of the PET surfaces treated 10, 20, and 60 times, respectively. Table 4.1 lists the peak-to-valley roughness, average roughness, and root-mean-square roughness values determined from the AFM images. Regardless of the utilized roughness calculation method, the roughness value systematically increased with the number of treatments, which is in good agreement with the obtained SEM images.

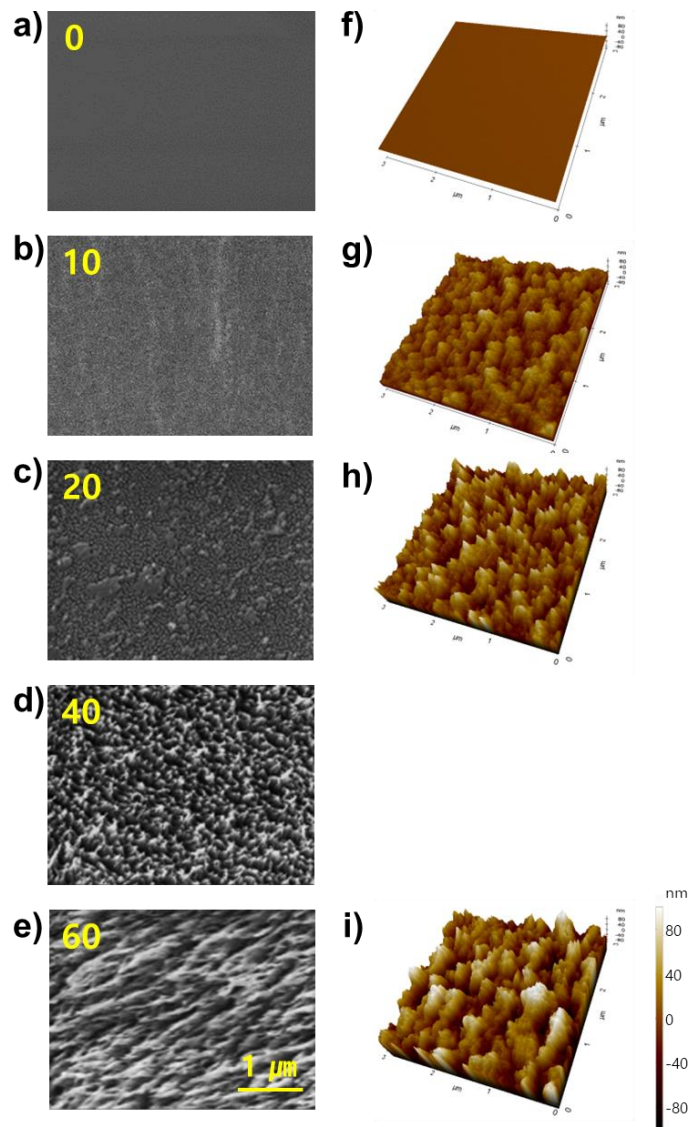


Figure 4.3. (a–e) SEM and (f–i) AFM images of the (a, f) bare PET surface and PET surfaces treated by the ion beam surface (b, g) 10 times, (c, h) 20 times, (d) 40 times, and (e, i) 60 times.

Table 4.1. Optical properties of the untreated and treated PET substrates.

	bare	10	20	40	60
Haziness (%)	0.18	1.75	4.05	13.01	23.1
Perpendicular transmittance (%)	90.96	91.25	88.54	80.01	72.23
Diffused transmittance (%)	0.16	1.60	3.59	10.41	16.68
Total transmittance (%)	91.12	92.85	92.13	90.42	88.91

Figure 4.4(a) shows the PET transmittance values obtained at different ion beam wavelengths. The measured perpendicular transmission (P.T.) and diffused transmission (D.T.) were used to calculate the total substrate transmission and haziness via the following formulas:

$$\text{Total transmittance} = P.T. + D.T. \dots \dots \dots (4.1)$$

$$\text{Haziness} = \frac{\text{diffused transmittance}}{\text{total transmittance}} \dots \dots \dots (4.2)$$

Because the wavelength of 400 nm lies in the high-absorption region of PET, its optical characteristics were determined at this wavelength or greater (we did not intend to quantitatively describe a change in transmittance due to the ion beam treatment). As the number of treatments increases, the diffused transmission gradually increases (a similar trend is observed when the beam wavelength approaches 400 nm). Figure 4.4(b) displays the average total transmission, perpendicular transmission, diffused transmission, and haziness values obtained at wavelengths of 400–800 nm (see also Table 4.2). It shows that the scattering degree continuously increases with the number of ion-beam treatments and reached a maximum of 23.1%, while the total transmittance increases from 91.12% to 92.85% and then decreases to 88.91%.

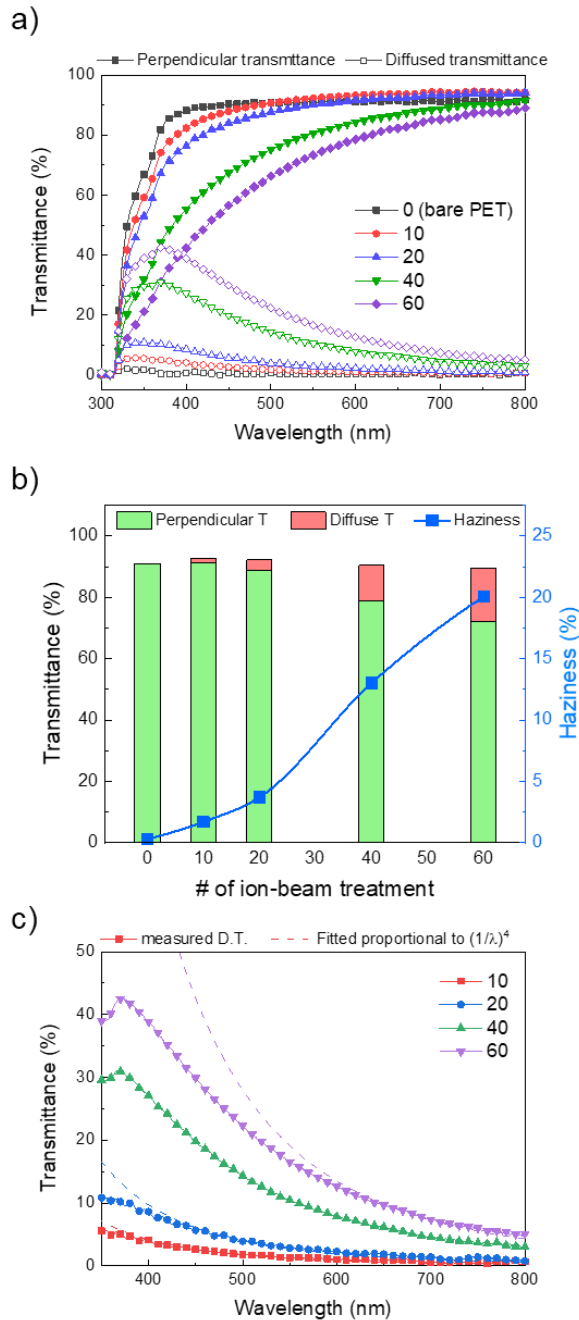


Figure 4.4. (a) Perpendicular transmittance and diffused transmittance plotted as functions of wavelength. At wavelengths below 400 nm, the absorption of the silver-colored PET material is very large. (b) Average total transmittance, perpendicular transmittance, diffused transmittance, and haziness values obtained in the wavelength region of 400–800 nm at different numbers of ion-beam treatments. (c) Diffuse transmittance values (symbols) obtained at different wavelengths and dashed fitting lines proportional to $(1/\lambda)^4$ that match the experimental data points in the region between 700 and 800 nm.

Table 4.2. Averaged total transmittance, perpendicular transmittance, diffused transmittance, and haziness values determined in the wavelength region of 400–800 nm at different numbers of ion beam treatments.

	bare	10	20	40	60
Haziness (%)	0.18	1.75	4.05	13.01	23.1
Perpendicular transmittance (%)	90.96	91.25	88.54	80.01	72.23
Diffused transmittance (%)	0.16	1.60	3.59	10.41	16.68
Total transmittance (%)	91.12	92.85	92.13	90.42	88.91

The obtained results indicate that the surface roughness exhibits a positive correlation with the scattering intensity. Among the scattering modes generated by particles, Rayleigh scattering mainly occurs when the size of particles affecting the scattering process is 1/10 or less than the wavelength, and the intensity of Rayleigh scattering is proportional to the sixth power of the particle diameter and inversely proportional to the fourth power of the wavelength [13]. The average diameters of the nanostructures obtained from the AFM images depicted of Figure. 4.3 were equal to 46.9, 52.4, and 67.8 for the samples treated 10, 20, and 60 times, respectively. Therefore, it is likely that scattering close to Rayleigh scattering occurs at higher wavelengths and gradually deviates from Rayleigh scattering at low wavelengths. The dashed lines in Figure 4.4(c) are the fitting lines corresponding to Rayleigh scattering, which match the experimental data points (symbols) in the region of 700–800 nm. Notably, the specimens treated 10 and 20 times are in good agreement with the Rayleigh scattering fitting lines in the wavelength region of 400–800 nm, while the specimen treated 60 times exhibits a different scattering mode at wavelengths less than 600 nm. It is estimated that the particle diameter is larger than 1/10 of the wavelength, and it is not a perfect spherical shape, which deviates from the Rayleigh scattering theory [14].

$$I = I_0 \frac{1 + \cos^2 \theta}{2R^2} \left(\frac{2\pi}{\lambda} \right)^4 \left(\frac{n^2 - 1}{n^2 + 2} \right)^2 \left(\frac{d}{2} \right)^6 = \alpha \frac{d^6}{\lambda^4} \dots \dots \dots (4.3)$$

The parameters of the manufactured OLED with the treated PET substrate are shown in Figure 4.5. Because only its outermost part was treated by LIS, it did not affect the electrical characteristics of the device; therefore, the amount of emitted

light increased by the surface structures.. This means that the light trapped inside the device is effectively emitted to the outside by the nano-hairy structure. The substrates without surface treatment exhibited the maximum current efficiency of 44.7 cd/A, and the substrates treated 10, 20, and 60 times demonstrated the maximum current efficiencies of 48.6, 54.7, and 58.3 cd/A, respectively. Thus, the OLED efficiency was increased by up to 30% due to the nanostructure formed on the PET surface. The normalized emission spectra of the OLEDs are displayed in Figure 4.5(c). It shows that the manufactured phosphorescent OLED exhibits two emission peaks at wavelengths of 516 and 544 nm. The intensity ratios of these two peaks (I_{544}/I_{516}) calculated for the bare PET substrate and PET specimens treated 10, 20, and 60 times are equal to 0.977, 0.958, 0.921, and 0.854, respectively. Therefore, the amount of light emitted at a high scattering wavelength increased after surface treatment.

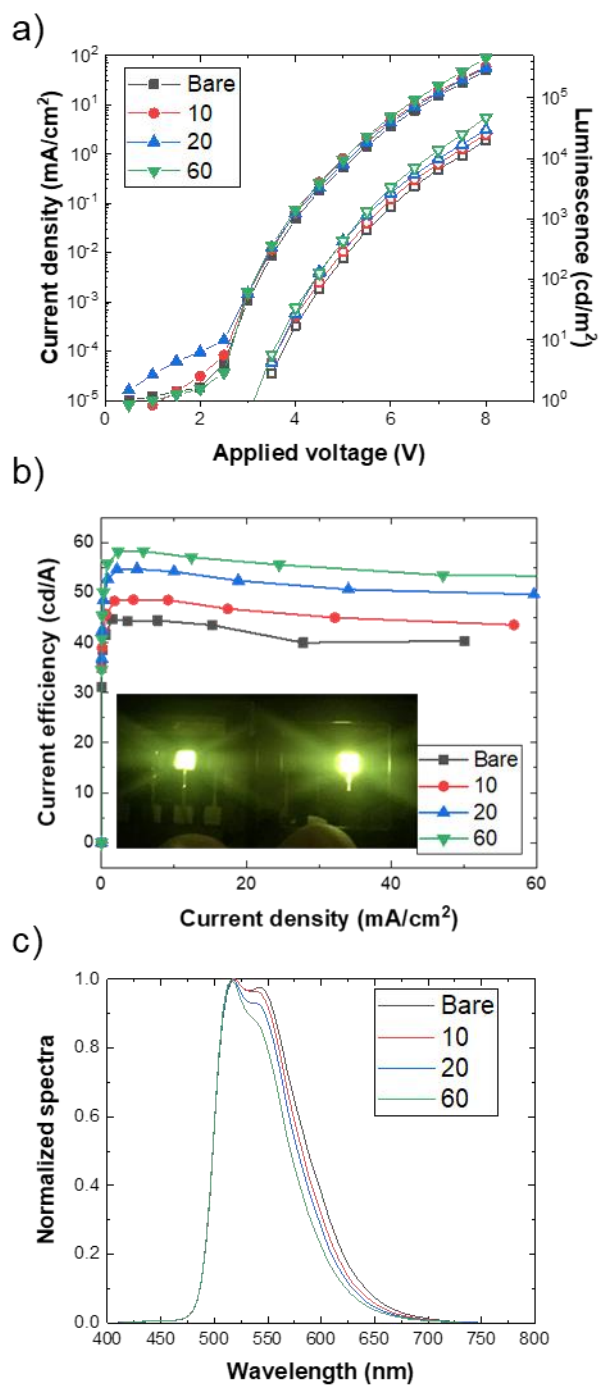


Figure 4.5. (a) Current–voltage characteristics (left axis) and luminescence–voltage characteristic (right axis), (b) current efficiencies, and (c) normalized emission spectra of the manufactured OLEDs.

4.4 Conclusions

Nanostructures can be effectively formed on PET surfaces via ion-beam irradiation. The produced structure had a hairy shape, and increasing the number of ion-beam irradiation treatments increased both its size and the surface roughness. The larger was the size of the nanostructure and the closer was the beam wavelength to 400 nm, the higher was the light scattering intensity. Using the PET substrate with a nano-hairy structure prepared by ion-beam treatment has increased the OLED efficiency by up to 30%. Furthermore, the nano-hairy structure fabricated on the OLED substrate could effectively emit the light trapped inside the OLED device to the outside. Future works in this area will investigate the OLED efficiency as a function of the shape and density of nanostructures by performing theoretical calculations.

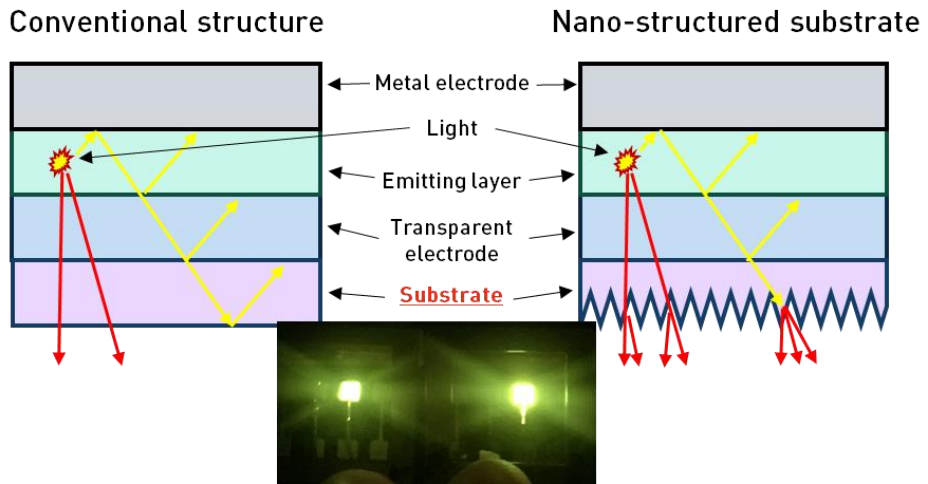


Figure 4.6. Graphical summary of Chapter 4.

4.5 Bibliography

1. C. W. Tang, S. A. Slyke, Organic electroluminescent diodes. *Applied Physics Letters* (1987) **51**, 12, 913-915
2. S. O. Jeon, K. H. Lee, J. S. Kim, et al., High-efficiency, long-lifetime deep-blue organic light-emitting diodes. *Nature Photonics* (2021) **15**, 208–215
3. T. -H. Han, Y. Lee, M. -R. Choi, et al., Extremely efficient flexible organic light-emitting diodes with modified graphene anode. *Nature Photonics* (2012) **6**, 105-110
4. S. Jung, S. Lee, M Song, et al., Extremely Flexible Transparent Conducting Electrodes for Organic Devices. *Advanced Energy Materials* (2013) **4**, 1, 1300474
5. D. Wang, J. Hauptmann, C. May, et al., Roll-to-roll fabrication of highly transparent Ca:Ag top-electrode towards flexible large-area OLED lighting application. *Flexible and Printed Electronics* (2021) **6**, 035001
6. J. B. Kim, J. H. Lee, C. K. Moon et al., Highly enhanced light extraction from surface plasmonic loss minimized organic light-emitting diodes. *Advanced Materials* (2013) **25**, 26, 3571-3577
7. S. Y. Kim, W. I. Jeong, C. Mayr, et al., Organic Light-Emitting diodes with 30% external quantum efficiency based on a horizontally oriented emitter. *Advanced Functional Materials* (2013) **23**, 31, 3896-3900

8. -Y. Kim, J. -J. Kim, Outcoupling efficiency of organic light emitting diodes and the effect of ITO thickness. *Organic Electronics* (2010) **11**, 6, 1010-1015
9. J. Frischeisen, D. Yokoyama, A. Endo, et al., Increased light outcoupling efficiency in dye-doped small molecule organic light-emitting diodes with horizontally oriented emitters. *Organic Electronics* (2011) **12**, 5, 809-817
10. C. W. Joo, J. -W. Shin, J. Moon, et al., Highly efficient white transparent organic light emitting diodes with nano-structured substrate. *Organic Electronics* (2016) **29**, 72-78
11. Lee, J. Y. Park, S. Gim, et al., Spontaneously Formed Nanopatterns on Polymer Films for Flexible Organic Light-Emitting Diodes. *Small* (2015) **11**, 35, 4480-4484
12. P. Yang, Q. Y. Bao, Z. Q. Xu, et al., Light out-coupling enhancement of organic light-emitting devices with microlens array. *Applied Physics Letters* (2010) **97**, 223303
13. Twersky, Rayleigh Scattering. *Applied Optics* (1964) **3**, 1150-1162
14. D. J. Lockwood, (2016). Rayleigh and Mie Scattering. In: Luo, M.R. (eds) Encyclopedia of Color Science and Technology. *Springer*, New York, NY. https://doi.org/10.1007/978-1-4419-8071-7_218

**Chapter 5. Improvement of Surface Adhesion of PET
Fiber and Copper for Antimicrobial Property without
Nano-structuring**

5.1 Introduction

Recently, severe acute respiratory syndrome coronavirus 2 (SARS-CoV-2), first discovered in Wuhan, Hubei Province, China, has spread rapidly worldwide, raising widespread health concerns. The World Health Organization (WHO) declared the coronavirus disease of 2019 (COVID-19) a pandemic on March 12, 2020. Over two years after the outbreak started in December 2019, over 300 million people have been infected, over 5 million people have died worldwide, and the infections and mortality rates have continued to increase [1]. Materials with antiviral properties have been used to prevent the spread of infectious diseases caused by these viruses. For example, ethanol-based disinfectants are the most commonly used sanitizers to treat humans, while chlorine-based and ammonium-based disinfectants are used for disinfecting living spaces [2,3]. These disinfectants effectively remove SARS-CoV-2 and other microorganisms but should be reapplied after use.

In contrast, copper is a sustainable antimicrobial material proven to inactivate viruses even on the nanometer scale. [4–11]. Recent studies have reported on the antiviral performance of copper against SARS-CoV-2. For example, Hutasoit reported that 96% of SARS-CoV-2 viruses placed on copper-coated steel plates were inactivated within two hours; however, no viruses were inactivated after five h of contact with uncoated stainless steel [12]. A study on SARS-CoV-2 inactivation as a function of the type of surface the virus contacts was conducted by Doremalen in 2020. They measured the time dependence of the titer of SARS-CoV-2 after it was placed on cardboard, stainless steel, plastic, and copper surfaces. On the copper surface, no viable SARS-CoV-2 was observed after four hours, whereas SARS-CoV-

2 was observed on the surface of the other materials even after twenty-four hours [13].

A key material used in masks and air purifier filters is the polymer membrane, which is an assembly of one-dimensional fibers. Air can pass through small pores in the membrane, but the fibers block droplets, bacteria, and dust. Nevertheless, while the polymer membrane can filter bacteria and viruses, the latter may remain on the membrane surface. This can cause secondary infections when the filters are replaced. Guo reported in 2020 that bacteria caught in high-efficiency particulate absorbing (HEPA) filters can survive longer than in dust. It was noted that bacteria in HEPA filters fill an ecological niche that may have been neglected in indoor environments [14].

A solution to this problem is the application of a copper coating to antibacterial and antiviral filters. However, it is essential to adhere the copper to the surface of the filter firmly because if the copper detaches from the filter, a human can inhale the copper, which becomes a toxin when inside the body [6]. In previous works, modifications to the surface of a filter using an ion-beam enabled the strong adherence of materials onto the filter [15–18]. The adhesion was accomplished without damaging the fibers of the filter. We found that SARS-CoV-2 was inactivated on the copper-coated mask within one hour [19].

In this study, we observed that the ion-beam surface treatment was very effective in improving the adhesion between the copper and the filter fibers. We found that the copper-coated filter inactivated more than 99.99% of four examples of bacteria (*Staphylococcus aureus* ATCC 6538, *Klebsiella pneumoniae* ATCC 4352, *Escherichia coli* ATCC 25922, and *Pseudomonas aeruginosa* ATCC 27853) and inactivated more than 99.8% of SARS-CoV-2.

The remainder of this paper is organized as follows. Section 2 explains the materials and methods we employed. Section 3 discusses the main results, and Section 4 describes the conclusions.

5.2. Materials and Methods

5.2.1. Materials

A polyethylene terephthalate (PET) (Airo Co., Ltd., Korea) filter with an average diameter of 30 μm and a surface density of 70 g/m^2 was used.

5.2.2. Ion Beam Treatment and Copper Sputtering Deposition

Figure 5.1a shows a schematic of the ion-beam treatment and copper sputtering processes. The process chamber is lab-made and includes the ion-beam source and direct-current magnetron sputtering source. After the chamber vacuum reached 1×10^{-5} torr of pressure, we proceeded with the subsequent process. First, oxygen gas was injected. Oxygen ion-beams were generated from a linear ion-beam source. The process was performed by varying the applied voltage, gas flow rate, and sample stage speed such that the total applied energy density was 1.45, 3.13, and 8.84 J/cm^2 . The latter three conditions were named Ion Beam 1, Ion Beam 2, and Ion Beam 3, respectively. Next, we measured the maximum temperature of the process by attaching labeled temperature-measuring tape (3E-50, 3E-70, 3E-90, 3E-110; Nichiyu Giken Kogyo Co., Ltd., Japan) to the sample stage. After the ion treatments were performed, copper was deposited using a direct current magnetron sputtering system with a purity target of more than 99.99%. Argon gas (purity > 99.99%) was injected with 30 sccm to apply a working pressure of 1.0 mTorr, and the copper was deposited with a power density of 2.55 W/cm^2 at a speed of 0.6 m/min in four separate runs. The thickness of the copper film was 30 nm. Detailed ion-beam and sputtering process conditions are in Table 5.1.

Table 5.1 Vacuum ion-beam surface treatment and sputtering process conditions.

Step 1	Ion Beam 1	Ion Beam 2	Ion Beam 3	Step 2	Cu Sputtering
Current (mA)	50	100	100	Gas / Flow rate (sccm)	Ar / 40
Applied voltage (kV)	0.6	1	2	Applied power (W)	200 W
Stage moving speed (meter/minute)	0.1	0.1	0.1	Stage moving speed (meter/minute)	0.6
Number of moving	2	2	2	Number of moving	4

5.2.3. SRIM Calculations

Stopping and Range of Ions in Matter (SRIM) is software that, as the name suggests, calculates the stopping and range of ions in matter [20–23]. This code can be used to calculate the amount of damage caused by ion irradiation. We used SRIM to calculate the number of phonons generated when oxygen ions collide with PET. In this study, there were two limitations in the SRIM calculations: 1) Oxygen is a diatomic molecule and can be decomposed into atoms when colliding with the PET surface, and 2) when oxygen ions collide with PET, a chemical reaction may be induced because oxygen is a reactive gas. Therefore, we made the following two assumptions to simplify the calculation of the relative number of phonons generated in the collisions: 1) When molecular oxygen ions collide with PET, the molecules decompose into two monatomic oxygen ions with half the energy [24], and 2) there are no chemical reactions between oxygen ions and PET substrates.

The density of the PET was 1.397 g/cm^3 , and the emitted ion energies were 180, 300, and 600 eV for Ion Beam 1, Ion Beam 2, and Ion Beam 3, respectively [17,18]. The relative number of phonons generated was calculated based on the ion energy of Ion Beam 3, with ion fluences of 2.52×10^{16} , 3.26×10^{16} , and 4.60×10^{16} ions/cm² for Ion Beam 1, Ion Beam 2, and Ion Beam 3, respectively.

5.2.4. Adhesion Test of Copper Deposited onto the Filter

The test involving the T-peeling of tape (3M VHB™ 4910 Tape; 3M, USA), illustrated in Figure 5.1b, was used to evaluate the adhesion force between the sputtered copper film and the filter fibers. After attaching tape to the copper deposited onto the filter, which was 10 mm wide, the end of the filter was fixed, and

the edge of the tape was pulled directly away from the filter at a 90° angle (forming a T-shape) to evaluate the peeling.

5.2.5. Observing the Surfaces of the Filters and Tapes

Filter samples with a size of 100 mm × 100 mm were prepared to measure the rate of change of the area of the filters. After completing the ion-beam treatment described in Section 2.2, the filter samples sizes were measured. We took digital pictures of the filter samples before and after the surface treatment on the grid, then calculated the change in their areas using commercial graphic drawing software (Rhino 3D; Version 6.0. Robert McNeel & Associates).

An optical microscope (ECLIPSE LV150N; Nikon, Japan) and field-emission scanning electron microscopy (FE-SEM; JSM 6700F, JEOL, Japan) were used to observe the surfaces of the filter and the detached tape.

5.2.6. Method for Evaluation of Antibacterial Performance

The copper-coated filter' antibacterial properties were evaluated, according to the KS K 0693:2016 test method, using the following bacteria: *Staphylococcus aureus* ATCC 6538, *Klebsiella pneumoniae* ATCC 4352, *Escherichia coli* ATCC 25922, and *Pseudomonas aeruginosa* ATCC 27853. The reduction rate was calculated using

$$\text{reduction rate (\%)} = (1 - B/A) * 100$$

where A is the colony-forming unit (CFU) per mL of the control group, and B is the experimental group.

5.2.7. Method for Evaluation of SARS-CoV-2 Elimination Performance

Figure 5.1c shows a schematic of the test system used to evaluate the SARS-CoV-2 elimination performance. For the aerosol test, a closed cylindrical chamber was produced using a vibrating nebulizer (HL100A; Health & Life Co., Ltd., New Taipei City, Taiwan). A 30 nm-thick copper-coated filter with a 70 mm diameter was installed in the chamber, and bioaerosols with SARS-CoV-2 (NCCCP43326, National Culture Collection for Pathogens, Cheongju, Korea) in 2% fetal bovine–serum containing Dulbecco's modified Eagle's medium (DMEM) (2.87×10^6 plaque-forming units (PFU)/mL) were sprayed onto the filter at a flow rate of 320 $\mu\text{L}/\text{min}$ for 300 s. For comparison, the same process was repeated using a filter that was not coated with copper. The filters were then immersed in 10 mL of DMEM for two minutes to separate the virus particles. The plaque assay was conducted in Vero76 cells (CRL-1587; American Type Culture Collection, Manassas, VA, USA) following the protocol described in a previous study [25]. The experiments with live SARS-CoV-2 were conducted at the biosafety level three laboratory in the Masan National Tuberculosis Hospital.

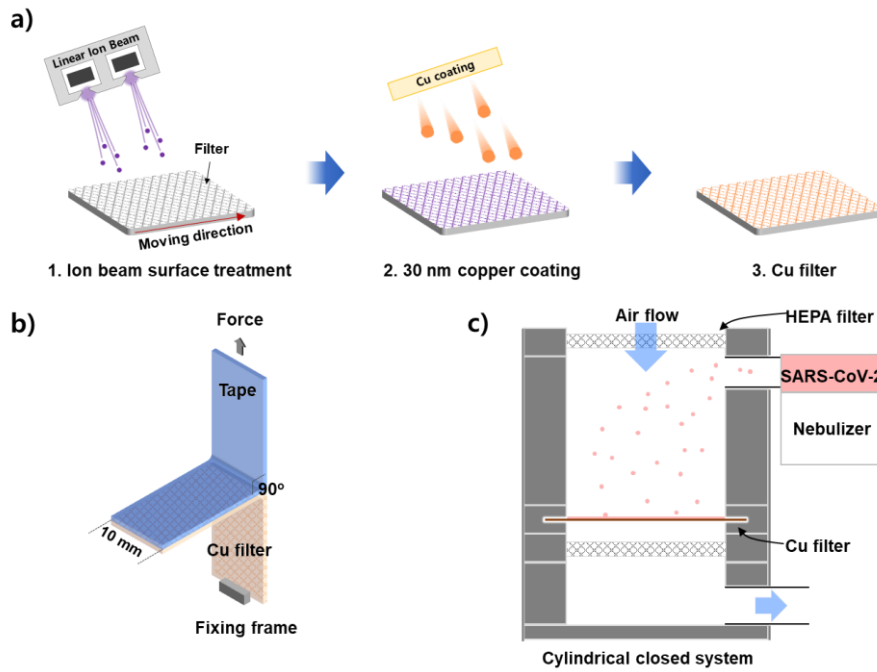


Figure 5.1. Diagrams of the a) ion beam treatment and copper sputtering processes, b) T-peeling test, and c) closed system used to evaluate aerosol filters.

5.3. Results and Discussion

5.3.1. Condition of the Filters After Ion Beam Treatment

The surfaces of the filters were checked for changes to the filter fibers caused by the oxygen ion-beam irradiation. Figure 5.2a shows the rate of change of the area of the 100 mm × 100 mm filter sample after treatment with the ion-beams. Ion Beams 1 and 2 caused area reduction rates of 0.33% and 0.46%, respectively. The area reduction rate caused by Ion Beam 3 was 3.81% (more than eight times that of Ion Beams 1 and 2), and the filter also contracted by approximately 2% in the longitudinal direction. The maximum process temperatures for Ion Beams 1 and 2 were 50 °C and 75 °C, respectively. In contrast, the process temperature for Ion Beam 3 was approximately 120 °C. The number of phonons generated was calculated using SRIM, and the relative amounts of generated phonons by ion-beam treatment are shown in Figure 5.2a (red axis label). The trends in the number of phonons generated and the maximum process temperature were similar because the phonons that were generated by colliding oxygen ions caused an increase in the material's temperature. For Ion Beam 3, the PET substrate reached a temperature of 120 °C, which is much higher than the glass transition temperature of PET [26].

Plateau-Rayleigh instabilities, in which a one-dimensional fluid is broken up into droplets due to the minimization of interfacial surface tension, can occur in a liquid column [27–29]. When the solid PET fiber reached the glass transition temperature or higher, the fluidity of the fibers increased, and the fibers became agglomerated. The agglomerated fibers blocked the filter's pores, causing a pressure loss and possible degradation of the filter performance. Optical microscope images

of the filters are shown in Figures 5.2b, c, d, and e. The agglomerated fibers were observed in the filter treated by Ion Beam 3 but not in the bare filter (without ion-beam treatment) or the filters treated by Ion Beam 1 or 2.

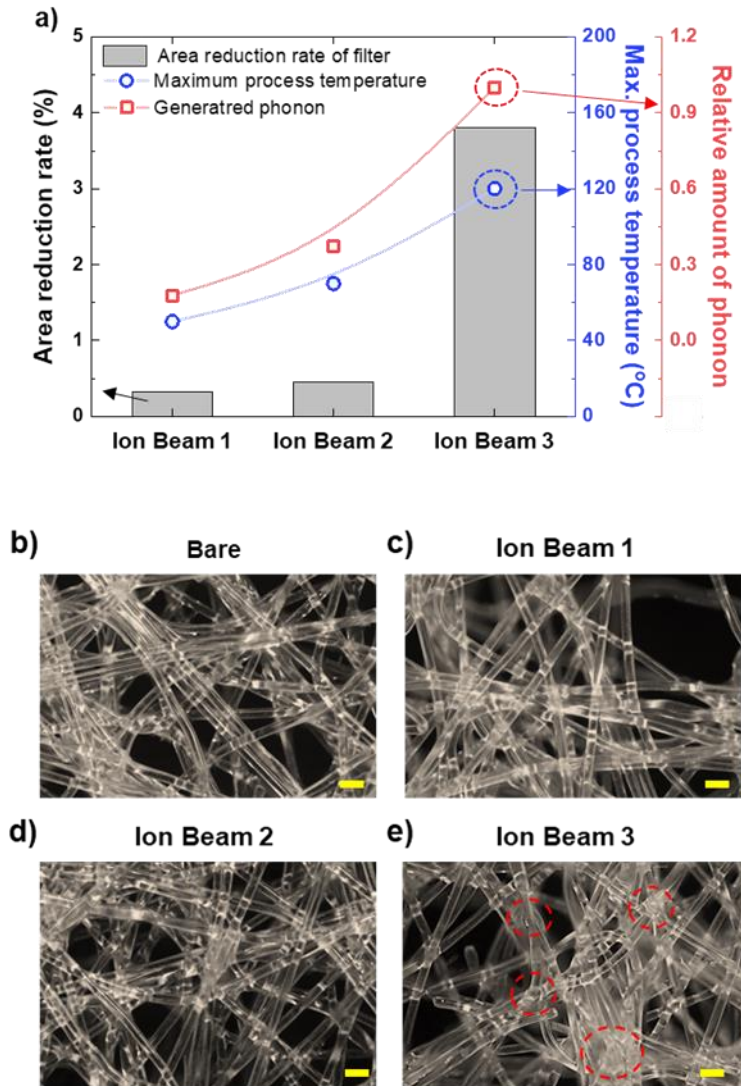


Figure 5.2. a) Rate of change of area of the filter (black axis on the left), maximum process temperature reached during ion beam treatment (blue axis on the right), and the relative number of phonons generated as calculated by SRIM (red axis on the right) under ion beam irradiations of 1.45, 3.13, and 8.84 J/cm². b–e) Optical microscope images (scale bar: 100 μ m) of the bare filter and the filters treated by Ion Beams 1, 2, and 3, respectively, under a dark field. The red-dashed circles show the areas where the fibers became agglomerated.

5.3.2. Composition and Adhesion Properties of the Filters

The SEM and energy-dispersive X-ray spectroscopy (EDS) mapping images of the bare filter and the copper-coated filter treated with Ion Beam 2 are shown in Figures 5.3a and b, respectively. The mass ratios of the major elements contained in each filter are shown in Figures 5.3c and d. Carbon and oxygen comprise the vast majority of the bare filter, whereas the copper-coated filter contained copper and oxygen; the copper was evenly distributed on its surface (see Figure 5.3b). Figure 5.4 shows the optical microscope images of the surface of the copper-coated filters. Figures 5.4a, b, and c show that the appearance of the bare filter and the filters treated by Ion Beams 1 and 2 were similar. However, the filter fibers treated by Ion Beam 3 were agglomerated, as shown in Figure 5.4d.

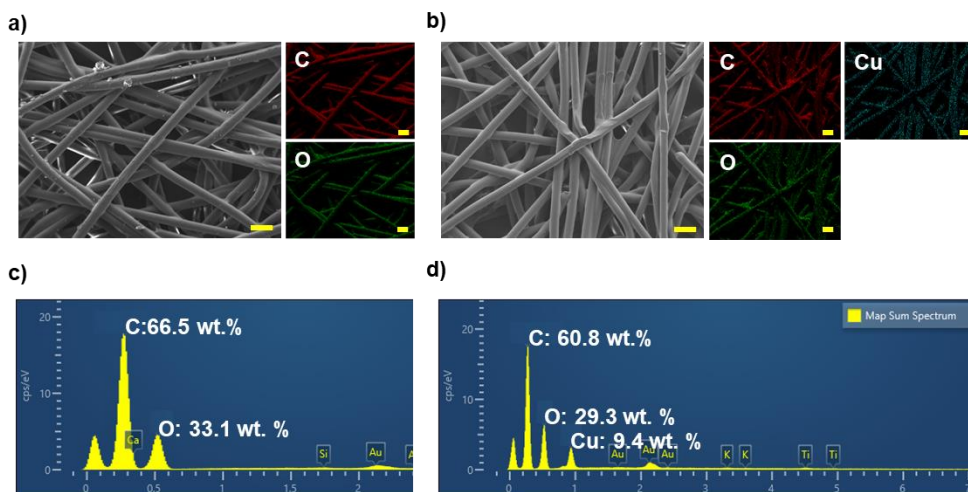


Figure 5.3. SEM (grayscale) and EDS mapping (color) images (scale bar: 100 μm) of the surfaces of the a) bare filter and b) copper-coated filter after ion beam treatment by Ion Beam 2. Atomic weight percentages of the surfaces of the c) bare filter and d) copper-coated filter after treatment by Ion Beam 2.

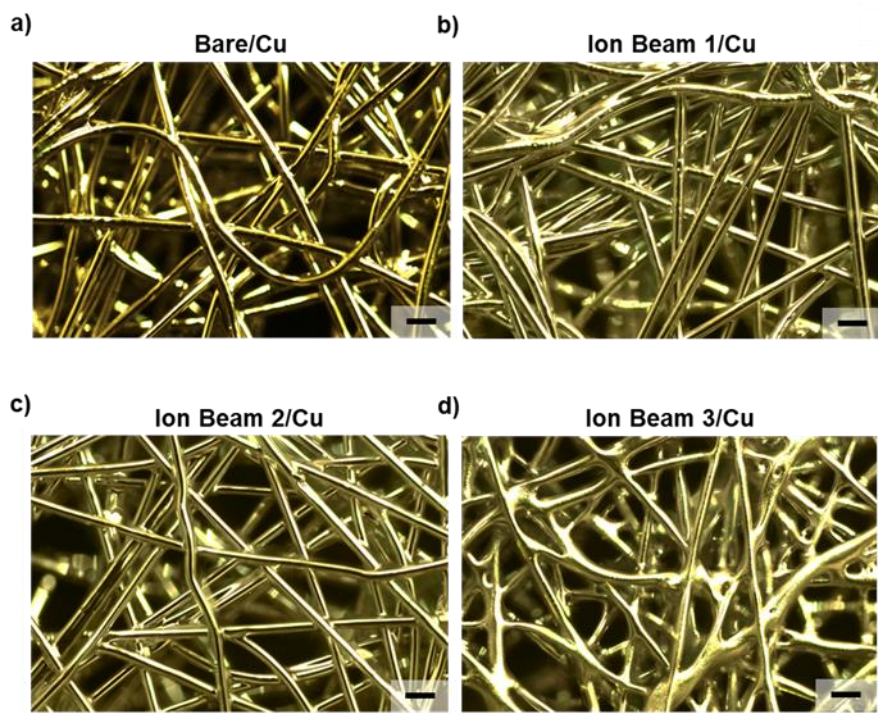


Figure 5.4. Optical microscope images (obtained under ultraviolet light with a peak wavelength of 360 nm; scale bar: 100 μm) of copper-coated filters treated with a) no ion beam (bare filter), b) Ion Beam 1, c) Ion Beam 2, and d) Ion Beam 3.

The strong adhesion between the filter fibers and the deposited copper film is essential because it can prevent copper nanoparticles (i.e., toxins) from entering the human body. The adhesion of the copper film deposited onto the filter fibers was evaluated using a T-peeling test with commercially available tape. This test confirmed that the peeling strengths of the filters treated with oxygen ion-beams were higher than those of the bare filter, as shown in Figure 5.5. The bare filter's peeling force per 10 mm of tape was 3.13 ± 0.05 N/cm, and the Ion Beam 2-treated filter exhibited the highest adhesion of 4.41 ± 0.11 N/cm. Figures 5.6a, b, c, and d show the results of the microscopic observations of the surfaces of the filters and the tape after it was peeled off, and Figure 5.6e shows a diagram of the evaluation of the tape. Figures 5.6a and b show that parts of the copper deposited onto the bare filter were released and transferred to the tape through cracks. This means that the adhesion between the copper film and the PET fibers was lower than the T-peeling result of 3.13 ± 0.05 N/cm. Figures 5.6c and d show the filter treated by Ion Beam 1 and the tape peeled off it, indicating that copper did not transfer from the fiber to the tape.

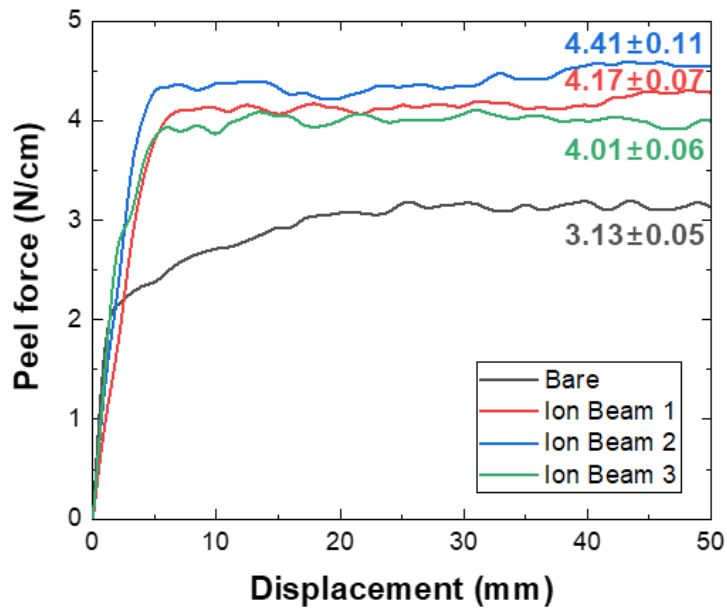


Figure 5.5. Peeling force per 10 mm of tape in the T-peeling test.

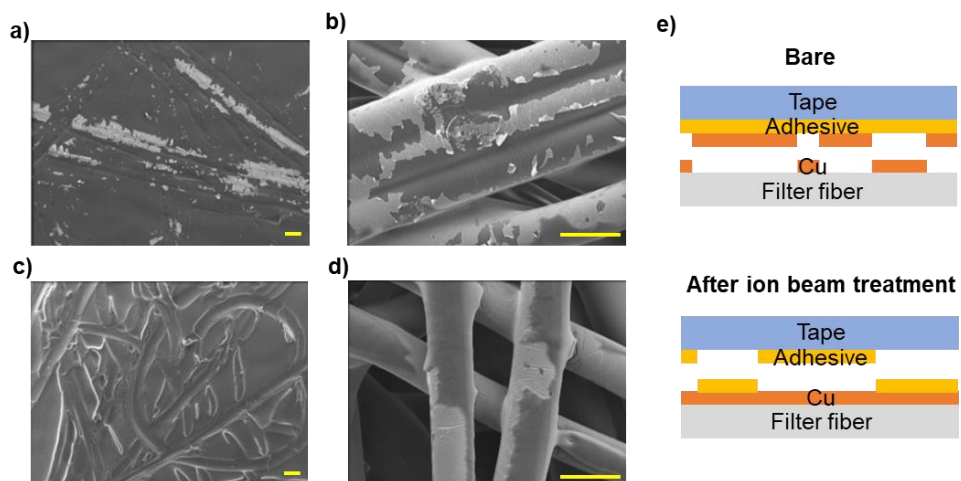


Figure 5.6. SEM images (scale bar, 50 micrometer) of the surface after peeling test a) tape surface and b) filter surface of bare, c) tape surface and d) filter surface treated under Ion Beam 1, and e) schematic diagram of the peeling test result of the untreated (bare) and ion beam-treated specimens

Figures 5.7 and 5.8 show low-magnification images and SEM/EDS of the filter and tape surfaces after the T-peeling test, respectively. Among the elements analyzed through EDS in Figure 5.8, carbon is included in the PET filter and adhesive of tape, copper is in the coated copper film, and silicon is in the adhesive of tape. It was confirmed through EDS analysis in Figure 5.8 that the tape's adhesive was transferred to the copper thin film, no the copper thin film was detached. The copper did not peel off the filters that underwent ion-beam treatment; instead, the tape's adhesive was transferred to the copper-coated filter surface. This indicates that the adhesion between the copper and the fibers in the filters that underwent ion-beam treatment was significantly more robust than that in the bare filter. This is reflected in Figure 5.5, which shows that the filters treated with the ion-beams exhibited a peeling force of 4.01 N/cm or more in the peeling test, compared to 3.13 N/cm for the bare filter.

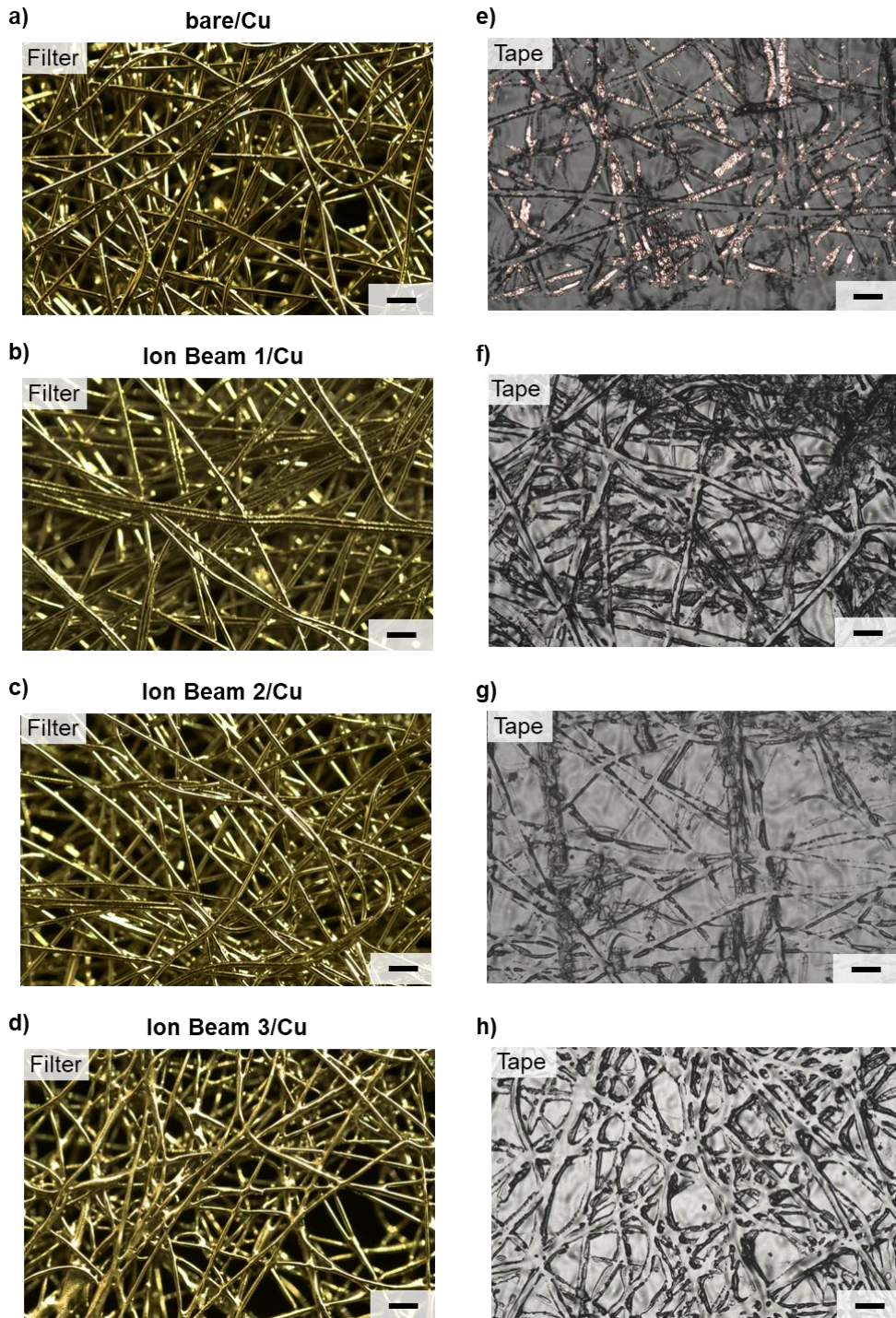


Figure 5.7. a-d) Optical microscope images (scale bar, 100 micrometer) of copper coated on filter surface after peeling test bare, Ion Beam 1, Ion Beam 2, and Ion Beam 3 under ultraviolet with 360 nm of peak wavelength, respectively. e-f) Optical microscope images (scale bar, 100 micrometer) of tape surface after peeling test bare, Ion Beam 1, Ion Beam 2, and Ion Beam 3 under white light.

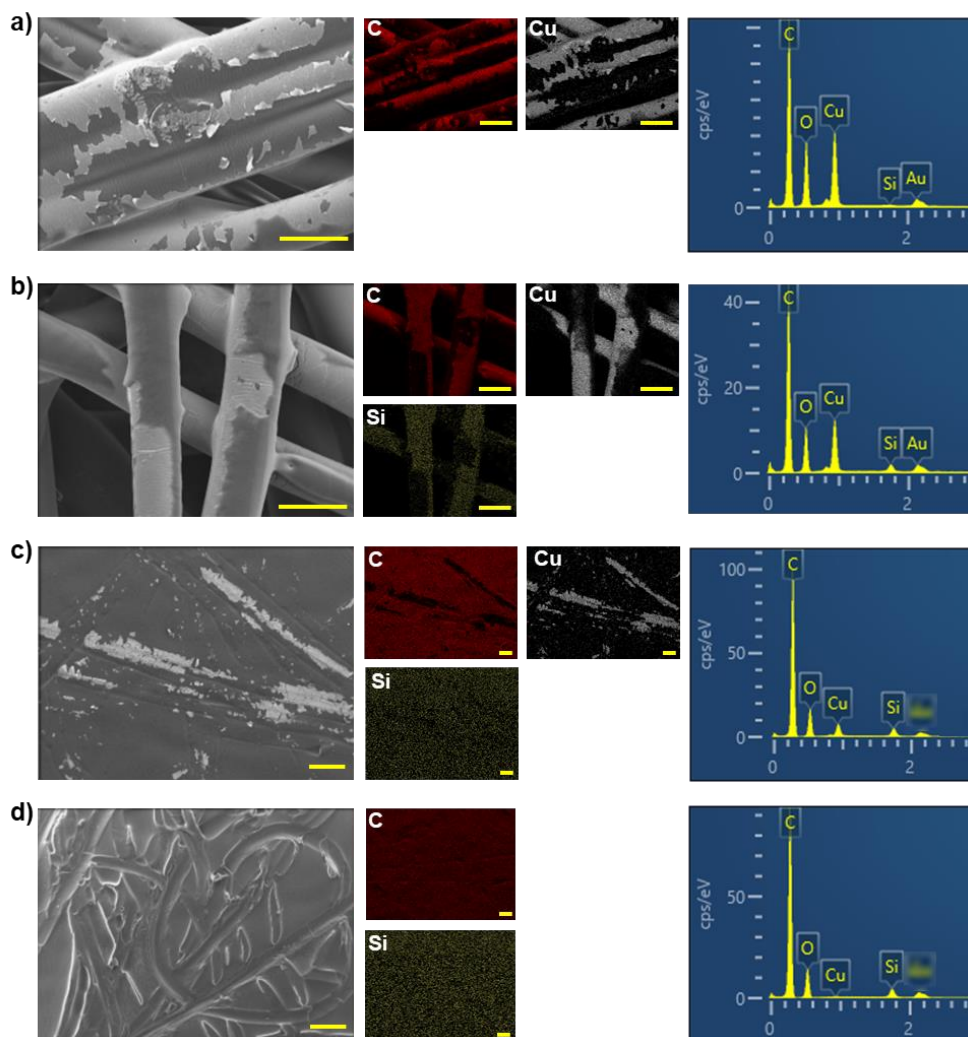


Figure 5.8. SEM and EDS mapping images (scale bar, 50 micrometer) of surface of copper-coated filter after tape peeling test of a) bare and b) Ion Beam 1. SEM and EDS mapping images (scale bar, 100 micrometer) of tape surface after tape peeling test of a) bare and b) Ion Beam 1.

5.3.3. Antibacterial Properties of the Copper-Coated Filter

The antibacterial properties of the copper-coated filter treated by Ion Beam 2 were investigated, according to the method described in Section 2.5, using the following bacteria: *Staphylococcus aureus* ATCC 6538, *Klebsiella pneumoniae* ATCC 4352, *Escherichia coli* ATCC 25922, and *Pseudomonas aeruginosa* ATCC 27853. The bare filter was used as the control sample. The antibacterial properties of the copper-coated filter are presented in Figures 5.9 and 5.10. All of the bacteria grew to approximately 10^7 CFU/mL in the control sample. In contrast, the bacteria grew to 10 CFU/mL or less in the copper-coated filter. This implies a reduction in bacterial growth by more than 99.999% (a logarithmic value greater than 5), confirming that the copper-coated filter had antibacterial properties.

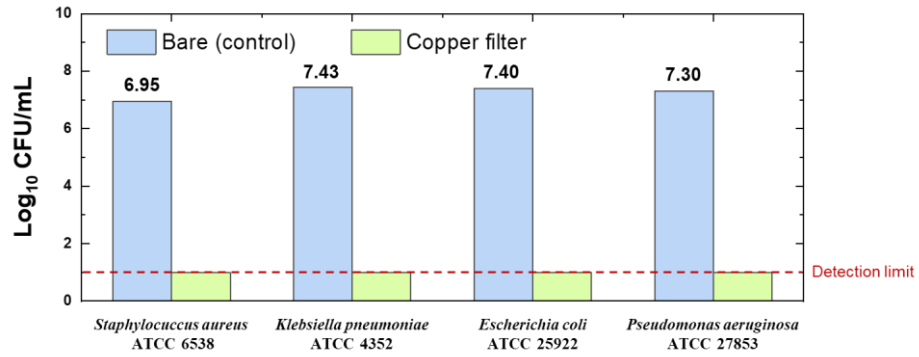


Figure 5.9. Antibacterial properties of bare filter (control) and copper coated filter against *Staphylococcus aureus* ATCC 6538, *Klebsiella pneumoniae* ATCC 4352, *Escherichia coli* ATCC 25922 and *Pseudomonas aeruginosa* ATCC 27853

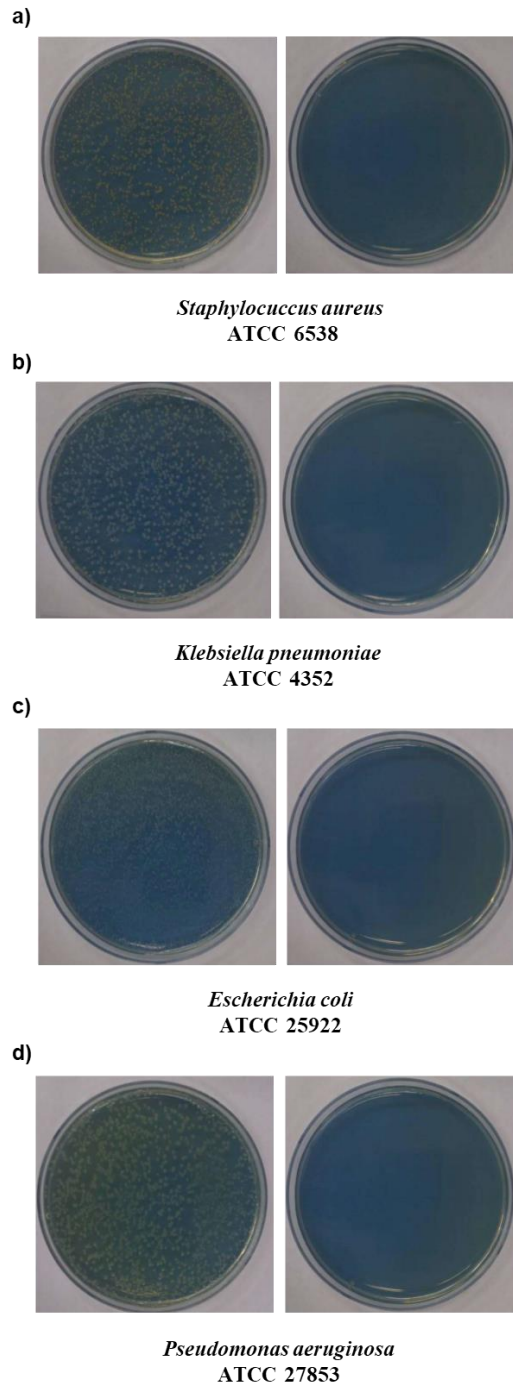


Figure 5.10. Antibacterial test results for a) *Staphylococcus aureus* ATCC 6538, b) *Klebsiella pneumoniae* ATCC 4352, c) *Escherichia coli* ATCC 25922, and d) *Pseudomonas aeruginosa* ATCC 27853. The left is the control group exposed to the normal filter, and the right is the experimental group exposed to the copper coated filter in each image.

5.3.4. Antiviral Properties of the Copper-Coated Filter

The SARS-CoV-2 evaluation system, composed of a copper-coated filter using a cylindrical device, is shown in Figure 5.1c. Figure 5.11a displays images of the bare filter and the copper-coated filter after spraying with SARS-CoV-2 aerosol, and Figure 5.11b shows images of the assay plates after being stained by crystal violet plaque. The copper-coated filter induced inactivation of the SARS-CoV-2 aerosol by more than 99.8% compared to the control group (as indicated in Figure 5.11b) as the detection limit (1.699 log PFU filter) was reached. By comparison, Hutasoit et al. reported that 96% of SARS-CoV-2 was inactivated on copper-coated stainless steel in two hours. In our previous work, we found that SARS-CoV-2 exposed to copper-coated masks for one hour was inactivated in a real-time polymerase chain reaction [12,19]. These results and those found in this study demonstrate that copper can eliminate viruses after short periods of physical contact.

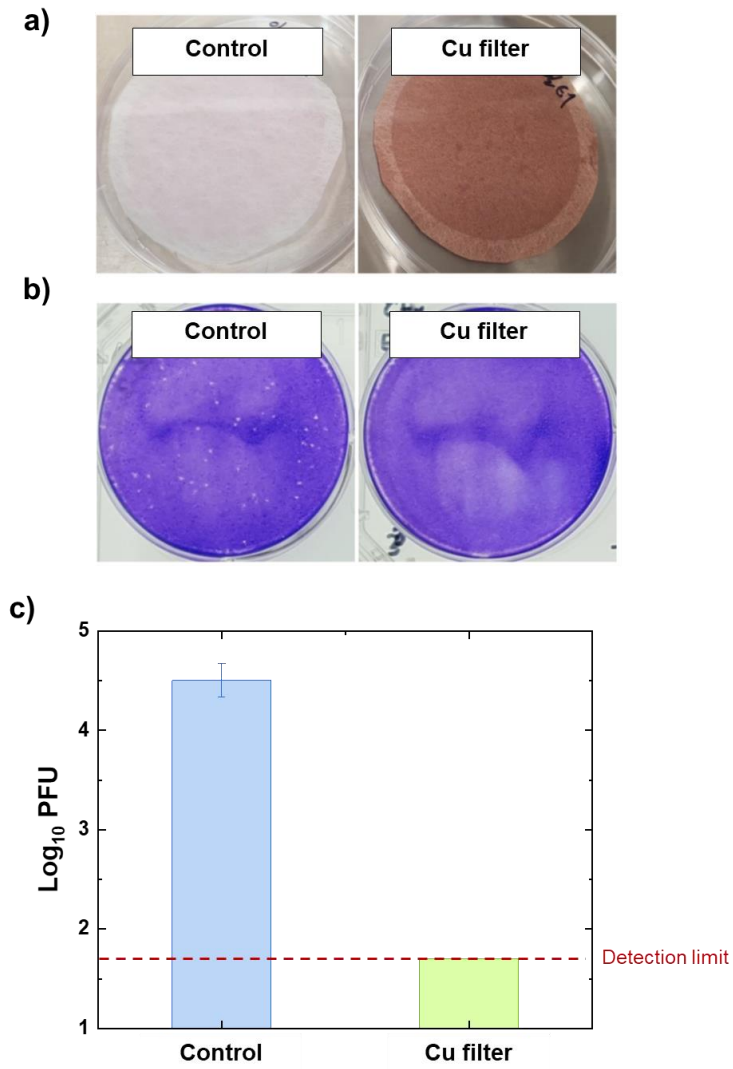


Figure 5.11. a) images of copper coated filter and non-copper coated filter after spraying SARS-CoV-2 aerosol, b) images of crystal violet stained plaque assay plates, and c) inactivation of SARS-CoV-2

5.4. Conclusions

In summary, an ion-beam treatment technique was used to strongly adhere copper to the fibers found in a filter, the core component in masks and air purifiers. After treating the filter surface with an oxygen ion-beam, strong adhesion of at least 4.01 N/cm was achieved between the copper and the filter fibers. Furthermore, we found that the ion-beam–surface treatment process should be performed below the glass transition temperature of filter material to prevent damaging the filter fibers. The copper-coated filter developed in this study demonstrated a capability to remove bacteria and viruses remaining on its surface. However, there is a high possibility that bacteria and viruses not caught in the filter cannot be removed, and studies on the possibility of changing the antibacterial and antiviral properties by accumulated dust, adsorbed moisture, and oxidized copper on the surface when the filter is used for a long period have not been conducted. Nevertheless, the use of this copper coating filter can minimize the risk of secondary infections that may occur during replacement and disposal of filters compared to conventional. Thus, copper-coated filters should be able to effectively and sustainably prevent infections caused by not only SARS-CoV-2 but also unknown viruses that may occur in the future. Moreover, unlike coating copper on the finished mask product that we previously reported, depositing copper on the filter fiber is advantageous because it provides a wider range of personal hygiene supplies utilization [19]. The copper coating filter developed in this study can be used for masks, filters for air purifiers, and building air conditioning filters, which can lead to a healthy life against airborne infectious diseases.

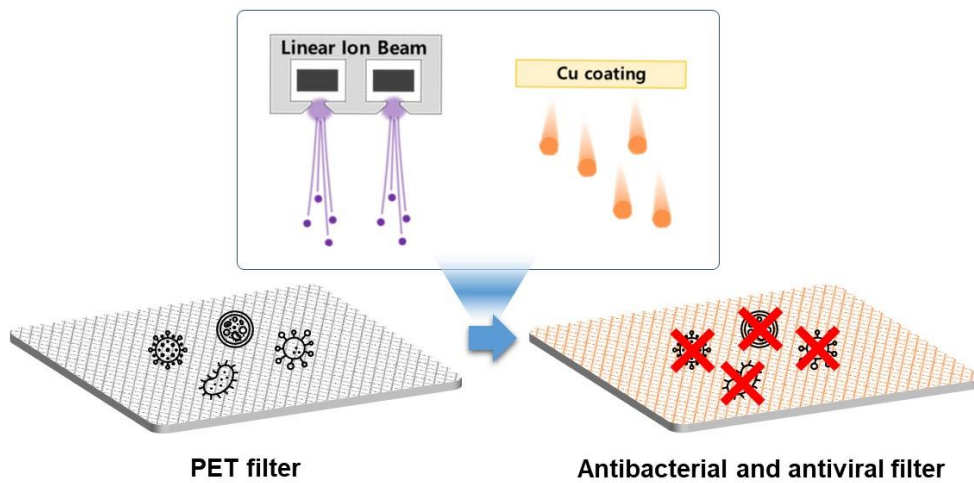


Figure 5.12. Graphical summary of Chapter 5.

5.5. Bibliography

1. COVID-19 Dashboard, Available online: <https://coronaboard.com/global/> (accessed on 16 Feb. 2022).
2. Leslie, R.A.; Zhou, S.S.; Macinga, D.R. Inactivation of SARS-CoV-2 by commercially available alcohol-based hand sanitizers. *Am. J. Infect. Control* **2021**, *49*, 401–402, doi:10.1016/j.ajic.2020.08.020.
3. Xiling, G.; Yin, C.; Ling, W.; Xiaosong, W.; Jingjing, F.; Fang, L.; Xiaoyan, Z.; Yiyue, G.; Ying, C.; Lunbiao, C.; et al. In vitro inactivation of SARS-CoV-2 by commonly used disinfection products and methods. *Sci. Rep.* **2021**, *11*, 2418, doi:10.1038/s41598-021-82148-w.
4. Souli, M.; Galani, I.; Plachouras, D.; Panagea, T.; Armaganidis, A.; Petrikkos, G.; Giamarellou, H. Antimicrobial activity of copper surfaces against carbapenemase-producing contemporary Gram-negative clinical isolates. *J. Antimicrob. Chemother.* **2013**, *68*, 852–857, doi:10.1093/jac/dks473.
5. Halbus, A.F.; Horozov, T.S.; Paunov, V.N. Colloid particle formulations for antimicrobial applications. *Adv. Colloid Interface Sci.* **2017**, *249*, 134–148, doi:10.1016/j.cis.2017.05.012.
6. Vincent, M.; Duval, R.E.; Hartemann, P.; Engels-Deutsch, M. Contact killing and antimicrobial properties of copper. *J. Appl. Microbiol.* **2018**, *124*, 1032–1046, doi:10.1111/jam.13681.

7. Grass, G.; Rensing, C.; Solioz, M. Metallic copper as an antimicrobial surface. *Appl. Environ. Microbiol.* **2011**, *77*, 1541–1547, doi:10.1128/AEM.02766-10.
8. Weaver, L.; Michels, H.T.; Keevil, C.W. Survival of *Clostridium difficile* on copper and steel: futuristic options for hospital hygiene. *J. Hosp. Infect.* **2008**, *68*, 145–151, doi:10.1016/j.jhin.2007.11.011.
9. Noyce, J.O.; Michels, H.; Keevil, C.W. Use of copper cast alloys to control *Escherichia coli* O157 cross-contamination during food processing. *Appl. Environ. Microbiol.* **2006**, *72*, 4239–4244, doi:10.1128/AEM.02532-05.
10. Yougbaré, S.; Mutalik, C.; Krisnawati, D.I.; Kristanto, H.; Jazidie, A.; Nuh, M.; Cheng, T.-M.; Kuo, T.-R. Nanomaterials for the Photothermal Killing of Bacteria. *Nanomaterials* **2020**, *10*, 1123. <https://doi.org/10.3390/nano10061123>.
11. Yougbare, S.; Chang, T.-K.; Tan, S.-H.; Kuo, J.-C.; Hsu, P.-H.; Su, C.-Y.; Kuo, T.-R. Antimicrobial Gold Nanoclusters: Recent Developments and Future Perspectives. *Int. J. Mol. Sci.* **2019**, *20*, 2924. <https://doi.org/10.3390/ijms20122924>.
12. Hutasoit, N.; Kennedy, B.; Hamilton, S.; Luttick, A.; Rahman Rashid, R.A.; Palanisamy, S. Sars-CoV-2 (COVID-19) inactivation capability of copper-coated touch surface fabricated by cold-spray technology. *Manuf. Lett.* **2020**, *25*, 93–97, doi:10.1016/j.mfglet.2020.08.007.
13. Neeltje van Doremalen, T.B., Morris, D.H.; Holbrook, M.G.; Gamble, A.; Williamson, B.N.; Tamin, A.; Harcourt, J.L.; Thornburg, N.J.; Gerber, S.I.; Lloyd-Smith, J.O.; de Wit, E.; Munster, V.J. Aerosol and

Surface Stability of SARS-CoV-2 as Compared with SARS-CoV-1. *N. Engl. J. Med.* **2020**, 382, doi:10.1056/NEJMc2004973.

14. Guo, J.; Xiong, Y.; Kang, T.; Xiang, Z.; Qin, C. Bacterial community analysis of floor dust and HEPA filters in air purifiers used in office rooms in ILAS, Beijing. *Sci. Rep.* **2020**, 10, 6417, doi:10.1038/s41598-020-63543-1.
15. Esmail, A.; Pereira, J.R.; Zoio, P.; Silvestre, S.; Menda, U.D.; Sevrin, C.; Grandfils, C.; Fortunato, E.; Reis, M.A.M.; Henriques, C. et al. Oxygen Plasma Treated-Electrospun Polyhydroxyalkanoate Scaffolds for Hydrophilicity Improvement and Cell Adhesion. *Polymers (Basel)* **2021**, 13, doi:10.3390/polym13071056.
16. Hegemann, D.; Brunner, H.; Oehr, C. Plasma treatment of polymers for surface and adhesion improvement. *Nucl. Instrum. Methods Phys. Res. B* **2003**, 208, 281–286, doi:10.1016/s0168-583x(03)00644-x.
17. Lee, S.; Byeon, E.; Jung, S.; Kim, D.G. Heterogeneity of hard skin layer in wrinkled PDMS surface fabricated by Ar ion-beam irradiation. *Sci. Rep.* **2018**, 8, 14063, doi:10.1038/s41598-018-32378-2.
18. Lee, S.; Byun, E.-Y.; Kim, J.-K.; Kim, D.-G. Ar and O₂ linear ion beam PET treatments using an anode layer ion source. *Curr. Appl. Phys.* **2014**, 14, S180–S182, doi:10.1016/j.cap.2013.12.031.
19. Jung, S.; Yang, J.Y.; Byeon, E.Y.; Kim, D.G.; Lee, D.G.; Ryoo, S.; Lee, S.; Shin, C.W.; Jang, H.W.; Kim, H.J.; et al. Copper-Coated Polypropylene Filter Face Mask with SARS-CoV-2 Antiviral Ability. *Polymers (Basel)* **2021**, 13, doi:10.3390/polym13091367.

20. Guenther, M.; Gerlach, G.; Suchaneck, G.; Sahre, K.; Eichhorn, K.-J.; Wolf, B.; Deineka, A.; Jastrabik, L. Ion-beam induced chemical and structural modification in polymers. *Surf. Coat. Technol.* **2002**, 158–159, 108–113.
21. Lee, E.H. Ion-beam modification of polymeric materials fundamental principles and applications. *Nucl. Instrum. Methods Phys. Res. B* **1999**, 151, 29–41.
22. Zaki, M.F. Effect of Ar ion on the surface properties of low density polyethylene. *Spectrochim. Acta. A Mol. Biomol. Spectrosc.* **2016**, 159, 177–183, doi:10.1016/j.saa.2016.01.044.
23. Ziegler, J.F. SRIM-2003. *Nucl. Instrum. Methods Phys. Res. B* **2004**, 219–220, 1027–1036, doi:10.1016/j.nimb.2004.01.208.
24. Hössinger, A. Simulation of Ion Implantation for ULSI Technology. PhD, Technische Univ, Wien, July 2000.
25. Mendoza, E.J.; Manguiat, K.; Wood, H.; Drebot, M. Two Detailed Plaque Assay Protocols for the Quantification of Infectious SARS-CoV-2. *Curr. Protoc. Microbiol.* **2020**, 57, ecpmc105, doi:10.1002/cpmc.105.
26. Wang, Y.-H.; Wang, W.-H.; Zhang, Z.; Xu, L.; Li, P. Study of the glass transition temperature and the mechanical properties of PET/modified silica nanocomposite by molecular dynamics simulation. *Eur. Polym. J.* **2016**, 75, 36–45, doi:10.1016/j.eurpolymj.2015.11.038.
27. Plateau, J. Experimental and Theoretical Steady State of Liquids Subjected to Nothing but Molecular Forces; Gauthiers-Villars: Paris, France, 1873.

28. Rayleigh, F. On the Instability of Jets. In Proc. Lond. Math. Soc., London, United Kingdom, 1 November 1878.
29. Goren, S.L. The Shape of a Thread of Liquid Undergoing Break-up. *J. Colloid Sci.* **1964**, 19, 81–86.

Chapter 6. Conclusions

In summary, we have identified the main principle of forming nanostructures on polymer surfaces and their potential application. Based on this principle, a new surface treatment technology that can be applied even to thin 1D fibers with a thickness of several tens of micrometers while minimizing the polymer surface damage has been developed.

When the ions emitted from LIS collide with the polymer, they lose energy due to the interactions with the nuclei and electrons of the medium. The energy losses caused by atomic nuclei are elastic collisions due to Coulombic repulsive forces, causing the atoms to be displaced, sputter, or recoil. Meanwhile, the energy losses due to electrons are inelastic collisions, which can excite or ionize atoms in the internal medium and ultimately be converted into light or thermal energy. These phenomena are the main reasons for the changes occurring on polymer surface, and SRIM calculations were performed in this study to predict nucleus and electron energy losses.

A nano-dimple structure was formed when a PEN substrate was irradiated by an ion beam with a fluence of $10^{16}/\text{cm}^2$ in the energy range of 0.6–1.08 keV. The produced nano-dimples had diameters of approximately 100 nm and peak-to-valley heights. They were generated due to the sputtering imbalance caused by the very low surface roughness and adequately described by the DKS model. By solving the continuum equation using this model, it was found that the analysis method used for semiconductor materials was applicable to polymers.

A wrinkle structure was formed by irradiating PDMS with an oxygen ion beam at a density of approximately $10^{15}/\text{cm}^2$ and energies of 0.6–1.08 keV. As a result, a

hardskin layer with increased number of SiO₂ bonds was fabricated on the PDMS surface, as confirmed by XPS. By conducting XPS depth profiling, changes in various carbon PDMS bonds were observed along the depth direction. The DPA values were calculated by Equation (3.1). The bond dissociation energy (E_d) and density of PDMS are well-known values; the $(dE/dx)_{\text{nuclear}}$ magnitudes were calculated by SRIM, and ion flux was measured experimentally. By comparing the obtained DPA values with the changes in carbon bonding determined by XPS, it was found that these changes occurred at DPA values of 1.5 or higher, which indicated that the bonds were broken or that the recombination of dangling bonds occurred. This recombined layer became a hardskin layer with a higher hardness than that of PDMS. The thickness of the hardskin layer ranging from 7 to 14 nm was predicted by SRIM by calculating the depth of nuclear stopping. The Young's modulus of the hardskin layer (2–4 GPa) was determined from the AFM data (wrinkle wavelength and amplitudes), Equations (1.8)–(1.11), and the hardskin layer thickness.

When a PET substrate was irradiated by an oxygen ion beam with a fluence of $10^{16}/\text{cm}^2$ and energy of 0.6 keV, a nano-hairy structure was formed, which significantly increased the haziness of the PET surface due to the more intense light scattering. The shorter was the wavelength, the greater was the haziness. When the particle diameter was 1/10 of the beam wavelength, Rayleigh scattering mainly occurred. Meanwhile, as the particle diameter increased, the scattering process more resembled Mie scattering. Because the nanostructure size was 40–60 nm, it was strongly affected by Rayleigh scattering at wavelengths of 600 nm and gradually deviated from Rayleigh scattering at wavelengths below 600 nm. To determine the change in the light extraction efficiency due to nanostructures, an OLED with the irradiated PET substrate was manufactured, and its efficiency evaluation was

conducted. As a result, the OLED efficiency increased by 30% after irradiation. By evaluating the light emission characteristics at different wavelengths, it was found that the amplification of the low wavelength light with a large scattering degree considerably increased. Furthermore, the nanostructure formed on the PET substrate helped extract the light trapped inside the OLED to the outside. Because this process involved a vacuum ion beam and a polymer film, it is suitable for roll-to-roll processing during the formation of surface nanostructures, transparent electrode deposition, and top electrode deposition.

The nanostructure formation technology based on the irradiation of PET substrates with ion beams can also be applied to surface modification. It is well known that oxygen ion beams produce hydrophilic surfaces, which are hard to combine with micrometer-thick fibers. When high energy is applied to a fiber, heat is generated, which increases the fluidity of the fiber material, resulting in agglomeration due to the Rayleigh–Plateau instability. The number of generated phonons predicted by performing SRIM calculations strongly correlated with the process temperature. High adhesion was achieved when copper was deposited onto the surface-treated 1D fibers, and the antibacterial and antiviral properties of the produced filter were confirmed. After exposing bacteria and viruses to the filter for 1 h, more than 99% of four types of bacteria and coronavirus were killed.

The principle of forming a vacuum polymer nanostructure using an ion beam formulated in this work and developed technology can be easily applied in the industry because of the possibility of roll-to-roll expansion. Furthermore, the processes involving environmentally safe oxygen and argon gases can contribute to the development of eco-friendly industries in the future. In addition, the obtained

results obtained may be potentially applied to various polymers such as polyimide and polytetrafluoroethylene besides PEN, PDMS, and PET.

Abstract in Korean

최근 나노기술의 급격한 발달은 일상생활에서도 수많은 나노 소재가 활용될 수 있게 하였다. 나노미터 스케일의 패터닝이 활용되는 반도체, 디스플레이나 차량에 활용되는 나노코팅 필름, 미세먼지 등 유해물질을 거르기 위한 필터, 치료를 위한 단백질이나 유전물질 등에 이르기까지 재료, 기계, 전자, 생명과학에 이르는 넓은 범위에 활용되고 있다. 수많은 나노 소재 중 나노 구조체를 형성시킨 표면은 평평한 표면과는 다른 물리적인 특성을 가지게 되고, 이는 표면에 새로운 기능을 부여해줄 수 있다. 나노구조체가 형성된 표면은 표면에너지를 극대화시켜 친수를 초친수로, 발수를 초발수로 만들 수 있고, 넓은 비표면적을 활용하여 점착, 접착에 활용하거나 화학반응 속도를 증가시킬 수 있다. 또한, 빛의 산란, 회절, 플라즈몬 공명 현상을 발생시켜 저반사, 컬러링 등의 새로운 광학 특성을 부여할 수 있다.

나노구조체의 제작은 Lithography, Imprinting, 자가나노구조화 등의 Top-down 방법과 다양한 방법으로 나노 물질을 성장시키는 Bottom-up 방식으로 구분할 수 있다. Top-down 방식 중 Lithography 와 Imprinting 은 매우 정교한 패턴의 형성이 가능한 방법이지만, 패터닝을 위한 마스크가 필요하고 공정 가격이 매우 높은 편이다. 반도체나 플라즈몬 공명을 활용한 컬러링 소자와 같이 매우 정교하고 규칙적인 패턴이 필요한 응용처에는 매우 적합한 방법이지만, 대량생산이 중요한 저반사, 초친수/초발수, 촉매와 같은 분야에서는 리소그래피, 임프린팅과는 다른 생산 방법이 요구된다.

선형 이온빔은 10^{-3} Torr 정도의 진공에서 수 kV 급의 이온을 방출시켜 표면을 개질시키는 장치이다. 플라즈마 발생 장치의 일종으로써, 널리

사용되는 RF 타입의 플라즈마에 비해 이온 에너지 조절, 입사 각도 조절 등이 용이하고, 스퍼터와 작동하는 진공도 영역대가 유사하고, 길이의 확장이 용이하여 대량 생산에 유리한 장점이 있다. 선형 이온빔의 공정 조건에 따라 식각, 산화막/질화막의 생성, 표면에너지 변화, 표면형상 변화 등 표면에 다양한 물리적, 화학적인 특성 변화를 발생시킬 수 있다.

본 연구에서는 선형 이온빔을 활용하여 PEN, PDMS, PET 와 같이 일상에서 활용되는 고분자 필름의 표면 형상을 제어하고, 이의 원인을 규명하였다. PEN 에 이온빔을 조사하면 약 100 nm 전후의 지름과 높이를 가지는 나노돔플이 형성된다. 형성된 나노돔플은 PEN 의 광학적 특성을 변화시킨다. PEN 표면 나노구조의 형성은 DKS 모델을 활용하면 표면 구조 형성이 잘 묘사됨을 확인하였다. DKS 모델에 부합한다는 것은 PEN 표면에 존재하는 수 nm 이하의 아주 작은 Roughness 에서 발생하는 위치에 따른 스퍼터링율의 차이가 나노돔플 형성의 원인이라는 의미이다.

PDMS 표면에 이온빔을 조사하면 나노링클 구조가 만들어진다. XPS 표면 분석을 통해 표면에 PDMS 의 SiO 결합이 SiO₂ 결합에 가까운 Hardskin 층으로 변화함을 확인하였다. 탄소 기반 Bond 의 Dissociation Energy (Ed) 값과, SRIM 을 통해 계산한 Nuclear Stopping ($(dE/dx)_{\text{nuclear}}$)을 활용하여 깊이에 따른 Displace per Atom (DPA) 값을 계산하였고, 이를 XPS Depth Profiling 을 활용해 측정된 탄소 Bond 의 변화와 비교하였다. DPA 값이 1.5 이상인 Bond 인 H-CH₂, C-Si 가 크게 변화함을 확인할 수 있었고, DPA 값의 계산을 통해 Bond 의 분해를 간접적으로 예측할 수 있다는 결론을 내릴 수 있었다.

이온빔을 조사한 PET 표면은 나노헤어리 구조가 형성되었다. 형성한 나노헤어리 구조는 PET의 산란도를 크게 증가시킴을 확인하였다. 산란도는 나노구조체의 크기가 커질수록 증가하였다. 산란은 나노구조체의 크기와 파장에 큰 영향을 받는데, 형성한 나노구조체의 크기는 약 40~60 nm의 크기를 가지고 있기 때문에 가시광 영역의 빛 (약 400~800 nm 영역)은 Rayleigh 산란 거동에 큰 영향을 받는다. Rayleigh 산란은 파장의 4 제곱에 반비례하기 때문에 가시광선에서 Blue 쪽에 해당하는 파장이 Red 계열의 파장보다 훨씬 큰 산란도를 보이고, 이는 측정한 Hazeiness 결과와 잘 부합한다. 제작한 나노헤어리 기판을 활용하여 OLED를 제작하였다. OLED는 소자 내부에 갇힌 빛을 외부로 추출시켜주는 것이 효율 향상에 있어 매우 중요한 요소이다. 나노헤어리 PET 기판에 제작한 OLED는 일반 PET에 제작한 OLED에 비해 효율이 최대 30%까지 증가했음을 확인하였고, 이는 PET 표면의 나노헤어리 구조는 기판에 갇힌 빛을 외부로 추출시켜주는데 매우 효율적임을 의미한다.

코로나 바이러스 방역용 마스크, 공기청정기용 헤파 필터 등 1D 섬유형 집합으로 구성된 필터의 표면처리 기술의 개발은 매우 중요한 요소이다. 앞서 필름상 나노구조를 형성하는 이온빔을 필터 원단에 수행하게 되면, 수십 마이크로미터 두께의 PET 섬유가 Rayleigh-Plateau 불안정성에 의해 서로 뭉치는 현상이 발생한다. 이러한 Rayleigh-Plateau 불안정성이 발생하지 않게 하기 위해서는 필터 표면처리를 수행할 때 온도 변화를 억제해야 하며, 온도 변화량은 SRIM을 통해 계산한 Phonon의 양과 유사한 상관관계를 가질 수 있음을 확인하였다. 필터 섬유의 손상을 억제하면서 높은 밀착성을 얻을 수 있는 이온빔 표면처리 공정 조건을 개발하여 이를 필터 원단에 수행했다. 그

결과, 필터 섬유와 구리가 높은 밀착성을 가지게 되었다. 구리가 코팅된 필터를 코로나 바이러스 (SARS-CoV-2)와 4 종류의 세균에 대해 항바이러스성과 항균성을 평가하였고, 그 결과 1 시간 노출시 99% 이상의 바이러스와 세균이 사멸됨을 확인할 수 있었다.

본 연구를 통해 고분자의 표면처리를 수행하여 표면 형상의 변화를 관찰하였고, SRIM 계산을 통하여 형상 변화 거동과 원인을 예측할 수 있음을 밝혀냈다. SRIM 계산은 고분자 결합에 대한 변수가 계산에 깊이 반영되지 않아 계산 결과를 정량적으로 일치시킬 수는 없었으나, 정성적으로 예측이 가능함을 확인했다. 본 연구에서 수행한 고분자 소재인 PEN, PDMS, PET 뿐만 아니라 Polyimide (PI), Polytetrafluoroethylene (PTFE), Polystyrene (PS) 등 다양한 고분자에도 적용하여 이온빔 조사시의 표면 변화거동을 미리 예측할 수 있을 것이다. 선형 이온빔은 몰투몰 공정 등 대량생산을 위한 확장에 유리하고, 비독성 가스인 산소와 아르곤을 중심으로 진행한 본 연구는 친환경이 강조되는 미래산업에 매우 필수적이다.